Pontifícia Universidade Católica
do Rio de Janeiro

Matheus Samuel Martins de Sousa

Engineering the electronic and spintronic properties of graphene by spin-orbit coupling and periodic vacancies

Tese de Doutorado

Thesis presented to the Programa de Pós–graduação em Física of PUC-Rio in partial fulfillment of the requirements for the degree of Doutor em Ciências - Física.

Advisor: Prof. Wei Chen

Rio de Janeiro
August 2023

Pontifícia Universidade Católica
do Rio de Janeiro

Matheus Samuel Martins de Sousa

Engineering the electronic and spintronic properties of graphene by spin-orbit coupling and periodic vacancies

Thesis presented to the Programa de Pós–graduação em Física of PUC-Rio in partial fulfillment of the requirements for the degree of Doutor em Ciências - Física. Approved by the Examination Committee:

Prof. Wei Chen
Advisor
Departamento de Física – PUC-Rio

Prof. Caio Henrique Lewenkopf
UFF

Prof. Andrea Brito Latge
UFF

Prof. George Balster Martins
UFU

Prof. Mariana Malard Sales Andrade
UnB

Rio de Janeiro, August 10th, 2023

Matheus Samuel Martins de Sousa

Graduated in Physics at the Universidade Federal Fluminense (UFF) in 2019.

Bibliographic data

Sousa, Matheus Samuel Martins de

Engineering the electronic and spintronic properties of graphene by spin-orbit coupling and periodic vacancies / Matheus Samuel Martins de Sousa ; advisor: Wei Chen. – 2023.

95 f: il. color. ; 30 cm

Tese (doutorado) - Pontifícia Universidade Católica do Rio de Janeiro, Departamento de Física, 2023.

Inclui bibliografia

1. Física – Teses. 2. Grafeno. 3. Spintrônica. 4. Propriedades eletrônicas. 5. Interação spin-órbita. 6. Engenharia de vacâncias. I. Chen, Wei. II. Pontifícia Universidade Católica do Rio de Janeiro. Departamento de Física. III. Título.

CDD: 530

Acknowledgments

I would like to first thank my advisor Prof. Wei Chen for the opportunity to work with him and for all the support and guidance during my PhD. In every step of this work, he was always available to help me and provide me with the best conditions to develop my research. I find that under his supervision I was able to grow as a researcher and as a person. His very practical and efficient way of thinking was a great inspiration for me. I am very grateful for all the time he dedicated to me and for all the things I learned from him. I thank him for all the discussions and suggestions that helped me to improve my work. I wish to thank Prof. Mallard and Prof. Fanyao Qu for the opportunity to work with them and collaborate in their research.

I wish to thank my family for all the support and encouragement they gave me during my PhD. I am very grateful for all the love and care they gave me during this time. I thank my parents for all the sacrifices they made for me and for always believing in me. In particular, I would like to thank my mother Maisa for always being there for me and for all the love and support she gave me, I would not be here without her. My father Tácio for all the encouragement and support he gave me. My dearly grandmother Maria. I thank all my close friends for always incentivizing me and for all the good times we had together. I thank my girlfriend Hitalla for all the love and support she gave me during this time.

This study was financed in part by the Coordenação de Aperfeiçoaento de Pessoal de Nível Superior - Brasil (CAPES) - Finance Code 001.

Abstract

Sousa, Matheus Samuel Martins de; Chen, Wei (Advisor). **Engineering the electronic and spintronic properties of graphene by spin-orbit coupling and periodic vacancies**. Rio de Janeiro, 2023. 95p. Tese de Doutorado – Departamento de Física, Pontifícia Universidade Católica do Rio de Janeiro.

In this thesis, we explore different properties of Graphene, a material with a single layer of carbon atoms.

In the first section, we propose a extended tight-binding model including spin-orbit and magnetization effects in order to investigate spintronics effects on the equilibrium currents of the material. We found that there is a interplay between the spin-locking due to Rashba spin-orbit coupling and the external magnetization proposed in the model. This interplay makes the spin-currents developed in the material to have specific properties, which is highlighted on the section on nanoribbons.

In the following section, we investigate the role of nonsymmorphic symmetries, a class of symmetries that can only be realized with reflection or rotation and translation, on the electronic properties of bidimensional materials. We proposed a method to produce these symmetries on any lattice by performing vacancy engineering, i.e. removing sites at certain positions. We show that when theses symmetries are present in the structure of the material, the spectra must be restricted in such a way that every two bands must touch at a point in the Brillouin Zone, in particular there must be nodal lines along the boundaries of the Brillouin Zone.

Exploring further on the idea of vacancy engineering, we propose a method for using it to create zero-energy flat-bands for bipartite lattices. This is a realization that the Hamiltonian of bipartite lattices takes a special form, namely anti-block-diagonal, and vacancy engineering consists of removing rows and columns from the tight-binding Hamiltonian. We analyze the role of the zero-energy flat-band on the electronic correlations such as formation of a superconductivity phase.

The last two sections are dedicated to quantum metric and applications thereof, in particular in the study of topological order. We give examples and show that for continuum systems there is a closed formula for dimension D. As an application, we show that the opacity of Graphene is directly related to the topological charge.

Keywords

Graphene; Spintronics; Electronic Properties; Spin-orbit interaction; Vacancy engineering.

Resumo

Sousa, Matheus Samuel Martins de; Chen, Wei. **Modificando as propriedades eletrônicas e spintrônicas do grafeno por meio de acoplamento spin-órbita e vacâncias periódicas**. Rio de Janeiro, 2023. 95p. Tese de Doutorado – Departamento de Física, Pontifícia Universidade Católica do Rio de Janeiro.

Nesta tese, exploramos diferentes propriedades do grafeno, um material com uma única camada de átomos de carbono.

Na primeira seção, propomos um modelo estendido de tight-binding que inclui efeitos de efeitos de spin-órbita e magnetização a fim de investigar os efeitos spintrônicos sobre as correntes de equilíbrio do material. Descobrimos que há uma interação entre o spin-lock devido ao acoplamento spin-órbita de Rashba e a magnetização externa proposta no modelo. Essa interação faz com que as correntes de spin desenvolvidas no material tenham propriedades específicas, o que é destacado na seção sobre nanoribbons.

Na seção seguinte, investigamos o papel das simetrias não-simórficas, uma classe de simetrias que só podem ser realizadas com reflexão ou rotação e translação, nas propriedades eletrônicas de materiais bidimensionais. Nós propusemos um método para produzir essas simetrias em qualquer rede por meio da engenharia de vacâncias, ou seja, removendo sítios em determinadas posições. Mostramos que quando essas simetrias estão presentes na estrutura do material, os espectros devem ser ser restringido de tal forma que cada duas bandas devem se tocar em um ponto da Brillouin, em particular, deve haver linhas nodais ao longo dos limites da zona de Brillouin.

Explorando a ideia de engenharia de vacâncias, propomos um método para usá-lo para criar bandas planas de energia zero para redes bipartidas. Essa é uma constatação de que o Hamiltoniano das redes bipartidas assume uma forma especial, anti-bloco-diagonal, e a engenharia de vacância consiste em remover linhas e colunas do Hamiltoniano de tight-binding. Analisamos o papel da banda plana de energia zero sobre as correlações eletrônicas, como a formação de uma fase de supercondutividade.

As duas últimas seções são dedicadas à métrica quântica e suas aplicações, em particular no estudo da ordem topológica. Damos exemplos e mostramos que para sistemas contínuos, há uma fórmula fechada para a dimensão D. Como uma aplicação, mostramos que a opacidade do grafeno está diretamente relacionada à carga topológica.

Palavras-chave

Grafeno; Spintrônica; Propriedades eletrônicas; Interação spin-órbita; Engenharia de vacâncias.

Table of contents

List of figures

1
Introduction

Graphene is a material that has been studied since it was experimentally discovered in 2004 [1]. It is a single layer of carbon atoms arranged in a hexagonal lattice, not only is it the thinnest material ever discovered, but it is also the strongest material ever discovered, it is also a material with amazing electrical properties [2]. The foundations of graphene were laid by studying graphite, lead by the work of P. R. Wallace [3], and in more recent years, the work of Andre Geim and Konstantin Novoselov.

In this work, properties of graphene are explored in different directions. Inspired by previous work on Rashba spin-orbit coupling in graphene [4], we propose an extended tight-binding model for graphene, in which Rashba spin-orbit coupling is included and an external magnetic field modelled by a exchange interaction is used to modulated the band structure. We then use this model to show that equilibrium current can be developed in graphene, and that the properties of the current can be controlled by the direction of the magnetic field applied [5].

In some circunstances, such as in graphene nanoflakes, the material can be only partially spin-polarized, and in this case, a non-zero spin-torque can be developed. Using this model, we propose a device where graphene is sit on top a substrate, and by various proximity effects, Rashba spin-orbit coupling is induced in the graphene. This kind of device can be used in spintronics applications, such as spin-transfer-torque devices [6, 7, 8, 9, 10, 11].

Two-dimensional materials, such as graphene, have a repeating structure and can have different properties depending on the symmetries associated with the repetition. The mathematical object that quantifies these symmetries is a point group, and in two-dimensions there are only 17 possible groups called wallpaper groups. The symmetry operations include rotations, citelections, and translations.

For instance, the group of the square lattice is the p4m group, which has four-fold rotational symmetry, mirror symmetry in two perpendicular directions, and translational symmetry in the place of the lattice. There is a special class of symmetry called non-symmorphic symmetries, which involve a combination of translation and a point group symmetry operation. A example

of such symmetry is the glide symmetry, which is a combination of a reflection and a translation parallel to the reflection axis. When a material has non-symmorphic symmetries, the operators associated with the symmetry have to commute with the Hamiltonian, and this restricts the eigenvalues of the system. We show that such restrictions lead to the existance of symmetry protected nodal lines [12].

These non-symmorphic symmetries can be achieved by using a method called "vacancy engineering", which is a method to create a material with a desired symmetry by removing atoms from the lattice. This is possible by considering an enlarged unit cell, and then removing atoms from the lattice. After removing atoms, the symmetry of the system is changed, and it is predicted that nodal lines should appear in the band structure. We show that this is indeed the case, that the nodal lines are protected by the symmetry of the system and robust to perturbations.

Vacancy engineering can be used to create materials with arbitrary holes. In the special case of bi-partite lattices, where the lattice can be divided into two partitions, the removal of atoms from one partition can lead to the creation of flat-band [13, 14]. Using linear algebra arguments, we show that arbitrary flat-bands can be created by removing atoms from the sub-lattice [15]. We also show that the number of flat-bands is related to the unbalance of atoms in the two partitions. Our motivation of investigating the vacancy-engineering flat-bands comes from twisted bilayer graphene, where the band structure is known to exihib flat-bands and are related to a wide range of physical effect, such as superconductivity [16].

We investigated if even though the flat-bands in our model are unrelated to the twisted bilayer graphene in origin, they can still be used to host the same physical effects. In particular we proposed a model of graphene with one and two flat-bands, where superconductivity is modeled using a weak coupling mean-field treatment of the Bogoliubov-de Gennes equations and show that the flat-band can host a superconducting phase.

In the low energy regime, Graphene is known to have linear energy dispersion and can be well approximated by a Dirac Hamiltonian. In particular, we investigate the case of quantum metric for Dirac materials. The quantum metric has been recently used to investigate properties of materials, such as topological phase transistions and localization of Wannier states. We show that the study of quantum metric is very relevant experimentally, such as in optical conductivity experiments. We provide several results for quantum metric in Dirac materials of different dimensions.

As a example of application, we investigate the case of the opacity of

graphene, recovering the famous experimental result. This investigation leads to the interesting conclusion that the opacity of graphene must be protected by the topological charge of the Dirac cones.

This thesis goes through different phenomena, such as spintronics, vacancy-engineering, superconductivity and quantum geometry. What ties all together is their appilcation to graphene. In view of this thesis, we show that graphene is a rich playground for condensed matter physics, and although it has been extensively studied, it is a material with very interesting properties and many applications, with many more to be studied in the future.

2
Magnetoelectric torque and edge currents

We begin our investigation by considering the interplay of Rashba spin-orbit coupling (RSOC), magnetization, and geometrical confinement on graphene, especially how they influence the spintronic properties of graphene. Our motivation is that RSOC can be induced in graphene by various means, for instance by growing graphene on some specific substrates, which seems to be very promising for spintronic applications. If a magnetization is present, then one expects that some form of magnetization may be induced. On the other hand, geometrical confinement is known to be very important for graphene based devices since it dramatically influences the band structure of graphene. For instance, the zigzag ribbon and armchair ribbon are known to have very distinct band structures, and hence their spintronic properties caused by RSOC and magnetization may be very different. In addition, we will make comparison with several effects that are known to be induced by RSOC and magnetization in a simple 2D electron gas (2DEG), such as persistent edge current and edge spin current. We will first give a pedagogical introduction to the tight-binding band structure of graphene, and then consider RSOC and magnetization in the following sections.

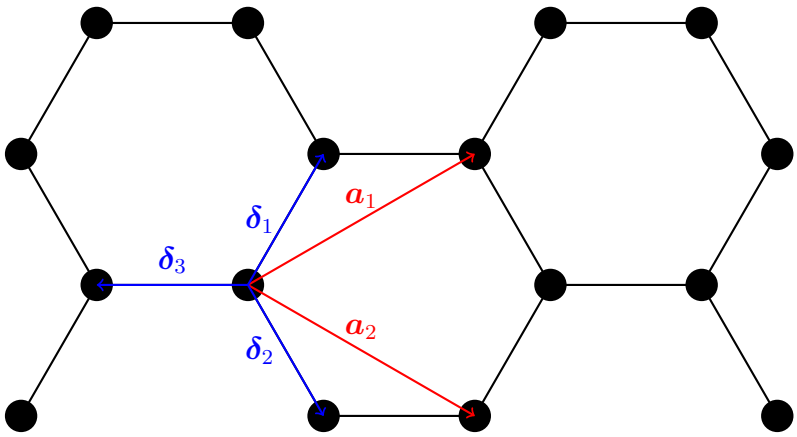

Figure 2.1: Representation of the Graphene lattice. In the figure: a_1 and a_2 are the lattice vectors, δ_1, δ_2 and δ_3 are the nearest-neighbor vectors.

2.1
Tight-binding model of Graphene

This is a pedagiogical introduction to the tight-binding Hamiltonian of graphene [17, 18] and we will serve as a reference for the rest of the paper when we consider other tight-binding models.

The tight-binding model of graphene proposed is the usual nearest-neighbor hopping model. By tight-binding model, we mean that the wave-function of the electron is highly localized at the ion position, also called atomical wave-function. The amplitude of an electron hopping from one ion to another is given by the overlap of their atomical wave-functions. We start by considering an infinite graphene sheet with periodic boundary conditions described by a surface of a torus. The graphene crystalline structure is described by a honeycomb lattice with lattice constant a and two atoms per unit cell. We characterize the lattice by the unit vectors

$$\boldsymbol{a}_1 = \frac{a}{2}\left(3, \sqrt{3}\right), \quad \boldsymbol{a}_2 = \frac{a}{2}\left(3, -\sqrt{3}\right), \tag{2-1}$$

from which we can construct the reciprocal lattice vectors

$$\boldsymbol{b}_1 = \frac{2\pi}{3a}\left(1, \sqrt{3}\right), \quad \boldsymbol{b}_2 = \frac{2\pi}{3a}\left(1, -\sqrt{3}\right). \tag{2-2}$$

Moreover, we have three nearest-neighbor vectors given by

$$\boldsymbol{\delta}_1 = \frac{a}{2}\left(1, \sqrt{3}\right), \quad \boldsymbol{\delta}_2 = \frac{a}{2}\left(1, -\sqrt{3}\right), \quad \boldsymbol{\delta}_3 = -a\left(1, 0\right). \tag{2-3}$$

and the representation of lattice can be seen in Fig. 2.1. The tight-binding model of graphene is given by the Hamiltonian where we consider electrons hopping between nearest-neighbor sites. The hopping amplitude is given by a constant t.

$$H = -t \sum_{\langle ij \rangle \sigma} c^\dagger_{i\sigma} c_{j\sigma} + \text{h.c.}, \tag{2-4}$$

where we consider units where $\hbar = 1$. The hopping amplitude of graphene is approximately $t = 2.8eV$, $c^\dagger_{i\sigma}$ is a second quantized operator that creates an electron with spin σ at site i and $c_{j\sigma}$ is the corresponding annihilation operator. The sum is made over all nearest-neighbor and is represented by the angle brackets $\langle ij \rangle$ under the summation. The hermitian conjugate must also be included in the Hamiltonian and is denoted by the h.c. term.

To obtain the Hamiltonian in momentum space, we can consider the Fourier transform of the second quantized operators

$$c^\dagger_{i\sigma} = \frac{1}{\sqrt{N}} \sum_{\boldsymbol{k}} e^{i\boldsymbol{k}\cdot\boldsymbol{r}_i} c^\dagger_{\boldsymbol{k}\sigma}, \quad c_{j\sigma} = \frac{1}{\sqrt{N}} \sum_{\boldsymbol{k}} e^{-i\boldsymbol{k}\cdot\boldsymbol{r}_j} c_{\boldsymbol{k}\sigma}, \tag{2-5}$$

where $\boldsymbol{r}_i$ is the position of the i-th site and N is the number of sites and $\boldsymbol{k}$

is the momentum in the first Brillouin zone. Now we consider the following summation

$$\sum_{\langle ij\rangle\sigma} c^{\dagger}_{i\sigma} c_{j\sigma} = \frac{1}{N} \sum_{\langle ij\rangle\sigma} \sum_{\boldsymbol{k}\boldsymbol{k'}} e^{i\boldsymbol{k}\cdot\boldsymbol{r}_i} e^{-i\boldsymbol{k'}\cdot\boldsymbol{r}_j} c^{\dagger}_{\boldsymbol{k}\sigma} c_{\boldsymbol{k'}\sigma}. \tag{2-6}$$

The sum over all nearest-neighbor sites restrict the difference between positions such that $\boldsymbol{r}_i - \boldsymbol{r}_j = \boldsymbol{\delta}_k$ for some l. This means that we can write the sum as

$$\frac{1}{N} \sum_{il\sigma} \sum_{\boldsymbol{k}\boldsymbol{k'}} e^{i(\boldsymbol{k}-\boldsymbol{k'})\cdot\boldsymbol{r}_i} e^{i\boldsymbol{k'}\cdot\boldsymbol{\delta}_l} c^{\dagger}_{\boldsymbol{k}\sigma} c_{\boldsymbol{k'}\sigma}. \tag{2-7}$$

Futhermore, we can use the following identity

$$\frac{1}{N} \sum_{i} e^{i(\boldsymbol{k}-\boldsymbol{k'})\cdot\boldsymbol{r}_i} = \delta_{\boldsymbol{k}\boldsymbol{k'}}. \tag{2-8}$$

This means that the sum over i is only non-zero when $\boldsymbol{k} = \boldsymbol{k'}$ and with these calculations we can write the Hamiltonian in momentum space as

$$H = -t \sum_{\boldsymbol{k}\sigma} \left(\sum_{l} e^{i\boldsymbol{k}\cdot\boldsymbol{\delta}_l} \right) c^{\dagger}_{\boldsymbol{k}\sigma} c_{\boldsymbol{k}\sigma} + \text{h.c.}. \tag{2-9}$$

In the case of graphene, the sum in parenthesis is equal to

$$\sum_{l} e^{i\boldsymbol{k}\cdot\boldsymbol{\delta}_k} = e^{i\boldsymbol{k}\cdot\boldsymbol{\delta}_1} + e^{i\boldsymbol{k}\cdot\boldsymbol{\delta}_2} + e^{i\boldsymbol{k}\cdot\boldsymbol{\delta}_3} \tag{2-10}$$

$$= e^{2ik_x a} + 2e^{ik_x a} e^{ik_y a} \cos\left(\sqrt{3}k_y a\right) = Z. \tag{2-11}$$

Knowing this, the Hamiltonian in momentum space can written in matrix form as

$$H = -t \sum_{\boldsymbol{k}\sigma} \begin{pmatrix} 0 & Z^* \\ Z & 0 \end{pmatrix}. \tag{2-12}$$

Writing Z as a complex number in polar form, we have

$$Z = \tilde{Z} e^{i\varphi}. \tag{2-13}$$

where $\tilde{Z}$ and φ are the magnitude and phase of Z, respectively. It is clear to see that the eigenvalues of this matrix are given by

$$\varepsilon_{\pm} = \pm t \sqrt{3 + 4\cos\left(k_x a\right)\cos\left(\sqrt{3}k_y a\right) + 2\cos\left(2\sqrt{3}k_y a\right)}. \tag{2-14}$$

and the eigenvectors are given by

$$|\psi\rangle_{\pm} = \frac{1}{\sqrt{2}} \begin{pmatrix} \pm e^{i\varphi} \\ 1 \end{pmatrix}. \tag{2-15}$$

2.2 Spin-orbit coupling

Throughout this thesis the Rashba spin-orbit coupling is used, so this section is dedicated to introducing it and showing how we must include the RSOC in the tight-binding Hamiltonian. The nearest-neighbors RSOC Hamiltonian is given by

$$H_{RSOC} = i\lambda_R \sum_{\langle ij\rangle\alpha\beta} c^\dagger_{i\alpha} \left(\boldsymbol{\sigma}_{\alpha\beta} \times \boldsymbol{d}_{ij}\right)^z c_{j\beta} + \text{h.c.}, \tag{2-16}$$

where $\boldsymbol{\sigma} = (\sigma_x, \sigma_y, \sigma_z)$ is Pauli vector and $\boldsymbol{d}_{ij}$ is the vector pointing from site i to site j. Proceeding as before, we can write the Hamiltonian in momentum space by Fourier transforming the second quantized operators and restricting the sum to nearest-neighbor sites so that $\boldsymbol{r}_i - \boldsymbol{r}_j = \boldsymbol{\delta}_l$. This gives us

$$H_{RSOC} = i\lambda_R \sum_{\boldsymbol{k}l\alpha\beta} e^{i\boldsymbol{k}\cdot\boldsymbol{\delta}_l} c^\dagger_{\boldsymbol{k}\alpha} \left(\boldsymbol{\sigma}_{\alpha\beta} \times \boldsymbol{\delta}_l\right)^z c_{\boldsymbol{k}\beta} + \text{h.c.}, \tag{2-17}$$

where λ_R is the strength of the RSOC interaction and $\boldsymbol{\sigma}$ is the Pauli vector. The z-component of cross vector product can be written as

$$\left(\boldsymbol{\sigma}_{\alpha\beta} \times \boldsymbol{\delta}_l\right)^z = \sigma^x_{\alpha\beta}\delta^y_l - \sigma^y_{\alpha\beta}\delta^x_l. \tag{2-18}$$

Summing over the spin indices, we have

$$H_{RSOC} = i\lambda_R \sum_{\boldsymbol{k}l} e^{i\boldsymbol{k}\cdot\boldsymbol{\delta}_l} \begin{pmatrix} c^\dagger_{\boldsymbol{k}\uparrow} & c^\dagger_{\boldsymbol{k}\downarrow} \end{pmatrix} \begin{pmatrix} 0 & \delta^y_l + i\delta^x_l \\ \delta^y_l - i\delta^x_l & 0 \end{pmatrix} \begin{pmatrix} c_{\boldsymbol{k}\uparrow} \\ c_{\boldsymbol{k}\downarrow} \end{pmatrix} + \text{h.c.} \tag{2-19}$$

$$\tag{2-20}$$

As we can see, the RSOC has the effect of lifting the degeneracy of the spin degree of freedom of electron at different sites and splitting their energy levels.

2.3 Magnetization

The magnetization component of the tight-binding Hamiltonian is given by

$$H_{ex} = J_{ex} \sum_{i\alpha\beta} \boldsymbol{S} \cdot c^\dagger_{i\alpha} \boldsymbol{\sigma}_{\alpha\beta} c_{i\beta} + \text{h.c.}, \tag{2-21}$$

where $\boldsymbol{S} = S\left(\sin\left(\theta\right)\cos\left(\phi\right), \sin\left(\theta\right)\sin\left(\phi\right), \cos\left(\theta\right)\right)$ is the spin operator. J_{ex} is the exchange interaction between $\boldsymbol{S}$ and the electron spin. This Hamiltonian is local, meaning that there is no exchange between electrons on different sites, only between electron spins on the same site. The Hamiltonian can be written in momentum space by Fourier transforming the second quantized operators

$$H_{ex} = J_{ex} \sum_{\boldsymbol{k}\alpha\beta} \boldsymbol{S} \cdot c^{\dagger}_{\boldsymbol{k}\alpha} \boldsymbol{\sigma}_{\alpha\beta} c_{\boldsymbol{k}\beta} + \text{h.c.}, \tag{2-22}$$

$$= J_{ex} \sum_{\boldsymbol{k}} \begin{pmatrix} c^{\dagger}_{\boldsymbol{k}\uparrow} & c^{\dagger}_{\boldsymbol{k}\downarrow} \end{pmatrix} \begin{pmatrix} \cos(\theta) & \sin(\theta)\, e^{-i\phi} \\ \sin(\theta)\, e^{i\phi} & -\cos(\theta) \end{pmatrix} \begin{pmatrix} c_{\boldsymbol{k}\uparrow} \\ c_{\boldsymbol{k}\downarrow} \end{pmatrix} + \text{h.c.} \tag{2-23}$$

The effect of this magnetization Hamitlonian is twofold, and it will depend on the direction given by angles θ and ϕ. It shifts the chemical potential between electrons at the same site with different spins and also provides an amplitude of flipping the spin.

2.4 Extended tight-binding model for graphene

We want a situation where we have a graphene sheet with a magnetic field applied perpendicular to the plane of the sheet. Moreover, by means of proximity effect, we want to induce a spin orbit coupling of them Rashba type. This ingredients are important for what we want to demonstrate, namely that the RSOC modifies the equilibrium properties of 2D materials, with effects including: spin-momentum locking, spin-orbit torque and chiral edge currents.

We formulate the tight-binding model including the RSOC 2-20, the exchange term 2-23 and chemical potential term. The Hamiltonian is given by

$$H = -\mu \sum_{i\sigma} c^{\dagger}_{i\sigma} c_{i\sigma} - t \sum_{\langle ij \rangle} c^{\dagger}_{i\uparrow} c_{j\uparrow} \tag{2-24}$$

$$+ i\lambda_R \sum_{\langle ij \rangle \alpha\beta} c^{\dagger}_{i\alpha} \boldsymbol{\sigma}_{\alpha\beta} c_{j\beta} + J_{ex} \sum_{i\alpha\beta} \boldsymbol{S} \cdot c^{\dagger}_{i\alpha} \boldsymbol{\sigma}_{\alpha\beta} c_{i\beta} + \text{h.c.}, \tag{2-25}$$

where μ is the chemical potential and the other individual terms were defined in the previous sections. The Hamiltonian is diagonalized, yielding four energy eigenvalues for each $\boldsymbol{k}$ point and the corresponding eigenvectors. Due to particle-hole symmetry, half of the eigenvalues are filled and the other half are empty. The ground state is composed by all the filled states, which is this case are the first two.

As a first result, we want to demonstrate the effect of the RSOC on the bandstructure of graphene. To do this, we calculate the spin polarization of the lowest energy level for all values $\boldsymbol{k}$ in the first Brillouin zone. The polarization is given by the formula $\boldsymbol{\sigma} = \langle u_{\boldsymbol{k}} | \boldsymbol{\sigma} | u_{\boldsymbol{k}} \rangle$, where $u_{\boldsymbol{k}}$ is the eigenvector corresponding to the lowest energy eigenvalue for $\boldsymbol{k}$. To make it presentable, we plot the polarization in the (k_x, k_y) plane and the direction of each arrow

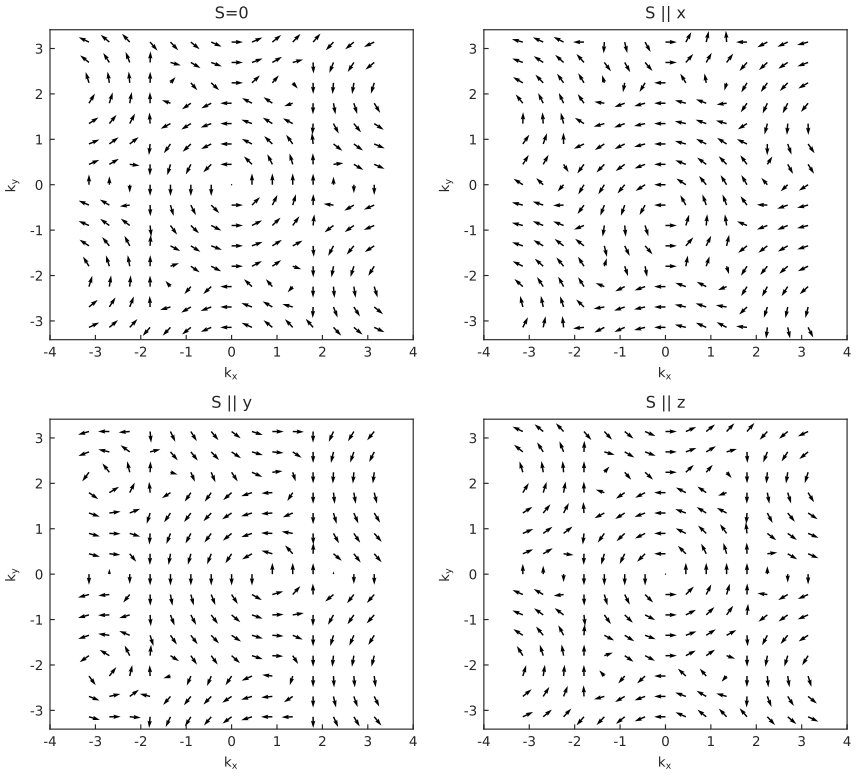

Figure 2.2: A x-y projection of the spin polarization showing a locking effect due to RSOC with varying magnetization direction. The size of the arrows indicate the magnitude of the polarization. The top left panel corresponds to no magnetization, the top right panel corresponds to magnetization along the x direction, the bottom left panel corresponds to magnetization along the y direction, and the bottom right panel corresponds to magnetization along the z direction.

corresponds to the (x, y) components of the polarization. The spin-texture is shown in 2.2 for different directions of external magnetization. As can be seen, the RSOC induces vortices in the spin texture, which is a direct consequence of the spin-momentum locking effect. These vortices are localized in the K and K' points, which are the Dirac points, moreover, there is one additional vortex in the Γ point. For magnetization pointing along the x direction, the bandstructure is distorted, similarly for magnetization pointing along the y direction. For magnetization pointing along the z direction, the bandstructure is not distorted.

2.5 Persistent current in zigzag nanoribbons

Having understood the effect of RSOC on the bandstructure of graphene, with its spin-momentum locking effect, we now want to investigate the effect of geometrical confinement, i.e, how the interplay of magnetization and spin-momentum locking will affect the equilibrium properties of graphene. To do

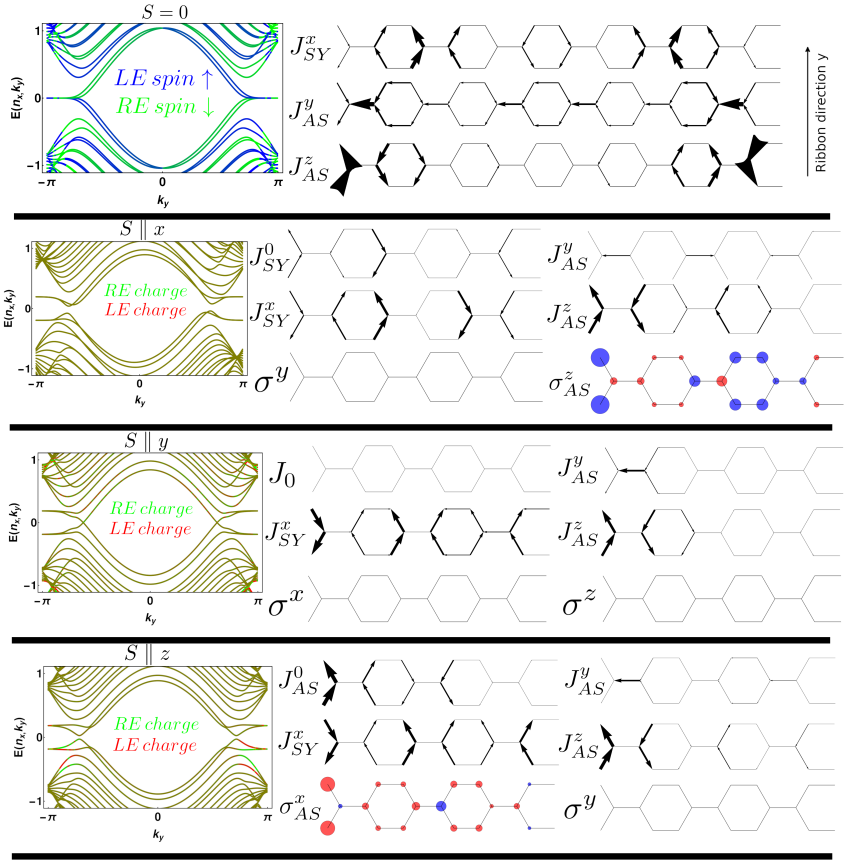

Figure 2.3: Numerical results for the zigzag edge nanoribbon in the cases of (a) no magnetization, and magnetization along (a) x, (b) y, and (c) z directions. In each case we plot the band structure, charge current, and spin current polarized in (x,y,z) directions as indicated by the black arrows that are proportional to the magnitude of the current. The induced magnetization is indicated by the circles, with the size of the circle indicating the magnitude and the color indicating the sign. We only plot half of the width and one unit cell along the ribbon direction since the patterns are either symmetric (SY) or antisymmetric (AS) between the two edges, as indicated by the subscript of these quantities

this, we consider a zigzag nanoribbon of graphene, which is a system that has been extensively studied in the literature. The zigzag nanoribbon is a system that has a non-trivial topology, which is characterized by the existence of edge states that are localized at the edges of the ribbon. These edge states are protected by time-reversal symmetry.

Numerical results for the zigzag ribbons are given in Fig 2.3, where we investigated the cases of no magnetization and in the presence of magnetization. For the latter case, we examine the situations of magnetization pointing at all three principle directions (x, y, z). The results are summarized in what follows.

(i) $\boldsymbol{S} = 0$: In the absence of magnetization, it is known that RSOC itself is sufficient to induce a spin current polarized in x direction and flowing in

y direction, and another one that is polarized in y direction and flowing in x direction, as our numerical calculation also confirms [19]. Besides, a helical (spin chiral) edge spin current polarized in z is also produced, whose flowing direction is opposite between the two edges [20, 21, 22]. The origin of this helical edge spin current can be understood from the figure of the band structure, where we color the eigenstate according to the spin component of the wave function at the left edge (blue and green colors). From the figure, one sees that for every spin up k_y state (blue) there exists a corresponding spin down $-k_y$ state (green), thereby producing counter propagating spins at the left edge. Moreover, this feature manifestsfor all eigenstates, and hence the helical edge spin current is not just the result of low energy states, but all eigenstates in the Fermi sea. Finally, these features of spin current are found to be true even for the cases with a magnetization that are described below.

(ii) $\boldsymbol{S}$ along x: It has been pointed out that in 2-D metallic systems with RSOC, a magnetization lying in-plane and pointing perpendicular to the edge will produce an edge charge current [23]. The direction of flow of this edge charge current depends on the distance away from the edge, i.e., it actually manifests as a laminal flow of charge current. This situation corresponds to the $\boldsymbol{S}$ along x situation in our model, and the laminal flow of charge current symmetric between the two edges is clearly seen from our numerical results. The origin of this laminal flow may be traced back to the band structure, where we see that the eigenstates are not particularly localized at either edge, but the whole band structure is distorted and antisymmetric $E(n_x, k_y) = -E(n_x, -k_y)$, causing the edge charge current. We also find a large transverse spin polarization σ_z induced near the edge, a phenomena similar to that uncovered in a low-energy Dirac model [24]. Because the magnetization is along x but the induced spin polarization is along z, this implies that the spin polarization exerts a local torque on the magnetization according to the Landau-Lifshitz dynamics. However, because the induced spin polarization is antisymmetric between the two edges, the torque of the whole ribbon averages to zero. Nevertheless, such a antisymmetric spin polarization is expected to cause a noncollinear order between the two edges.

(iii) $\boldsymbol{S}$ along y: For the case of a magnetization along the ribbon, numerical result shows no charge current and no spin accumulation polarized along x or z directions, and hence the spin accumulation does not exert a local torque on the magnetization. The energy spectrum is half-metallic.

(iv) $\boldsymbol{S}$ along z: For the case of an out-of-plane magnetization, a charge current is produced, and it is antisymmetric (chiral) between the two edges. Comparing with the charge current in the $\boldsymbol{S}$ along x case, this suggests

the chirality of the charge current can be controlled by the direction of the magnetization. Moreover, this charge current only occurs at finite chemical potential, similar to that in the QAHE in topologically nontrivial Chern insulators [25]. Further analyzing the band structure and the wave function, we find that the band structure is symmetric between $+k_y$ and $-k_y$, but the wave function distribution is not: If the $+k_y$ state is mostly localized at the left edge (red), then the $-k_y$ state is more localized at the right edge (green). This feature naturally suggests counterpropagating charge currents at the two edges. In addition, the band structure shows that some of the low-energy states are inherited from the flat band edge states of the pristine zigzag ribbon, which become dispersive under the combined effect of magnetization and RSOC. Besides these currents, transverse spin polarizations σ_x are also induced near the edges, but are of opposite signs at the two edges and hence average to zero, yielding no local torque on the magnetization. From analyzing different magnetization directions, we conclude that for magnetization along principle directions (x,y,z), only the (χ_{xz}, χ_{zx}) components of the transverse susceptibility are nonzero, which cause a local spin torque according to the Landau-Lifshitz dynamics. However, the transverse spin polarization always has the same magnitude but of opposite sign between the two edges, and therefore the spin polarization of the whole system integrates to zero, indicating no net torque on a macroscopic scale.

2.6 Persistent current in armchair nanoribbons

Numerical results for the armchair ribbons with and without magnetization are given in Fig 2.4. For the magnetized case, the results also depend on the direction of magnetization. We summarize the results below.

(i) $\boldsymbol{S} = 0$: The case without magnetization has the bulk spin current caused by RSOC just like in the zigzag ribbon. The difference here is that J_x is strongly suppressed due to the open boundary condition in the y direction. The system also produces an out-of-plane polarized helicalspin current whose directions of flow are opposite between the two edges. An analysis on the band structure shows that this spin current originates from the eigenstates that contain counterpropagating spins,as can be deduced from the color codes of the band structure. These features of spin currents are found to remain valid in the magnetized cases below.

(ii) $\boldsymbol{S}$ along x: For the case of magnetization pointing in-plane and along the ribbon, we find no charge current, but a spin accumulation polarized in both transverse directions is induced, indicating a spin torque according to

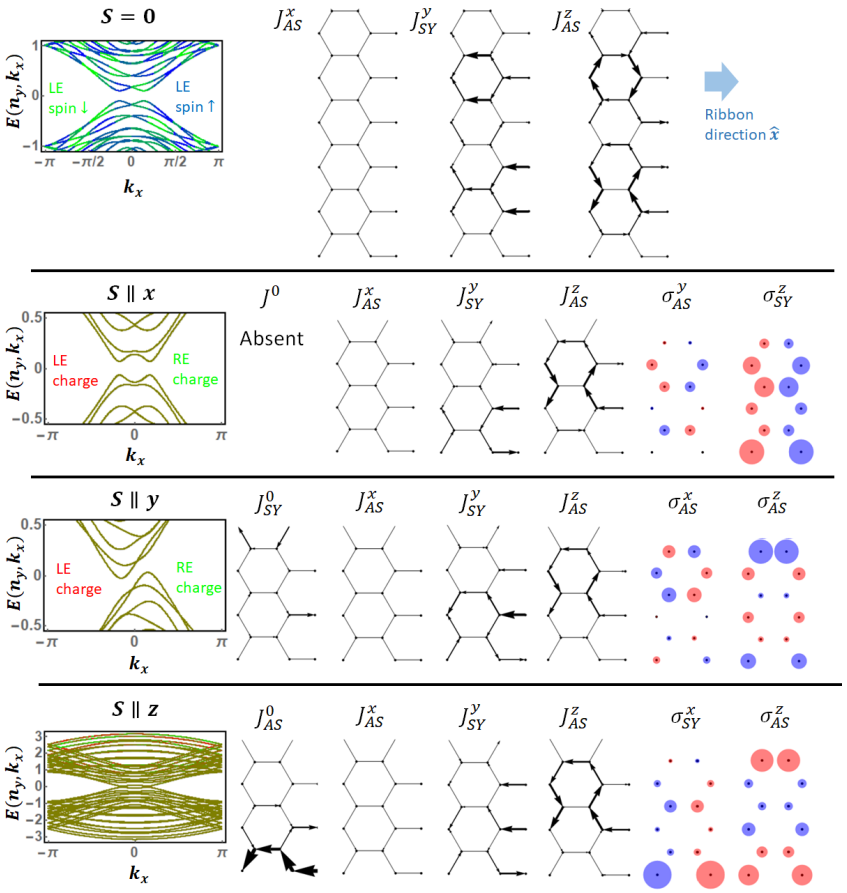

Figure 2.4: Numerical results for the armchair edge nanoribbon in the cases of (a) no magnetization, and magnetization along (a) x, (b) y, and (c) z directions, where we plot the band structure, charge current, and spin current polarized in (x,y,z) directions as indicated by the black arrows, as well as the induced magnetization is indicated by the circles. Only half of the width of the ribbon and one unit cell along the ribbon direction is plotted since the patterns are either symmetric (SY) or antisymmetric (AS) between the two edges.

the Landau-Lifshitz dynamics. In addition, the σ_y component is found to be anti-symmetric between the two edges, and as a result it yields a non-collinear magnetic order between the two edges. On the other hand, the σ_z component is found to be symmetric for the two edges, but it has alternating signs along the ribbon, meaning that it should generate a non-collinear magnetic order along the ribbon.

(iii) $\boldsymbol{S}$ along y: For the case of magnetization pointing in-plane but perpendicular to the ribbon direction, we find that an asymmetric band structure causes a non-chiral charge current whose flow direction is the same at the two edges. Spin polarizations in both transverse directions σ_x and σ_z are induced, and are asymmetric between the two edges and therefore averages to zero in the mesoscopic scale.

(iv) $\boldsymbol{S}$ along z: The presence of an out-of-plane magnetization in found to

induce a symmetric band structure, but the wave function has an interesting feature: For a given $+k_x$ state that is more localized at the right edge, there exists a corresponding $-k_x$ state at the left edge, suggesting the existence of a chiral edge charge current. Moreover, this feature more prominent for the higher-energy states than the lower-energy states. Comparing this feature with the $\boldsymbol{S}$ along y result, we conclude that the chirality of edge charge current can actually be controlled by the magnetization direction. For the induced spin polarization, one sees that the σ_z-component is anti-symmetric between the two edges, while σ_y is symmetric but has an alternating sign along the ribbon. Finally, comparing the spin polarizationin all three situations of magnetization along (x,y,z), we conclude that every component of the local susceptibility tensor $\chi_{\alpha\beta}$ is nonzero, which is very different from that of the zigzag ribbon. Nevertheless, the total torque averaged over the whole ribbon vanishes in all cases.

2.7 Graphene nanoflakes

From the analysis in the previous section, we see that although there is a transverse spin polarization induced by the magnetization in the nanoribbon, indicating a local spin torque, the average spin polarization is always zero and hence no spin torque in the macroscopic scale. An interesting issue is whether one can overcome this feature to produce a net spin torque such that it may have some applications in spintronics. To achieve this goal, we propose two setups. The first proposal is to make the nanoribbon only partially magnetized. For instance, one can make the region closer to one edge magnetized but the rest of the ribbon unmagnetized. In Fig 2.5, we use a zigzag ribbon with magnetization $\boldsymbol{S}$ along $\boldsymbol{x}$ as an example, and find that a nonzero net transverse spin polarization. The average value of spin polarization per site can reach the order of $\sigma_z \sim 10^{-4}$ when the magnetization only covers a region near an edge, but it can bedramatically enhanced to $\sigma_z \sim 10^{-2}$ if only the edge sites are magnetized. According to the Landau-Lifshitz dynamics, the spin polarization $\sigma_z \sim 10^{-4}$ and exchange coupling $J_{ex} \sim 0.1eV$ would cause a very large spin torque $dS/dt \sim 10GHz$. In fact, even if the magnitude of this torque is reduced by two orders of magnitude, it is still large enough to yield a detectable effect.

The second proposal to harvest a nonzero net torque is to use graphene nanoflakes with irregular shapes [26, 27, 28, 29]. The motivation is that the irregular shape may help to generate a nonuniform distribution of spin polarization that does not average to zero, since the two edges are not equivalent, or in a very irregular shape it may even be ambiguous to identify

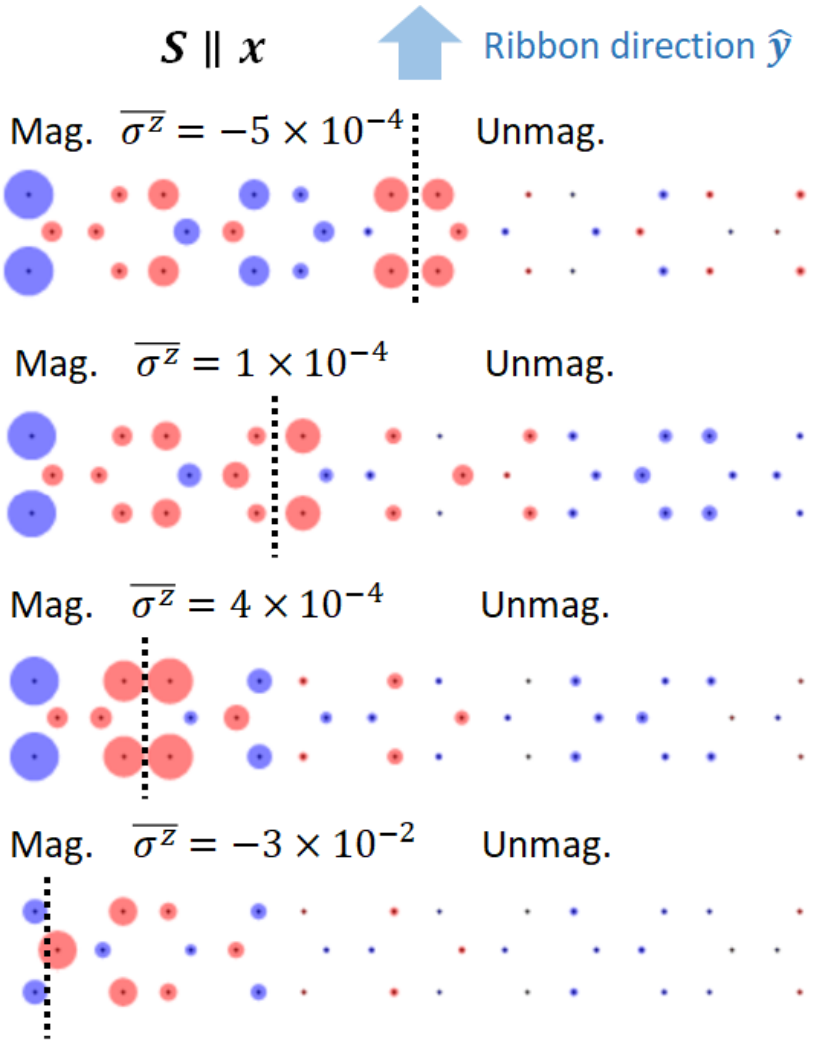

Figure 2.5: Theoretical proposal of using partially magnetized nanoribbon to produce a spin torque. In a partially magnetized zigzag ribbon with a magnetization $\boldsymbol{S}$ along x, a transverse spin polarization σ_z is indicated by the size of disks, withthe color indicating positive (red) and negative (blue). We consider the situation that the region to the left of the dotted line is magnetized, and to the right is unmagnetized. The panels from top to bottom indicate the situation of magnetization covering 1/2, 1/3, 1/6, and only the edge sites of the ribbon. In all these cases, the average spin polarization per σ_z is nonzero, indicating a net spin torque.

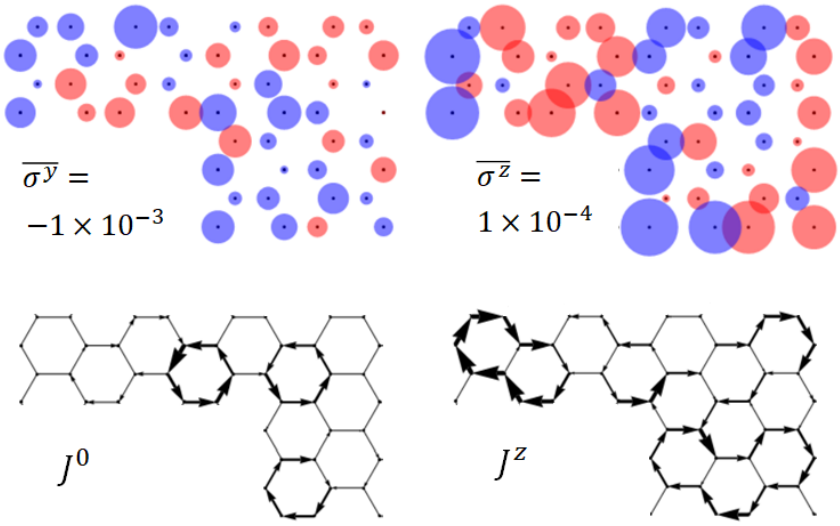

Figure 2.6: Another theoretical proposal of using an L-shaped nanoflake with magnetization $\boldsymbol{S}$ along x to produce a net spin torque. In this figure, we show the transverse spin polarizations σ_y and σ_z , charge current J_0, and out-of-plane polarized spin current J_z. The circles and arrows indicate their magnitude, with the color code indicating their sign. The average value of the spin polarization is indicated on the graphs.

two opposite edges. In Fig. 2.6, we use an L-shaped nanoflake as an example to investigate this situation. The numerical result indeed yields a net σ_y and σ_z per site of the order of 10^{-3} to 10^{-4}, respectively, when magnetization is in-plane and points along x, indicating a net torque of significant magnitude. Another interesting feature of the nanoflake is that despite the open boundary in all directions, equilibrium charge and spin currents (J_0, J_x, J_y, J_z) still exist. These currents manifest as networks of local currents with the continuity equation satisfied on every site (they are persistent currents that do not continuously accumulate charge or spin on any site), suggesting that they occur abundantly in realistic magnetized nanoflakes of all kinds of shapes.

3
Engineering nodal lines in the band structure of graphene by periodic vacancies

In this section, we examine the possibility of engineering a band structure consisting nodal lines in graphene. The nodal lines are where bands cross each other in the 2D Brillouin zone (BZ), and it is possible to generate them by imposing crystalline symmetries owing to the periodic pattern of the vacancies. In addition, we shall see below that the crystalline symmetries that are nonsymmorphic will enforce the nodal lines at the BZ boundary, which we call symmetry-enforced nodal lines [30, 31, 32]. The general principle behind the vacancy engineering is the fact that periodic vacancies fundamentally change the crystalline symmetry of the host system. This principle has been demonstrated for some 2D materials like borophene [33, 34], and our work is particularly interested in demonstrating this principle in graphene given that it is the most abundent 2D material and the easies to be fabricated [12]. In addition, we will mention that such vacancy-engineered nodal lines are actually not just a theoretical proposal, but has already been realized experimentally in the so-called nanoporous graphene [35].

Since we are interested in the crystalline symmetry of 2D materials, the relevant mathematical concept to this problem are the wall paper groups. For any repeating 2D patterns, concerning the operations that leave the patterns unchanged like reflection, inversion, rotation, etc., one can classify all the repeating patterns into a total of 17 wall paper groups. For our purpose of generating nodal lines, the relevant wall paper groups are those containing nonsymmorphic symmetries, which in 2D are related to the glide plane operation, i.e., a reflection about some axis and then translate it along the axis by some distance will leave the repeating pattern unchanged. In this particular work, we will show that it is possible to use periodic vacancies to turn graphene into patterns that belong to the $p2mg$ and $p2gg$ groups, and turn a square lattice into a pattern that belongs to the $p4gm$ group, whose band structures all contain nodal lines at the BZ boundary as predicted. We will denote that patterns that we propose by C_N, where N labels the number of sublattices in the rectangular unit cell of the periodic pattern. In addition, before we introduce these 2D patterns, we will use a simple 1D model to

elaborate the mechanism for the band crossing imposed by the nonsymmorphic symmetry.

3.1 Symmetry-enforced band crossing in one-dimension

Before diving into the nodal lines in 2D systems, we first use use a simple 1D model to demonstrate the simple mechanism behind the band crossing (or nodal points) enforced by nonsymmorphic symmetry in 1D. The nodal lines in 2D are formed for basically the same reasons, as we should see in the following sections. Consider a 1D system that has nonsymmorphic symmetry and is consists of only two sublattices denoted by A and B. The glide plane operator in momentum space is denoted by $g(k)$ and is a 2×2 matrix. This operator maps A_i to B_i within the same unit cell i, but maps B_i to A_{i+1} in the next unit cell $i+1$ so it must pick up an additional phase. As a result, $g(k)$ takes the form

$$g(k) = \begin{pmatrix} 0 & e^{-ik} \\ 1 & 0 \end{pmatrix}, \tag{3-1}$$

which has eigenvalues $\pm e^{-ik/2}$. The precise form of the Hamiltonian does not matter for our discussion. Nevertheless, for concreteness, one may consider a tight-binding model for the zigzag ladder shown in Fig. 3.1 (a) that serves our purpose. The Hamiltonian $H(k)$ commutes with $g(k)$ since we consider systems that have nonsymmorphic symmetry, so we can label the eigenstates by

$$g(k)|\psi_\pm(k)\rangle = \pm e^{-ik/2}|\psi_\pm(k)\rangle, \quad H(k)|\psi_\pm(k)\rangle = E_\pm(k)|\psi_\pm(k)\rangle. \tag{3-2}$$

Now consider particularly the BZ boundary $k = 0$ and $k = \pi$, and use the fact that the glide plane operator at the two momenta is the same $g(0) = g(2\pi)$, which yields

$$\begin{aligned} &g(0)|\psi_+(0)\rangle = +|\psi_+(0)\rangle, \\ &g(0)|\psi_-(0)\rangle = -|\psi_-(0)\rangle, \\ &g(2\pi)|\psi_+(2\pi)\rangle = +e^{-i\pi}|\psi_+(2\pi)\rangle = -|\psi_+(2\pi) = g(0)|\psi_+(2\pi)\rangle. \end{aligned} \tag{3-3}$$

So we get $g(0)|\psi_+(2\pi)\rangle = -|\psi_+(2\pi)\rangle$, but this result has exactly the same form as the second line of the above equation $g(0)|\psi_-(0)\rangle = -|\psi_-(0)\rangle$, leading us to conclude that $|\psi_+(2\pi) = |\psi_-(0)\rangle$. This means that the eigenstate $|\psi_+(k)\rangle$ with glide plane eigenvalue $+e^{-ik/2}$ and the eigenstate $|\psi_-(k)\rangle$ with glide plane eigenvalue $-e^{-ik/2}$ are connected at the BZ boundary, as indicated

schematically in Fig. 3.1 (b). Obviously, the same argument also leads to $|\psi_-(2\pi) = |\psi_+(0)\rangle$.

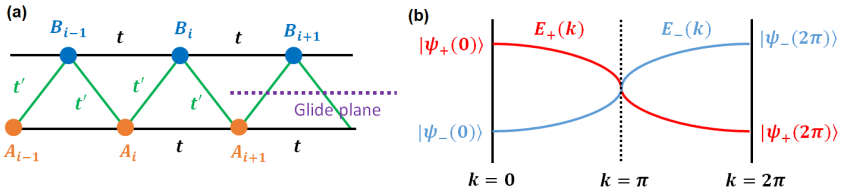

Figure 3.1: (a) A zigzag ladder example in 1D that has nonsymmorphic symmetry, which distinguishes the two sublattices A_i and B_i within unit cell i, and the hoppings on the legs t and on the rungs t' may be different. The system is invariant under a reflection about the glide plane plus a shift over half a unit cell. (b) Schematics of the band crossing enforced by the nonsymmorphic symmetry, where the two bands $E_+(k)$ and $E_-(k)$ of different glide plane eigenvalues swap at $k = \pi$.

Now consider eigenenergies in this problem. Using the fact that the Hamiltonian at the BZ boundary is the same $H(0) = H(2\pi)$ and $|\psi_-(2\pi) = |\psi_+(0)\rangle$ we have just proved, one has

$$\begin{aligned} H(0)|\psi_+(0)\rangle &= E_+(0)|\psi_+(0)\rangle = H(2\pi)|\psi_-(2\pi)\rangle \\ &= E_-(2\pi)|\psi_-(2\pi)\rangle = E_-(2\pi)|\psi_+(0)\rangle, \end{aligned} \tag{3-4}$$

This indicates that $E_+(0) = E_-(2\pi)$, meaning that the $E_+(k)$ is gradually evolves to connect with $E_-(k)$ at the BZ boundary $k = 0$ (equivalently $k = 2\pi$), as shown schematically in Fig. 3.1 (b). Naturally, this means that $E_+(k)$ and $E_-(k)$ must cross somewhere in the BZ, forming a nodal point.

We can further prove that the crossing of the two bands $E_+(k)$ and $E_-(k)$ must occur in the middle of the BZ $k = \pi$, which is usually the choice of BZ boundary. Consider the momenta $k = \pi$ and $k = -\pi$, which in practice are the same point. The glide plane operator is the same at these two momenta

$$g(\pi) = g(-\pi) = \begin{pmatrix} 0 & -1 \\ 1 & 0 \end{pmatrix}, \tag{3-5}$$

leading to the eigenvalues and eigenstates

$$\begin{aligned} &g(\pi)|\psi_+(\pi)\rangle = -i|\psi_+(\pi)\rangle, \quad g(\pi)|\psi_-(\pi)\rangle = i|\psi_-(\pi)\rangle, \\ &g(-\pi)|\psi_+(-\pi)\rangle = i|\psi_+(-\pi)\rangle, \quad g(-\pi)|\psi_-(-\pi)\rangle = -i|\psi_-(-\pi)\rangle. \end{aligned} \tag{3-6}$$

But since $g(\pi) = g(-\pi)$, one immediately concludes that it must be possible

to choose a gauge in which

$$|\psi_+(\pi)\rangle = |\psi_-(-\pi)\rangle, \quad |\psi_-(\pi)\rangle = |\psi_+(-\pi)\rangle. \tag{3-7}$$

Further using the fact that $H(\pi) = H(-\pi)$ and $|\psi_+(\pi)\rangle = |\psi_-(-\pi)\rangle$ that we just proved, the eigenvalue problem becomes

$$\begin{aligned} &H(\pi)|\psi_+(\pi)\rangle = E_+(\pi)|\psi_+(\pi)\rangle = H(-\pi)|\psi_-(-\pi)\rangle \\ &= E_-(-\pi)|\psi_-(-\pi)\rangle = E_-(-\pi)|\psi_+(\pi)\rangle, \end{aligned} \tag{3-8}$$

leading us to conclude that $E_-(-\pi) = E_+(\pi)$. Moreover, because $k = \pi$ and $k = -\pi$ are the same point, one has

$$E_-(-\pi) = E_+(\pi) = E_-(\pi), \tag{3-9}$$

meaning that the two bands must cross each other (or "stick together") at $k = \pi$.

3.2 Vacancy-engineered graphene with a single glide plane

Having understood the band crossing in 1D, we proceed to examine graphene with periodic vacancies that possess nonsymmorphic symmetry, especially to elaborate how the band crossing leads to the formation of nodal lines and loops at the BZ boundary. We first propose a C_{10} configuration that contains a glide plane going along $\hat{\mathbf{y}}$, and a reflection plane along $\hat{\mathbf{x}}$, as shown in Fig. 3.2 (a). These symmetry properties make the C_{10} belong to the wallpaper group $p2mg$. To examine the band structure of this configuration, we consider the nearest-neighbor hopping tight-binding model of graphene and add a strong local potential to project out the vacancy sites in the desired configuration

$$H = t \sum_{\langle ij \rangle, \sigma} c^\dagger_{i\sigma} c_{j\sigma} + U \sum_{i \in vac, \sigma} c^\dagger_{i,\sigma} c_{i\sigma}. \tag{3-10}$$

Here $c_{i\sigma}$ is the electron annihilation operator of spin σ on the lattice site i, t is the hopping amplitude between nearest neighbor lattice sites $\langle ij \rangle$, and $U \gg t$ is the local potential that projects out the impurity sites. The band structure can be solved by diagonalzing the Hamiltonian Fourier transformed to momentum space. The result for the band structure of C_{10} shown in Fig. 3.2 (b) clearly indicates that every two bands cross each other at the BZ boundary in the $\hat{\mathbf{y}}$ direction. As a result, the band structure contains a set of nodal lines at the BZ boundary. To understand this formation of these nodal lnies, we observe

that in this C_{10} configuration, every two sublattices form a pair that map to each other under glide-plane operation, which we call a glide pair. To further analyze these glide pairs, we denote the position of the unit cell to be (x, y), and each sublattice to be upper-cased letter $(A, B, C...)$. For instance, if we consider a configuration with four sites per unit-cell, we would label the basis as (A, B, C, D), respectively. We find that there are two kinds of glide pairs that we call type-I and type-II, which are distinguished by how the electron annihilation operators $c^{\text{sub}}_{x,y}$ transform under glide-plane operation

$$\begin{aligned} &\text{Type I}: \ c^{A}_{-x,-y} \to c^{B}_{x,-y}, \quad c^{B}_{-x,-y} \to c^{A}_{x,-y+1}, \\ &\text{Type II}: \ c^{C}_{-x,-y} \to c^{D}_{x-1,-y}, \quad c^{D}_{-x,-y} \to c^{C}_{x-1,-y+1}. \end{aligned} \tag{3-11}$$

These relations indicate that the glide plane reflects the x-coordinate of a type-I pair, but the glide plane reflects the x-coordinate and then translates to a neighboring unit cell along x for a type-II pair. In both types of pairs, the reflection of the x-coordinate is followed by a translation along y which lands at the neighboring unit cell in the y direction. For instance, if one checks carefully by eyes, the glide pairs for the C_{10} configuration defined with respect to the glide plane G are

$$\begin{aligned} \text{Type}-\text{I}: &\quad (1,6), \quad (3,8), \quad (5,10), \\ \text{Type}-\text{II}: &\quad (2,7), \quad (4,9), \end{aligned} \tag{3-12}$$

with the numbering of atoms shown in Fig. 3.2 (c).

Suppose there are N_1 type-I and N_2 type-II glide pairs in a specific configuration C_N, such as $N_1 = 3$ and $N_2 = 2$ for the C_{10} configuration according to Eq. (3-12). Using Eq. (3-11), we arrive at the conclusion that the $N \times N$ glide-plane operator $G(\mathbf{k})$ of the whole system is block diagonal, with $N_1 + N_2 = N/2$ blocks of 2×2 matrices

$$\begin{aligned} &G(\mathbf{k}) = N_1\, g_1(\mathbf{k}) \oplus N_2\, g_2(\mathbf{k}) \Updownarrow_{k_x}, \\ &g_1(\mathbf{k}) = \begin{pmatrix} & e^{-ik_y} \\ 1 & \end{pmatrix}, \quad g_2(\mathbf{k}) = \begin{pmatrix} & e^{-ik_x - ik_y} \\ e^{-ik_x} & \end{pmatrix}, \end{aligned} \tag{3-13}$$

where $\Updownarrow_{k_x}$ takes k_x to $-k_x$. The Hamiltonian $H(\mathbf{k})$ is said to have glide-plane symmetry if it commutes with the glide plane operator $[H(\mathbf{k}), G(\mathbf{k})] = 0$. It then follows that there are $\{N_1, N_1, N_2, N_2\}$-fold degenerate glide plane symmetry eigenvalues $\left\{+e^{-ik_y/2}, -e^{-ik_y/2}, +e^{-ik_x - ik_y/2}, -e^{-ik_x - ik_y/2}\right\}$. The simul-

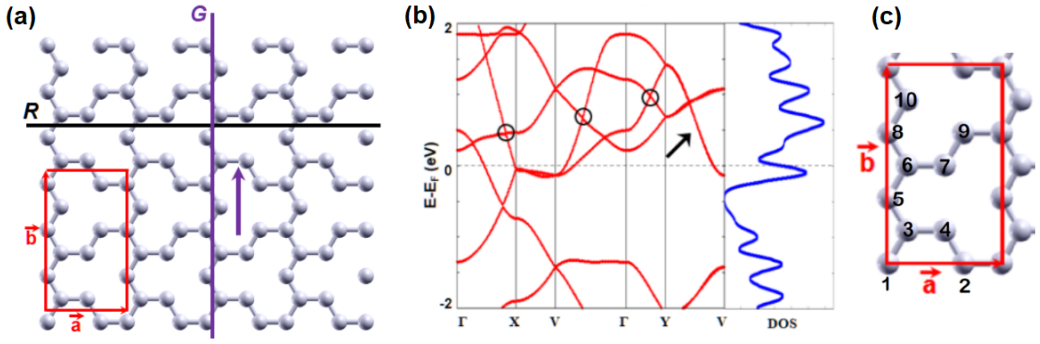

Figure 3.2: (a) Proposed C_{10} configuration that has 10 carbon atoms in the unit cell (red rectangle) defined by lattice vectors $\vec{a}$ and $\vec{b}$. The configuration contains a reflection plane R perpendicular to $\vec{b}$ and a nonsymmorphic glide plane G perpendicular to $\vec{a}$. (b) The resulting band structure of C_{10} along the high-symmetry line Γ-X-V-Γ-Y-V. The black arrows indicate the symmetry-enforced nodal lines, every two bands stick together becoming degerate in this range. The circles indicate accidental nodal lines inside the BZ. The right hand side of the figure shows the density of states of this band structure. (c) The numbering of carbon atoms in a unit cell.

taneous eigenstates of $G(\mathbf{k})$ and $H(\mathbf{k})$ satisfy

$$\begin{aligned} G(\mathbf{k})|\psi_{n1\pm}(\mathbf{k})\rangle &= \pm e^{-ik_y/2}\,\Updownarrow_{k_x}|\psi_{n1\pm}(\mathbf{k})\rangle, \\ G(\mathbf{k})|\psi_{n2\pm}(\mathbf{k})\rangle &= \pm e^{-ik_x-ik_y/2}\,\Updownarrow_{k_x}|\psi_{n2\pm}(\mathbf{k})\rangle, \\ H(\mathbf{k})|\psi_{nI\pm}(\mathbf{k})\rangle &= E_{nI\pm}(k_x,k_y)|\psi_{nI\pm}(\mathbf{k})\rangle. \end{aligned} \tag{3-14}$$

To see where this property comes from, consider the minimal situation of $N = 2$ sublattices as an example. In this case, the glide plane operator is $G(\mathbf{k}) = g(k_y)\,\Updownarrow_{k_x}$, and we may diagonalize it to obtain the eigenvalues

$$\begin{aligned} &g(\mathbf{k})|\phi_\pm(\mathbf{k})\rangle = \lambda_\pm(\mathbf{k})\,\Updownarrow_{k_x}|\phi_\pm(\mathbf{k})\rangle, = \begin{pmatrix} & e^{-ik_y} \\ 1 & \end{pmatrix}\Updownarrow_{k_x}\begin{pmatrix} u_\pm(k_x,k_y) \\ v_\pm(k_x,k_y)\end{pmatrix} \\ &= \begin{pmatrix} & e^{-ik_y} \\ 1 & \end{pmatrix}\begin{pmatrix} u_\pm(-k_x,k_y) \\ v_\pm(-k_x,k_y)\end{pmatrix} = \lambda_\pm(k_x,k_y)\,\Updownarrow_{k_x}\begin{pmatrix} u_\pm(k_x,k_y) \\ v_\pm(k_x,k_y)\end{pmatrix} \\ &= \lambda_\pm(k_x,k_y)\begin{pmatrix} u_\pm(-k_x,k_y) \\ v_\pm(-k_x,k_y)\end{pmatrix}, \end{aligned} \tag{3-15}$$

and hence one can solve for the coefficients $u_\pm(-k_x,k_y)$ and $v_\pm(-k_x,k_y)$ with eigenvalues that are just phases $\lambda_\pm = \pm e^{-ik_y/2}$. This property that eigenvalues that are just phases remains true for more number of glide pairs.

Notice that, at a fixed k_x, the Hamiltonian at $k_y = 0$ and $k_y = 2\pi$ is the same $H(k_x,0) = H(k_x,2\pi)$, and so is the glide-plane operator $G(k_x,0) = G(k_x,2\pi)$. Moroever, at a fixed k_x and band index n, the symmetry eigenvalues

at $k_y = 0$ and $k_y = 2\pi$ are,

$$\begin{aligned}
&G(k_x,0)|\psi_{n1\pm}(k_x,0)\rangle = \pm \Updownarrow_{k_x} |\psi_{n1\pm}(k_x,0)\rangle,\\
&G(k_x,2\pi)|\psi_{n1\pm}(k_x,2\pi)\rangle = \mp \Updownarrow_{k_x} |\psi_{n1\pm}(k_x,2\pi)\rangle,\\
&G(k_x,0)|\psi_{n2\pm}(k_x,0)\rangle = \pm e^{-ik_x} \Updownarrow_{k_x} |\psi_{n2\pm}(k_x,0)\rangle,\\
&G(k_x,2\pi)|\psi_{n2\pm}(k_x,2\pi)\rangle = \mp e^{-ik_x} \Updownarrow_{k_x} |\psi_{n2\pm}(k_x,2\pi)\rangle,
\end{aligned} \tag{3-16}$$

Combining these eigenvalues with $G(k_x,0) = G(k_x,2\pi)$ indicates that one must be able to find a gauge in which the eigenstates satisfy

$$\begin{aligned}
|\psi_{nI+}(k_x,0)\rangle &= |\psi_{nI-}(k_x,2\pi)\rangle,\\
|\psi_{nI-}(k_x,0)\rangle &= |\psi_{nI+}(k_x,2\pi)\rangle.
\end{aligned} \tag{3-17}$$

As a result, the eigenenergies must satisfy

$$\begin{aligned}
&H(k_x,0)|\psi_{nI+}(k_x,0)\rangle = E_{nI+}(k_x,0)|\psi_{nI+}(k_x,0)\rangle\\
&= H(k_x,2\pi)|\psi_{nI+}(k_x,2\pi)\rangle = E_{nI-}(k_x,2\pi)|\psi_{nI-}(k_x,2\pi)\rangle\\
&= E_{nI-}(k_x,2\pi)|\psi_{nI+}(k_x,0)\rangle,
\end{aligned} \tag{3-18}$$

since $H(k_x,0) = H(k_x,2\pi)$. This and a similar argument leads to

$$\begin{aligned}
E_{nI-}(k_x,2\pi) &= E_{nI+}(k_x,0),\\
E_{nI+}(k_x,2\pi) &= E_{nI-}(k_x,0).
\end{aligned} \tag{3-19}$$

Thus at given k_x, n, and I the two bands $E_{nI+}(k_x,k_y)$ and $E_{nI-}(k_x,k_y)$ must cross each other somewhere in $0 \le k_y \le 2\pi$.

We can now apply this argument to the BZ boundary $k_y = \pm\pi$, at which the eigenstates have symmetry eigenvalues

$$\begin{aligned}
&G(k_x,\pi)|\psi_{n1\pm}(k_x,\pi)\rangle = \mp i \Updownarrow_{k_x} |\psi_{n1\pm}(k_x,\pi)\rangle,\\
&G(k_x,-\pi)|\psi_{n1\pm}(k_x,-\pi)\rangle = \pm i \Updownarrow_{k_x} |\psi_{n1\pm}(k_x,-\pi)\rangle,
\end{aligned} \tag{3-20}$$

and similarly for the eigenstate with index $I = 2$. Because $G(k_x,\pi) = G(k_x,-\pi)$, we can always find a gauge in which the eigenstates satisfy

$$\begin{aligned}
|\psi_{nI+}(k_x,\pi)\rangle &= |\psi_{nI-}(k_x,-\pi)\rangle,\\
|\psi_{nI-}(k_x,\pi)\rangle &= |\psi_{nI+}(k_x,-\pi)\rangle.
\end{aligned} \tag{3-21}$$

Using $H(k_x, \pi) = H(k_x, -\pi)$, the same argument in Eq. (3-18) leads to

$$E_{nI+}(k_x, \pi) = E_{nI-}(k_x, -\pi) = E_{nI-}(k_x, \pi), \tag{3-22}$$

where we have used the fact that $k_y = \pi$ and $k_y = -\pi$ are the same point, thus completing the proof that every two bands must stick together at the BZ boundary $k_y = \pm\pi$.

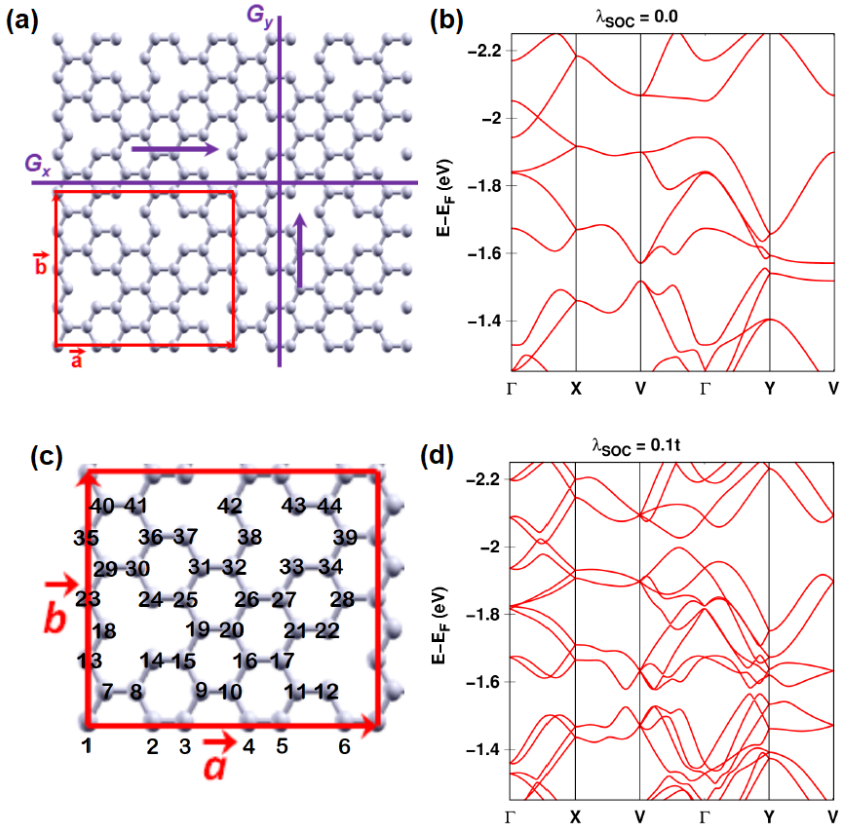

Figure 3.3: (a) The proposed C_{44} configuration that contains two orthogonal glide-planes G_x and G_y. (b) Band structure of C_{44} along the path Γ-X-V-Γ-Y-V, where the black arrows and circles indicate the symmetry-enforced and accidental nodal loops, respectively. The density of states of this configuration is shown at the right hand side. (c) The numbering of carbon atoms in this configuration. (d) The band structure of C_{44} in the presence of Rashba SOC.

3.3 Vacancy-engineered graphene with two orthogonal glide planes

It is also possible to vacancy-engineer a configuration that contain two orthogonal glide planes going along $\hat{\mathbf{x}}$ and $\hat{\mathbf{y}}$ directions. We should call the corresponding glide plane operators G_x and G_y. Figure 3.3(a) shows a C_{44} configuration that belongs to this situation, whose pattern is classified to be in the wallpaper group $p2gg$. The band structure solved by tight-binding model shown in Fig. 3.3 (b) indicates that every two bands stick together at the entire

BZ boundary in both x and y directions, foring the nodal loops, again owing to the nonsymmorphic symmetry. To understand the origin of these nodal loops, we also observe that in this C_{44} configuration, every two atoms map to each other under either one of the two glide plane operations. Using the numbering of atoms in Fig. 3.3 (c), the glide pairs defined with respect to the glide plane operator G_x are

$$\begin{aligned}
\text{Type}-\text{I}: \quad & (1,10), \quad (2,11), \quad (3,12), \quad (7,4), \\
& (8,5), \quad (9,6), \\
\text{Type}-\text{II}: \quad & (13,42), \quad (14,43), \quad (15,44), \quad (40,16), \\
& (41,17), \quad (18,38), \quad (19,39), \quad (35,20), \\
& (36,21), \quad (37,22), \quad (23,32), \quad (24,33), \\
& (25,34), \quad (29,26), \quad (30,27), \quad (31,28).
\end{aligned} \tag{3-23}$$

which ensures the band crossing at the BZ boundary in the x direction. On the other hand, for the glide plane G_y, the glide pairs are

$$\begin{aligned}
\text{Type}-\text{I}: \quad & (1,26), \quad (2,25), \quad (3,24), \quad (4,23), \\
& (7,32), \quad (8,31), \quad (9,30), \quad (10,29), \\
& (13,38), \quad (14,37), \quad (15,36), \quad (16,35), \\
& (18,42), \quad (19,41), \quad (20,40), \\
\text{Type}-\text{II}: \quad & (5,28), \quad (6,27), \quad (11,34), \quad (12,33), \\
& (17,39), \quad (21,44), \quad (22,43),
\end{aligned} \tag{3-24}$$

which ensure the band crossing at the BZ boundary in the y direction.

The mechanism for the nodal loops is very similar to that in the previous section for only one glide plane: Since the Hamiltonian commutes with both glide-plane operators, $[H(\mathbf{k}), G_{x,y}(\mathbf{k})] = 0$, we may label the eigenstates by the quantum numbers $\{n, \alpha, \beta\}$, where n is the band index, $\alpha = I_x\pm$ labels the eigenvalues of G_x, and $\beta = I_y\pm$ labels the eigenvalues of G_y. The eigenstates

have to satisfy

$$\begin{aligned}
G_x(\mathbf{k})|\psi_{n1\pm\beta}(\mathbf{k})\rangle &= \pm e^{-ik_x/2}\Updownarrow_{k_y}|\psi_{n1\pm\beta}(\mathbf{k})\rangle,\\
G_x(\mathbf{k})|\psi_{n2\pm\beta}(\mathbf{k})\rangle &= \pm e^{-ik_x/2-ik_y}\Updownarrow_{k_y}|\psi_{n2\pm\beta}(\mathbf{k})\rangle,\\
G_y(\mathbf{k})|\psi_{n\alpha1\pm}(\mathbf{k})\rangle &= \pm e^{-ik_y/2}\Updownarrow_{k_x}|\psi_{n\alpha1\pm}(\mathbf{k})\rangle,\\
G_y(\mathbf{k})|\psi_{n\alpha2\pm}(\mathbf{k})\rangle &= \pm e^{-ik_x-ik_y/2}\Updownarrow_{k_x}|\psi_{n\alpha2\pm}(\mathbf{k})\rangle,\\
H(\mathbf{k})|\psi_{n\alpha\beta}(\mathbf{k})\rangle &= E_{n\alpha\beta}(\mathbf{k})|\psi_{n\alpha\beta}(\mathbf{k})\rangle. \qquad (3\text{-}25)
\end{aligned}$$

Following the same argument for the case of only one glide plane in the previous section, we arrives at the conclusion that

$$\begin{aligned}
E_{n\alpha I_y\mp}(k_x,2\pi) &= E_{n\alpha I_y\pm}(k_x,0),\\
E_{nI_x\mp\beta}(2\pi,k_y) &= E_{nI_x\pm\beta}(0,k_y), \qquad (3\text{-}26)
\end{aligned}$$

i.e., there must be a band crossing in the range $0 \leq k_x \leq 2\pi$ at any fixed k_y, and another band crossing in the range $0 \leq k_y \leq 2\pi$ at any fixed k_x. The argument applied to the BZ boundary also leads to

$$\begin{aligned}
E_{n\alpha I_y-}(k_x,\pi) &= E_{n\alpha I_y+}(k_x,-\pi) = E_{n\alpha I_y+}(k_x,\pi),\\
E_{nI_x-\beta}(\pi,k_y) &= E_{nI_x+\beta}(-\pi,k_y) = E_{nI_x+\beta}(\pi,k_y). \qquad (3\text{-}27)
\end{aligned}$$

Thus every two bands must stick together at the BZ boundary, forming $N/2$ nodal loops surrounding the entire BZ boundary.

Having proposed various vacancy configurations, here we should make a remark concerning the experimental realization of our proposal. We anticipate that a particularly promising system is the so-called nanoporous graphene, which has realized graphene with periodic vacancies. In fact, a closer look at the experimental vacancy configuration realized in [35], called chevrontype nanoporous graphene (C-NPG), reveals that this configuration is actually nonsymmorphic. The C-NPG belongs to wallpaper group p2gg that contains glide planes in two orthogonal directions just like our C_{44} configuration. Therefore the C-NPG should contain nodal loops surrounding the entire BZ boundary according to our theory, which is in fact already confirmed by the DFT calculation (see Fig. 3 E of Ref. [30]), although this feature seems to have been overlooked in the experimental paper. This experimental confirmation not only proves that our theory is correct, but also points to the possibility to engineer nonsymmohphic vacancy configurations in reality, which seems very promising.

3.4 Effect of Rashba SOC on nodal lines and nodal loops

The nodal lines and loops are expected to be robust against various perturbations, provided the perturbations do not break the nonsymmorphic symmetry. In this section, we use C_{44} in the presence of Rashba SOC as an example to elaborate that even though the Rashba SOC lifts the spin degeneracy, the nodal loops are still protected by the nonsymmorphic symmetry. To elaborate this effect, we consider the tight-binding model of graphene in the presence of Rashba SOC described by

$$\begin{aligned} H &= t\sum_{\langle ij\rangle,\sigma} c_{i\sigma}^{\dagger}c_{j\sigma} + i\lambda_{SOC}\sum_{\langle ij\rangle,\alpha,\beta} c_{i\alpha}^{\dagger}\left(\boldsymbol{\sigma}_{\alpha\beta}\times\mathbf{d}_{ij}\right)^{z}c_{j\beta} \\ &\quad +U\sum_{i\in vac,\sigma} c_{i,\sigma}^{\dagger}c_{i\sigma}. \end{aligned} \tag{3-28}$$

Here λ_{SOC} is the strength of Rashba SOC assuming the breaking the inversion symmetry in the out-of-plane direction $\hat{\mathbf{z}}$, $\boldsymbol{\sigma} = (\sigma^x, \sigma^y, \sigma^z)$ are the Pauli matrices, $\mathbf{d}_{ij}$ is the vector connecting site i to site j.

The band structure of C_{44} solved by tight-binding model is shown in Fig. 3.3 (d). Note that in the band structure of pristine C_{44} without Rashba SOC shown in Fig. 3.3 (b), there is spin degeneracy everywhere in the BZ (every line in the band structure actually contains two lines), and moreover every two bands to stick together at the BZ boundary to form the nodal loops, so the nodal loops at the are in fact four-fold degenerate. In contrast, Fig. 3.3 (d) shows that when Rashba SOC is present, the spin degeneracy is lifted everywhere inside the BZ as expected (every line is only one line), but every two spin-split bands still merge together to form a two-fold degenerate nodal loop at the BZ boundary. We are lead to conclude that the Rashba SOC splits the spin degeneracy of the nodal loops and hence changes their degeneracy from four-fold to two-fold, the existence of nodal loops at the BZ boundary is still guaranteed by the nonsymmorphic symmetry.

3.5 Vacancy-engineered square lattice

Finally, as a proof of principle, we show that this vacancy engineering principle is not limited to the honeycomb lattice of graphene, but other types of square lattice too. To demonstrate this, in Fig. 3.4 (a) we show vacancy-engineered square lattice that belongs to wallpaper group $p4gm$, which contains two orthogonal glide planes. One expects that every two bands should stick together to form nodal loops at the entire BZ boundary, which is indeed

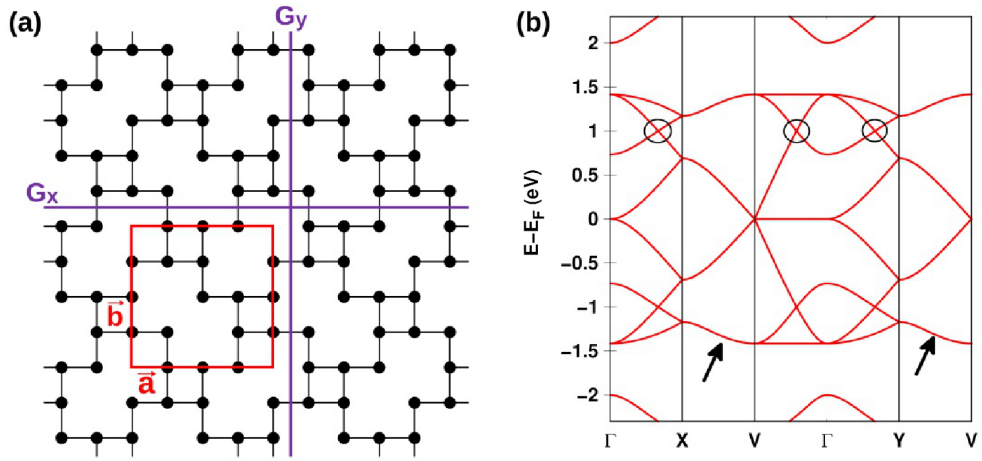

Figure 3.4: (a) A vacancy configuration engineered from a square lattice, which contains two orthogonal glide planes G_x and G_y. (b) The band structure of this configuration solved by tight-binding model plotted along high-symmetry lines, which contains nodal loops surrounding the entire BZ boundary as indicated by the arrows. The splitting of these nodal loops away from the BZ boundary also causes accidental band crossings as indicated by circles.

the case for the band structure shown in Fig. 3.4 (b) that is solved by a spinless tight-binding model with nearest-neighbor hopping. Thus our vacancy engineering principle that is solely based on on crystalline symmetries can indeed be ubiquitously applied to many different kind of 2D lattices regardless the structural and chemical details of the host system.

4
Flat-bands in vancancy-engineered structures

In the previous chapter, we show that periodic vacancies can change the crystalline symmetry and hence modify the band structure of graphene. In this chapter, we explore yet an other effect of periodic vacancies that can modify the band structure in a different way based on a different mechanism, namely flat bands caused by the rank-nullity theorem. The basic principle relies on the chiral symmetry of graphene, i.e., the nearest-neighbor hopping on the honeycomb lattice always connects between different sublattices. As a result, the Hamiltonian is block-off-diagonal. If we further introduce periodic vacancies in such a way that the numbers of two sublattices in a unit cell are different, then the blocks in the Hamiltonian is not square, and one is guaranteed to have zero energy flat bands due to the rank-nullity theorem.

The motivation of proposing a mechanism for zero energy flat bands is to draw analogy with that discovered in twisted bilayer graphene (TBLG). In particular, the flat bands therein is known to cause superconductivity. This further motivates us to investigate whether such a vacancy-engineered zero energy flat bands can support superconductivity. We will elaborate that, using the simplest mean field theory for phonon mediated superconductivity, these flat bands can indeed support s-wave superconductivity owing to the much enlarged density of states by the flat bands.

4.1
Rank-nullity theorem for flat bands in bipartite lattices

In this chapter, we revisit Lieb's theorem [13, 14], which is based on the rank-nullity theorem, with a special emphasis on the nonspatial symmetries, localization of the wave functions, and applications to periodic vacancies. We consider any two- (2D) or three-dimensional (3D) bipartite-lattices described by single-particle Hamiltonian $H(k)$ in momentum space that preserves time-reversal (TR), particle-hole (PH) chiral symmetries. These symmetries are particularly relevant to topological order and topological phase transitions [36, 37, 38, 39].

A bipartite lattice is one which can be partitioned in two disjoints partitions U and V, such that every edge connects a site in U to a site in

V. The results lattice has two sublattices that effectively don't interact with each other directly. There are a variety of example of bipartite lattice, such as the square lattice, and the graphene (honeycomb) lattice, and what will be elaborated in this chapter will hold for any bipartite lattice.

Bipartite lattices have the interesting property that its adjacency matrix can always be put in a anti-block-diagonal form by choosing the an appropriate basis and the chiral symmetry operators are implemented by $C = \sigma_3 K$. In particular, the basis $\left|\psi_1^A, \ldots, \psi_1^B, \ldots\right\rangle$, where $\left|\psi_i^A\right\rangle$ are states in the first partition and $\left|\psi_i^B\right\rangle$ are the states in the second partition, will make the adjacency matrix anti-block-diagonal. This is true because of the property of the bipartite lattice. By analogy, the Hamiltonian matrix of a bipartite lattice can also be written in a anti-block-diagonal form by choosing the same basis. In general, the Hamiltonian matrix of a bipartite lattice can be written as

$$H(\boldsymbol{k}) = \left(\begin{array}{c|c} & Q(\boldsymbol{k}) \\ \hline Q^\dagger(\boldsymbol{k}) & \end{array}\right) \tag{4-1}$$

where $Q(\boldsymbol{k})$ is a $N_A \times N_B$ matrix.

As a preliminary example, the square lattice as shown in Fig. 4.1. One possible of partitions is $U = \{A, C\}$ and $V = \{B, C\}$, in the basis of this partition the the nearest-neighbor tight binding model Hamiltonian matrix can be written as

$$H(\boldsymbol{k}) = \begin{pmatrix} 0 & 0 & te^{ik_x} & te^{-ik_y} \\ 0 & 0 & te^{-ik_y} & te^{ik_x} \\ te^{-ik_x} & te^{ik_y} & 0 & 0 \\ te^{ik_y} & te^{-ik_x} & 0 & 0 \end{pmatrix} \tag{4-2}$$

which is anti-block-diagonal.

The idea of creating ZEFBs goes back to Sutherland [13] and Lieb [14] in their seminal papers. The theorem states that a bipartite lattice with chiral symmetry will hold a ZEFB if there is a unbalance between the the number os sites in each partitions. Namely, if we call N_A and N_B the number of sites in the first and section partition, then if $N_A \neq N_B$ there will a zero energy eigenvalue. Indeed, we can see in Fig. 4.2 the Lieb lattice as stated in the theorem. One possible choice of partitions is $U = \{A\}$ and $V = \{B, C\}$, in the basis of this partition the Hamiltonian matrix can be written as

$$H(\boldsymbol{k}) = \begin{pmatrix} 0 & te^{ik_x} & te^{-ik_y} \\ te^{-ik_x} & 0 & 0 \\ te^{ik_y} & 0 & 0 \end{pmatrix} \tag{4-3}$$

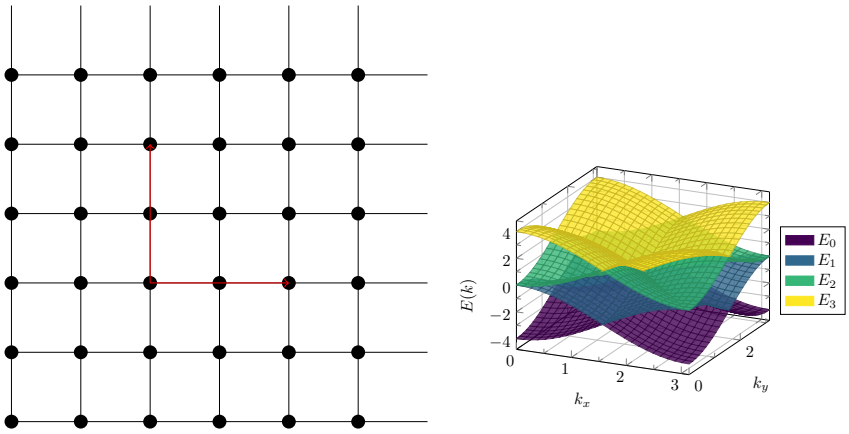

Figure 4.1: On the left, the square lattice with four sites and its unit cell and periodic boundary conditions. On the right, the spectrum of the Hamiltonian of the square lattice as a function of the wave vector.

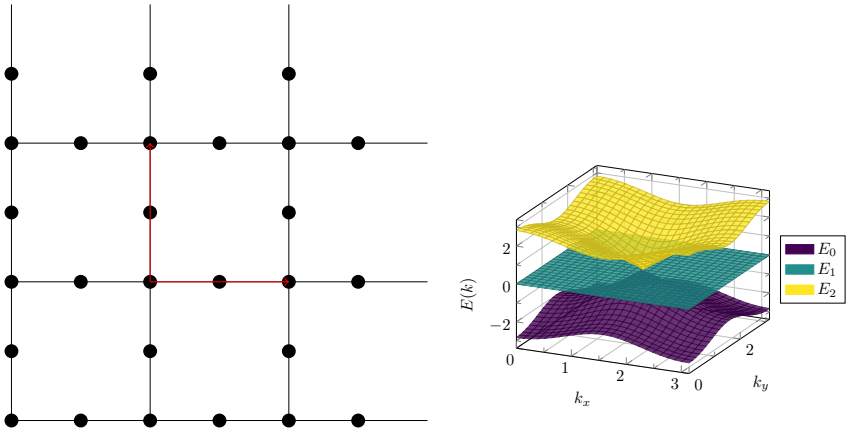

Figure 4.2: The Lieb lattice (left) and its band structure (right).

If we take a look at the band structure of the Lieb lattice, we can see that there is a zero-energy flat-band, this is a consequence of the Lieb theorem as previously stated. However, we can put this in another way, if we compare the lattices of the square lattice 4.1 and the lattice of the Lieb lattice 4.2, we can see that we can get the Lieb lattice from the square lattice by removing sites from the square lattice periodically. In fact, if we compare the Hamiltonians of the square lattice 4-2 and the Lieb lattice 4-3 , we can see that they are the same except for the last row and column. This means that if we remove the last row and column of the square lattice, we will get the Lieb lattice. This is the idea of vacancy-engineering.

In this section we explore properties which are very closely related to graph theory, a more thoroughly introduction to the topic refer to Appendix A.

The act of removing sites from a lattice is equivalent to removing the rows and columns of the Hamiltonian matrix. This procedure can have dramatic

effects on the band structure of the lattice as we could see in the example of the Lieb lattice. In fact, not only we will change the dimension of but we can also change rank of the Hamiltonian matrix, i.e the number of linearly independent rows or columns of the matrix. For practical purposes, instead of removing rows and columns, one can use a projecting procedures as explained in Appendix B. The connection between the rank of the Hamiltonian matrix and the zero-energy flat-band is given by the rank-nullity theorem.

Denoting $\mathrm{r}(H)$ as the rank and $\eta(H)$ as the nullity of a matrix H, our interest is how the nullity of the Hamiltonian $\eta(H)$, which counts the number of ZEFBs, can be nonzero. The rank-nullity theorem can be stated as follows

$$\mathrm{r}(H) + \eta(H) = \dim(H), \tag{4-4}$$

i.e, the rank of a matrix plus its nullity is equal to its dimension. We refer rank of H as the column-rank of H, as opposite but equal to row-rank, by convention. In either case, we have that the column-rank equals the row-rank. In the case of bipartite lattices, the Hamiltonian matrix takes the form 4-1, and the rank-nullity theorem can be applied to both H and Q separately, namely

$$\begin{aligned} \mathrm{r}(H) + \eta(H) &= N_A + N_B, \\ \mathrm{r}(Q) + \eta(Q) &= N_A. \end{aligned} \tag{4-5}$$

Notice that we have organized the basis such that the first N_A entries are in the A sublattice and the remaining N_B are in the B sublattice. Moreover,

$$\mathrm{r}(H) = \mathrm{r}(Q) + \mathrm{r}(Q^\dagger) = 2rQ(r), \tag{4-6}$$

where we use used the fact that

$$\mathrm{r}(Q) = \mathrm{r}(Q^\dagger) = r(QQ^\dagger) = r(Q^\dagger Q). \tag{4-7}$$

This comes from the fact that $\eta(Q^\dagger Q) = \eta(Q)$ and $\eta(QQ^\dagger) = \eta(Q^\dagger)$, combined with Eq. 4-5. Let $|\psi\rangle$ be an eigenvector of Q with eigenvalue zero with muliplicity $\eta(Q)$, then $|\psi\rangle$ is also an eigenvector of $Q^\dagger Q$ with eigenvalue zero with the same muliplicity. For instance,

$$\mathrm{r}(QQ^\dagger) + \eta(QQ^\dagger) = N_A, \tag{4-8}$$

$$\mathrm{r}(QQ^\dagger) + \eta(Q^\dagger) = N_A, \tag{4-9}$$

$$\mathrm{r}(QQ^\dagger) + N_A - \mathrm{r}(Q^\dagger) = N_A, \tag{4-10}$$

$$\mathrm{r}(QQ^\dagger) = \mathrm{r}(Q^\dagger). \tag{4-11}$$

Now we want to show that in the case $N_A \neq N_B$ and, without loss of generality, assuming that $N_B > N_A$, we recover the Lieb theorem. From

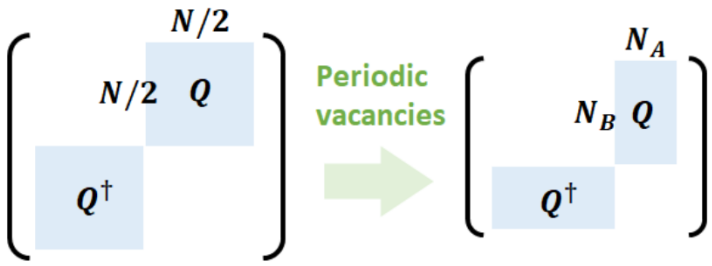

Figure 4.3: Proposed procedure for creating ZEFBs generically. Initially, we have the Hamiltonian $H(\boldsymbol{k})$ of a bipartite lattice which is $N \times N$. The Q and $Q^\dagger$ matrices are square and both $N/2 \times N/2$. After introducing periodic vacancies, removing columsn and rows from the Hamiltonian, Q becomes rectangular $N_B \times N_A$ and $Q^\dagger$ becomes $N_A \times N_B$. We show that in this situation we will have ZEFBs.

Eqs. 4-5 and 4-6

$$\begin{aligned} \eta(H) &= N_A + N_B - \mathrm{r}(H), && (4\text{-}12)\\ &= N_A + N_B - 2\mathrm{r}(Q), && (4\text{-}13)\\ &= N_A + N_B - 2(N_A - \eta(Q)), && (4\text{-}14)\\ &= N_B - N_A + 2\eta(Q). && (4\text{-}15) \end{aligned}$$

From Eq. 4-15, we conclude that that $\eta(H) > 0$ if Q is not square, since $N_B > N_A$ and $\eta(Q) \geq 0$. Moreover, if $\eta(Q) = 0$

$$\eta(H) = N_B - N_A. \tag{4-16}$$

This means that ZEFBs must emerge if we remove the two sublattices in different quantities. In this case, we would have a situation where the Hamiltonian matrix H itself is square but the matrices Q and $Q^\dagger$ individually are not as can be seen in Fig. 4.3.

Next, we want to show that the wave-function of the flat-band will be localized at the majority sublattice. To prove this, we start by applying the rank-nullity theorem to the bilinear forms $Q^\dagger Q$ and $QQ^\dagger$, namely

$$\begin{aligned} \mathrm{r}(QQ^\dagger) + \eta(QQ^\dagger) &= N_B.\\ \mathrm{r}(Q^\dagger Q) + \eta(Q^\dagger Q) &= N_A, \end{aligned} \tag{4-17}$$

Using 4-7 and the discussion thereafter, we conclude that

$$\eta(QQ^\dagger) - \eta(Q^\dagger Q) = N_B - N_A. \tag{4-18}$$

Additionally, we notice that Hamiltonian squared is a block diagonal matrix which has the form in Eq. 4-19 and has the same nullity as the Hamiltonian

itself, namely $\eta(H) = \eta(H^2)$, since for every $|\psi\rangle$ with $H|\psi\rangle = 0$ we have $H^2|\psi\rangle = 0$.

$$H^2(\boldsymbol{k}) = \left(\begin{array}{c|c} Q(\boldsymbol{k})Q^\dagger(\boldsymbol{k}) & \\ \hline & Q^\dagger(\boldsymbol{k})Q(\boldsymbol{k}) \end{array}\right). \tag{4-19}$$

We use $H^2(\boldsymbol{k})$ to prove this proposition, namely

$$\eta(H^2) = \eta(H) = \eta(Q^\dagger Q) + \eta(QQ^\dagger) = N_B - N_A. \tag{4-20}$$

If Q itself is not singular, i.e., $\eta(Q) = 0$, which is true in many practical examples, $\eta(Q^\dagger Q) = 0$ and from Eq. 4-20, we have $\eta(QQ^\dagger) = N_B - N_A$. If we inspect the matrix form of the Hamiltonian squared in Eq. 4-19, we see that the zero eigenvalues come individually from the first block $Q(\boldsymbol{k})Q^\dagger(\boldsymbol{k})$. This means that the wave-functions for the zero-energy flat-band must vanish at the A sublattice and are localized in the majority sublattice, B in this case.

We can achieve zero-energy flat-bands in bipartite lattices by introducing the following procedure which is described in Fig.4.3. We enlarge the unit cell to contain $N =$ even number of sites with the same amount of two sublattices, then the Hamiltonian matrix arranged in the basis $\left|\psi_1^A, \ldots, \psi_{N/2}^A \psi_1^B, \ldots, \psi_{N/2}^B\right\rangle$ remains block-off-diagonal. The chiral symmetry operator is implemented by $C = \sigma_3 \otimes \mathbf{I}_{N/2}$, where $\mathbf{I}_{N/2}$ is the $N/2 \times N/2$ identity matrix. Then we introduce periodic vacancies into the lattice, the columns and rows in the Hamiltonian matrix that correspond to the vacancy sites will be removed. If the number of vacancies on the A and B sublattices are different, then the unit cell will contain a different number of sublattices $N_A \neq N_B$. As a result, the $Q(k)$ 4-4 as an $N_A \times N_B$ matrix will not be a square matrix. Nevertheless, the chiral symmetry of the system still holds, since removing the columns and rows that correspond to the vacancy sites does not break it. As a result, the band structure at any vacancy configuration will hold a zero-energy flat band (ZEFB) and it wave functions associated to it must be localized on one of the two sublattices since they are eigenstates of the chiral operator S as we have proved above.

In the following sections, we examine these propositions in the context of spinless honeycomb lattice with nearest-neighbor hopping, which is relevant to the p_z orbital of single-layer graphene. For practical porpuses, we focus on the large on-site potential regime $U > 100t$ that completely removes the vacancy sites and is equivalent to the vacancy engineering proposed in this section.

4.2 Flat bands in honeycom lattice with nearest-neighbor hopping

A promising system to realize the flat bands discussed in the previous section is the honeycomb lattice with only nearest-neighbor hopping and appropriate periodic vacancies. In this case, the honeycomb lattice is bipartite, so we can apply the chiral symmetry and rank-nullity theorem discussed in the previous section to address the formation of flat bands. In the next section, will discuss the application of this idea to graphene and the complications that we may encounter in reality. The honeycomb lattice with nearest-neighbor hopping and periodic vacancies is described by the spinless Hamiltonian

$$H = \sum_{\langle ij \rangle} t\, c_i^\dagger c_j + U \sum_{i \in v} c_i^\dagger c_i, \tag{4-21}$$

where $U = 100t$ is a large on-site potential that conveniently projects out the vacancy sites $i \in v$. We denote the vacancy configurations by $\mathrm{C}_{N_A+N_B}$ in order to draw relevant to graphene in the next section. In Fig. 4.4 (a), we show two examples that can realize flat bands. The first is a C_{15} configuration given by removing a single A sublattice from a $N = 16$ rectangular unit cell such that $N_A = 7$ and $N_B = 8$, which has a rectangular BZ. The band structure plotted in Fig. 4.4 (b) along a high-symmetry line is PH symmetric and contains a single ZEFB throughout the BZ. The second configuration is the C_{14} shown in the right panel of Fig. 4.4 (a) that removes two A sublattices on the same 16-site unit cell, such that $N_A = 6$ and $N_B = 8$. The band structure shown in Fig. 4.4 (b) has doubly degenerate ZEFBs $\eta(H) = N_B - N_A = 2$, consistent with our theory in the previous section. In Fig. 4.4 (c), we also show the wave functions of the ZEFBs for C_{15} and C_{14}, which are both are localized on the majority B sublattices. In addition, in Fig. 4.4 (c) we plot the wave functions of the single flat band of C_{15} and doubly degenerate flat bands of C_{14} at some randomly selected momentum $\mathbf{k}$, confirming that all these wave functions are localized in the majority B sublattice. All these features are in full agreement with the rank-nullity theorem and chiral symmetry presented in the previous section, which encourages us to examine the feasibility of this idea in a realistic graphene, which will be addressed in the next section.

4.3 Nearly Flat bands in graphene with periodic vacancies

Since the results in the previous section points to the possibility of realizing the ZEFBs on a honeycomb lattice, we are motivated to investigated the

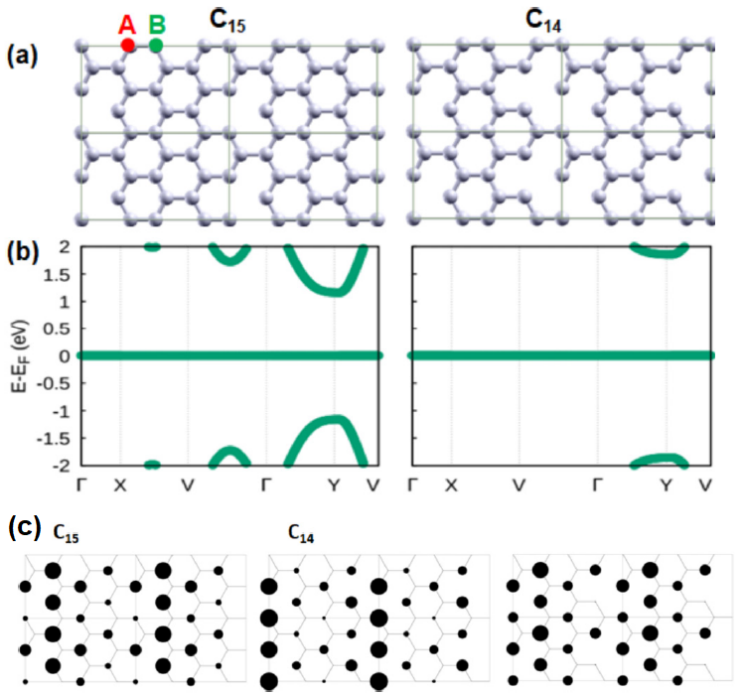

Figure 4.4: (a) The lattice structures of two vacancy configurations C_{15} (left column) and C_{14} (right column) that are proposed to have ZEFBs if the Hamiltonian preserves chiral symmetry. This is confirmed in (b), that shows the band structure along a path in the Brillouin Zone, which indicates a single ZEFB for C_{15} and doubly degenerate ZEFBs for C_{14}. Although now visible, we confirm numerically that there are two ZEFBs in the C_{14} configuration. (c) The wave functions $|\psi_i|^2$ at momentum $\mathbf{k} = (0.15, 0.37)$ of the single ZEFB of C_{15} and the two degenerate ZEFBs of C_{14}. Only the B sublattice is visible, since the wave-function vanish at the A sublattice. The largest circles correspond to $|\psi_i|^2 = 0.313$.

feasibility of this idea on graphene. The realistic graphene, however, contains a fair amount of complications that can break the chiral symmetry that our theory relies on [18]. Of all these complications, the biggest deal breaker is presumably the next-nearest-neighbor hopping t', since it is between the same sublattices and hence enters the diagonal elements of the momentum space Hamiltonian, redering the off-block-diagonal form inappropriate. However, the next-nearest-neighbor hopping t' is also known to be an order of magnitude smaller than the nearest-neighbor hopping t, so one would expect that some features of the ZEFBs should remain.

To examine this issue, we examine a spinless honeycomb lattice tight-binding model that contains both nearest-neighbor and next-nearest-neighbor hoppings

$$H = \sum_{\langle ij \rangle} t\, c_i^\dagger c_j + \sum_{\langle\langle ij \rangle\rangle} t'\, c_i^\dagger c_j - \sum_i \mu c_i^\dagger c_i + U \sum_{i \in v} c_i^\dagger c_i, \tag{4-22}$$

where $t = 2.8$eV and $t' = -0.2$eV, similar to the realistic values on graphene, and we again use $U > 100t$ to project out the impurity sites. We have also include a chemical potential μ into the discussion for the purpose that will become more clear in the next section. Applying this tight-binding model to the C_{15} and C_{14} configurations shown in Fig. 4.4 (a) yields the band structure shown in Fig. 4.5 (a). One sees that althouth the ZEFBs are no longer perfectly flat, they still have a fairly narrow band width. In addition, plotting the narrow band wave functions in real space reveals that they are still highly localized in the majority B sublattice. Thus we conclude that the band structure and wave function still retain many features of the ZEFBs owing to the fact that the chiral symmetry-breaking term is much smaller than the symmetry-preserving terms $t' \ll t$. We notice that, along with the chiral symmetry, the particle-hole symmetry is also broken. We can understand this by writing the particle-hole operator S as $S = TC$, where T is the time-reversal operator and C is the chiral operator. Since time-reversal is preserved by vacancy-engineerig, we conclude that hiral symmetry breaking leads to particle-hole symmetry breaking.

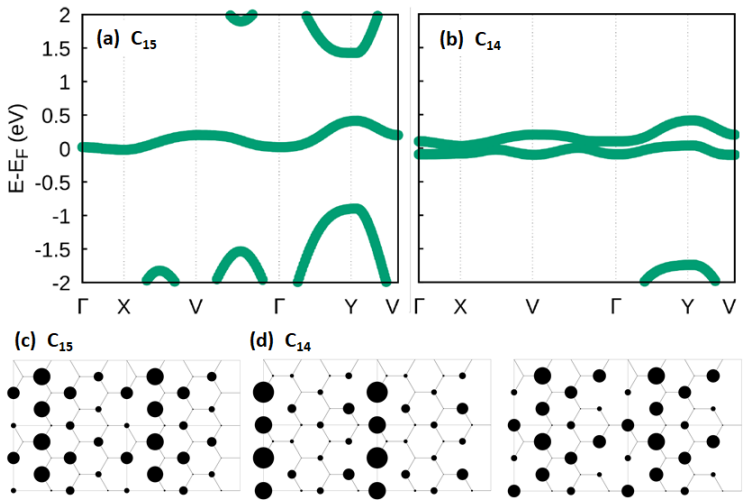

Figure 4.5: Band structures of (a) C_{15} and (b) C_{14} simulated by a tight-binding model with nearest-neighbor $t = 2.8$eV and next-nearest-neighbor $t' = -0.2$eV hoppings, and a chemical potential $\mu = 0.2$eV. The ZEFBs are no longer perfectly flat, but nevertheless still have a fairly narrow band width. The wave functions $|\psi_i|^2$ of the narrow bands at momentum $\mathbf{k} = (0.15, 0.37)$ are shown in (c) and (d). We see that they are still highly localized on the majority B sublattices, but there is a small but non-zero wave-function at the A sublattice.

4.4 Superconductivity stabilized by vacancy-engineered narrow bands in graphene

The very narrow bands in these vacancy-engineered graphene inherented from the ZEFBs obviously contributes to a huge density of states (DOS) near the Fermi surface, which is expected to dramatically change the electronic and magnetic properties of the holey graphene. In addition, we know that the phonon band width in graphene is about $\omega_D \approx 0.25$eV [40, 41, 42], meaning that the narrow bands with band width ~ 0.5eV in a large area of the BZ are within the Debye frequency. This seems to suggest a large phase space for phonon-mediated Cooper pairing [43]. Motivated by this simple phase space argument, we proceed to examine whether a conventional phonon-mediated s-wave SC phase can occur in these holey graphene with the help of these low energy narrow bands. To examine this possibility, we examine a spinful mean-field model of s-wave SC described by

$$\begin{aligned} H &= \sum_{\langle ij\rangle\sigma} t\, c^\dagger_{i\sigma} c_{j\sigma} + \sum_{\langle\langle ij\rangle\rangle\sigma} t'\, c^\dagger_{i\sigma} c_{j\sigma} - \sum_{i\sigma} \mu\, c^\dagger_{i\sigma} c_{i\sigma} \\ &\quad + \sum_i \left(\Delta_i c^\dagger_{i\uparrow} c^\dagger_{i\downarrow} + \Delta^*_i c_{i\downarrow} c_{i\uparrow}\right) + U \sum_{i\in v} c^\dagger_{i\sigma} c_{i\sigma}, \end{aligned} \tag{4-23}$$

where we use $t = 2.8$eV, $t' = -0.2$eV and $\mu = 0.2$eV. Here Δ_i is the local pairing amplitude at site i, and the on-site potential $U > 100t$ that projects out the vacancy sites $i \in v$.

We solve the mean field Hamiltonian by means of Bogoliubov-de Gennes transformation. The formalism seeks to diagonalize Eq. (4-23) by $H = \text{const.} + \sum_{\mathbf{k}\alpha} E_{\mathbf{k}} \gamma^\dagger_{\mathbf{k}\alpha} \gamma_{\mathbf{k}\alpha}$ using a Bogoliubov transformation

$$\begin{aligned} c_{i\uparrow} &= \sum_{\mathbf{k}} \gamma_{\mathbf{k}\uparrow} u_{\mathbf{k}}(i) - \gamma^\dagger_{\mathbf{k}\downarrow} v^*_{\mathbf{k}}(i), \\ c_{i\downarrow} &= \sum_{\mathbf{k}} \gamma_{\mathbf{k}\downarrow} u_{\mathbf{k}}(i) + \gamma^\dagger_{\mathbf{k}\uparrow} v^*_{\mathbf{k}}(i), \end{aligned} \tag{4-24}$$

where $i = 1, 2 \ldots N_A + N_B$ denotes the site inside a unit cell, and $\gamma_{\mathbf{k}\sigma}$ is the annihilation operator of the Bogoliubov quasiparticles. The wave functions

$\{u_{\mathbf{k}}(i), v_{\mathbf{k}}(i)\}$ and eigenenergy $E_{\mathbf{k}}$ satisfy

$$\begin{aligned} E_{\mathbf{k}} u_{\mathbf{k}}(i) &= \sum_{\langle ij \rangle} t\, u_{\mathbf{k}}(j) + \sum_{\langle\langle ij \rangle\rangle} t'\, u_{\mathbf{k}}(j) \\ &\quad + U\delta_{i\in v} u_{\mathbf{k}}(i) + \Delta_i v_{\mathbf{k}}(i), \\ E_{\mathbf{k}} v_{\mathbf{k}}(i) &= -\sum_{\langle ij \rangle} t\, v_{\mathbf{k}}(j) - \sum_{\langle\langle ij \rangle\rangle} t'\, v_{\mathbf{k}}(j) \\ &\quad - U\delta_{i\in v} v_{\mathbf{k}}(i) + \Delta_i^* u_{\mathbf{k}}(i). \end{aligned} \tag{4-25}$$

The pairing amplitude at site i is determined from these Bogoliubov coefficients by

$$\Delta_i = \sum_{\mathbf{k}} V\theta(\omega_D - E_{\mathbf{k}})\,[2f(E_{\mathbf{k}}) - 1]\, u_{\mathbf{k}}(i) v_{\mathbf{k}}^*(i), \tag{4-26}$$

where $f(E_{\mathbf{k}}) = (e^{E_{\mathbf{k}}/k_B T} + 1)^{-1}$ is the Fermi distribution. The pairing interaction $V < 0$ is nonzero only within Debye frequency $\omega_D = 0.25$eV, which is ensured by the step function $\theta(\omega_D - E_{\mathbf{k}})$. Equations (4-25) and (4-26) are solved self-consistently until the local pairing amplitude Δ_i converges. In addition, we consider only s-wave pairing since the wave function of the narrow bands is highly localized on the same sublattices as shown in Fig. 4.4 and (4.5), suggeting that on-site pairing is the most likely.

In Fig. 4.6 (a) and (b), we show the numerical result for the local gap Δ_i at zero temperature for the two configurations C_{15} and C_{14} in Fig. 4.4. Both configurations render a finite Δ_i, indicating that a conventional phonon-mediated pairing can indeed be stabilized by the vacancy-engineered narrow bands and can be captured by our simple mean field theory. The pairing Δ_i on the B sublattices is about two orders of magnitude larger than that on the A sublattices, owing to the narrow band wave functions that are highly localized on the B sublattice as shown in Fig. 4.5, despite the chiral symmetry is weakly broken. For C_{15}, the spatially averaged gap $\Delta(T) = \sum_i \Delta_i/(N_A + N_B)$ at zero temperature $\Delta(0)$ only becomes sizable the pairing potential has roughly the same strength as the hopping $|V| \sim t$, implying that SC in C_{15} can only be induced by a sufficiently strong electron-phonon interaction. In contrast, C_{14} requires much smaller $|V|$ to trigger SC, suggesting that increasing the number of narrow bands does help to create the SC phase, in agreement with the expectation that a larger DOS at the Fermi surface helps to stabilize SC.

The temperature dependence of the spatially averaged gap exhibits a behavior similar to that in the usual weak coupling mean field theory. The critical temperature T_c is found to be higher at larger pairing potential V, as

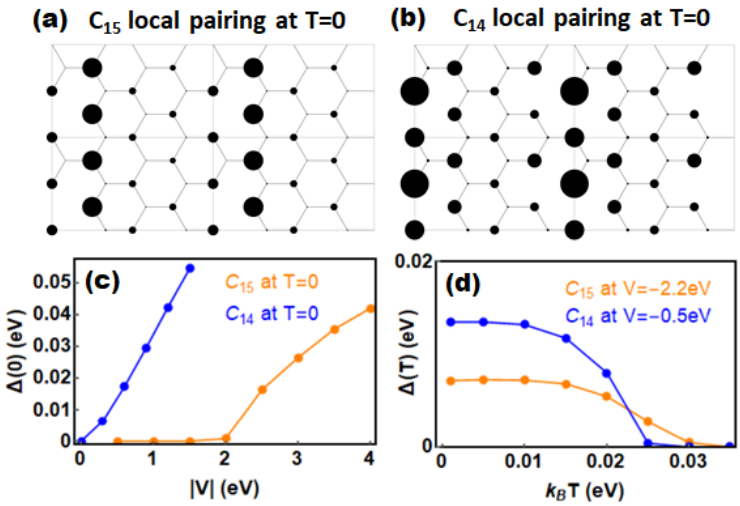

Figure 4.6: (a) Local pairing amplitude Δ_i for the C_{15} configuration in Fig. 4.4, calculated at zero temperature and pairing interaction $V = -2.2$eV. The circles indicate the magnitude of the pairing, with largest circles correspond to $\Delta_i = 0.036$eV. (b) Δ_i for the C_{14} configuration in Fig. 4.4 at zero temperature and $V = -0.5$eV, where the largest circles correspond to $\Delta_i = 0.074$eV. In both (a) and (b), One sees that the majority B sublattices have much larger pairing amplitude. (c) Spatially averaged pairing amplitude at zero temperature $\Delta(0)$ versus the pairing interaction $|V|$. (d) The spatially average pairing amplitude $\Delta(T)$ as a function of temperature.

expected. Besides, we also find that T_c generally increases with the number of narrow bands, consistent with that expected from an enlarged DOS. Note that since the proposed mechanism based on chiral symmetry and rank-nullity theorem has no restriction on the number of narrow bands $N_B - N_A$ (times 2 if including spin) it can create, we anticipate that the vacancy configurations with very different numbers of the two sublattices, i.e., many such narrow bands, may be able to produce a very high T_c.

5
Quantum metric and fidelity number of Dirac materials

In this chapter, we examine the quantum geometrical properties of general D-dimensional Dirac models. Our purpose is to give an overview on the notion of quantum geometry in topological materials, including several new aspects that we have introduced, and then in the next chapter we will apply this formalism particularly to graphene and discuss several experimental measurables.

The concept of quantum geometry arises from considering the filled band Bloch state $|u(\mathbf{k})\rangle$ of a insulator, semiconductor, or superconductor, and regard the Brillouin zone (BZ) as a compact D-dimensional T^D torus. The overlap of the filled band Bloch state at momentum $\mathbf{k}$ and a slightly different momentum $\mathbf{k}+\delta\mathbf{k}$ defines a so-called quantum metric [44]. Once the metric is defined, one can discuss various aspects in differential geometry on the BZ manifold, such as geodesic and scalar curvature. From a physical point of view, a particular motivation to investigate the quantum metric is its relation with the topological order, since it is recently shown that the integrant that integrates to a universal topological invariant is always related to the deteminant of the quantum metric [45]. As a result, one can extract some information about the topological order through measuring the profile of quantum metric in momentum space, which is proposed to be feasible in pump-probe type of experiments.

In a recent work, we suggest that the integration of quantum metric over momentum space can easily be measured by means of optical absorption experiments [46]. This quantity is interesting because the BZ is a very special kind of manifold from the point of view of differential geometry, namely it is a T^D torus. As a result, the integration of quantum metric over momentum actually represents a kind of average distance between neighboring Bloch states in the BZ, of which we call the fidelity number. What is even more interesting is that, as we will elaborate in the following sections, the spectral function of the fidelity number turns out to be related to the optical absorption power that has been measured in semiconductors for decades [47]. Our theory therefore gives a quantum geometrical interpretation of the optical absorption power, as we shall elaborate particularly for TIs described by Dirac models.

5.1 Quantum geometry of gapped materials

The notion of quantum geometry starts by the introduction of quantum metric. In general, for a quantum state $|u(\mathbf{k})\rangle$ that depends on some parameters $\mathbf{k} = (k_1, k_2...)$, the quantum metric $g_{\mu\nu}$ is introduced from the overlap the quantum state at slightly different parameters [44]

$$|\langle u(\mathbf{k})|u(\mathbf{k}+\delta\mathbf{k})\rangle| = 1 - \frac{1}{2}g_{\mu\nu}\delta k^\mu \delta k^\nu, \tag{5-1}$$

i.e., it is the prefactor of the leading order expansion (which is second order) in the small parameter difference δk. A straightforward expansion gives the explicit expression

$$g_{\mu\nu}(\mathbf{k}) \;=\; \frac{1}{2}\langle\partial_\mu u|\partial_\nu u\rangle + \frac{1}{2}\langle\partial_\nu u|\partial_\mu u\rangle - \langle\partial_\mu u|u\rangle\langle u|\partial_\nu u\rangle. \tag{5-2}$$

In particular, we aim to apply this concept to TIs and TSCs described by the Dirac Hamiltonian and Bloch eigenstates $H(\mathbf{k})|\ell^{\mathbf{k}}\rangle = \epsilon_\ell^{\mathbf{k}}|\ell^{\mathbf{k}}\rangle$, where $\mathbf{k} = (k_1, k_2...k_D)$ is the D-dimensional crystalline momentum that is treated as a tuning parameter. We will reserve the index n for valence bands, m for conduction bands, ℓ for all the bands, and likewisely for the summations $\{\sum_n, \sum_m, \sum_\ell\}$.

To be more specific, suppose there are N_- valence band states of TIs or quasihole states of TSCs with negative energy $\epsilon_n < 0$, and at zero temperature they are all filled. Thus the reason able starting point is the fully antisymmetric valance band state [48] $|u^{\rm val}(\mathbf{k})\rangle$

$$|u^{\rm val}(\mathbf{k})\rangle = \frac{1}{\sqrt{N_-!}}\epsilon^{n_1 n_2 ... n_{N-}}|n_1^{\mathbf{k}}\rangle|n_2^{\mathbf{k}}\rangle...|n_{N_-}^{\mathbf{k}}\rangle, \tag{5-3}$$

where the $|u_a^-(\mathbf{k})\rangle$ form a basis of the N_- filled bands (with negative energy). To calculate the quantum metric of this state, one may use the second-quantization formalism with fermionic annihilation operators c_ℓ. The derivative over momentum in this formalism can be written as

$$\frac{\partial}{\partial k^\mu} = \sum_{\ell\ell'}\langle\ell'|\partial_\mu|\ell\rangle c_{\ell'}^\dagger c_\ell. \tag{5-4}$$

Applying this derivative on the fully antisymmetric filled band state $|u^{\rm val}\rangle =$

$\prod_{n=1}^{N_-} c_n^\dagger|0\rangle$ gives

$$|\partial_\mu u^{\rm val}\rangle = \sum_{n=1}^{N_-}\left(\langle n|\partial_\mu n\rangle + \sum_{m=1}^{N_+}\langle m|\partial_\mu n\rangle c_m^\dagger c_n\right)|u^{\rm val}\rangle, \tag{5-5}$$

from which it follows that

$$\begin{aligned}\langle u^{\rm val}|\partial_\mu u^{\rm val}\rangle &= \sum_{n=1}^{N_-}\langle n|\partial_\mu n\rangle \\ \langle\partial_\mu u^{\rm val}|\partial_\nu u^{\rm val}\rangle &= \left(\sum_{n=1}^{N_-}\langle\partial_\mu n|n\rangle\right)\left(\sum_{n=1}^{N_-}\langle n|\partial_\nu n\rangle\right) \\ &\quad + \sum_{n=1}^{N_-}\langle\partial_\mu n|Q_+|\partial_\nu n\rangle,\end{aligned} \tag{5-6}$$

where we have defined the projectors to the empty m and filled n band states

$$Q_+ \equiv \sum_{m=1}^{N_+}|m\rangle\langle m|, \quad Q_- \equiv \sum_{n=1}^{N_-}|n\rangle\langle n|. \tag{5-7}$$

Applying Eqs. (5-5) and (5-6) to Eq. (5-2), we obtain the expression for the quantum metric of this fully antisymmetric filled band state

$$g_{\mu\nu}(\mathbf{k}) = \frac{1}{2}\sum_{nm}\left(\langle\partial_\mu n|m\rangle\langle m|\partial_\nu n\rangle + \langle\partial_\nu n|m\rangle\langle m|\partial_\mu n\rangle\right). \tag{5-8}$$

For practical calculation we can use the Hellman-Feynman relations

$$\langle m|\partial_\mu n\rangle = \frac{\langle m|\,\partial_\mu H\,|n\rangle}{E_n - E_m}, \tag{5-9}$$

$$\langle\partial_\nu m|m\rangle = \frac{\langle n|\,\partial_\nu H\,|m\rangle}{E_n - E_m}, \tag{5-10}$$

which can be proved under the assumption of adiabatic change of the Hamiltonian and is well defined for gapped system. Under this assumption we can write the quantum metric as

$$g_{\mu\nu}(\mathbf{k}) = \frac{1}{2}\sum_{nm}\frac{\langle n|\,\partial_\mu H\,|m\rangle\,\langle m|\,\partial_\nu H\,|n\rangle}{(E_n - E_m)^2} + (\mu \leftrightarrow \nu). \tag{5-11}$$

We further introduce a quantum metric spectral function by

$$g_{\mu\nu}(\mathbf{k},\omega) = \frac{1}{2}\sum_{nm}\Big(\langle\partial_\mu n|m\rangle\langle m|\partial_\nu n\rangle + \langle\partial_\nu n|m\rangle\langle m|\partial_\mu n\rangle\Big) \tag{5-12}$$

$$\times\,\delta\left(\omega + \frac{\varepsilon_n^{\mathbf{k}}}{\hbar} - \frac{\varepsilon_m^{\mathbf{k}}}{\hbar}\right). \tag{5-13}$$

Obviously, this spectral function frequency-integrates to the quantum metric

$$g_{\mu\nu}(\mathbf{k}) = \int d\omega\, g_{\mu\nu}(\mathbf{k},\omega). \tag{5-14}$$

Experimentally, this spectral function describes the optical absorption at momentum $\mathbf{k}$. We can see this by considering the current operator in momentum space $\hat{j}_\mu = e\partial_\mu H$, where $H = H(\mathbf{k})$ is the momentum space single-particle Hamiltonian, and we will assume a D-dimensional cubic lattice of unit cell volume a^D. From the usual linear response theory, the zero temperature longitudinal optical conductivity at momentum $\mathbf{k}$ at frequency of the light ω is

$$\begin{aligned}\sigma_{\mu\mu}(\mathbf{k},\omega) &= \sum_{nm}\frac{\pi}{a^D\hbar\omega}\langle n|\hat{j}_\mu|m\rangle\langle m|\hat{j}_\mu|n\rangle\delta\left(\omega + \frac{\varepsilon_n^{\mathbf{k}}}{\hbar} - \frac{\varepsilon_m^{\mathbf{k}}}{\hbar}\right)\\ &= \frac{\pi e^2}{a^D}\hbar\omega\, g_{\mu\mu}(\mathbf{k},\omega),\end{aligned} \tag{5-15}$$

which can be used to extract the diagonal components of the quantum metric spectral function $g_{\mu\mu}(\mathbf{k},\omega)$.

We proceed to consider the momentum-integration of the quantum metric

$$G_{\mu\nu} = \int \frac{d^D\mathbf{k}}{(2\pi)^D} g_{\mu\nu}(\mathbf{k}), \tag{5-16}$$

of which we call the fidelity number. Since the BZ is a torus, the fidelity number has the physical meaning as a measure of the average distance between neighboring Bloch states in the BZ manifold: A large $G_{\mu\mu}$ means that the Bloch state $|u(\mathbf{k})\rangle$ as a unit vector in the Hilbert space rotates very dramatically as the momentum $\mathbf{k}$ changes just a little bit along μ direction. As a result, the fidelity number is a characteristic quantum geometric property of the system. We may further intriduce a fidelity number spectral function by momentum-integrating the quantum metric spectral function in Eq. (5-13), which obviously

frequency-integrates to the fidelity number

$$G_{\mu\nu}(\omega) = \int \frac{d^D\mathbf{k}}{(2\pi)^D} g_{\mu\nu}(\mathbf{k},\omega), \quad G_{\mu\nu} = \int d\omega\, G_{\mu\nu}(\omega). \tag{5-17}$$

The significance of $G_{\mu\nu}(\omega)$ is that it is directly related to the optical absorption power of insulating or semiconducting materials: If we consider the optical conductivity of a gapped material measured in real space, then it is given by the momentum integration of the optical conductivity at momentum $\mathbf{k}$

$$\begin{aligned}\sigma_{\mu\mu}(\omega) &= \int \frac{d^D\mathbf{k}}{(2\pi\hbar/a)^D}\, \sigma_{\mu\mu}(\mathbf{k},\omega) \\ &= \frac{\pi e^2}{\hbar^{D-1}}\,\omega \int \frac{d^D\mathbf{k}}{(2\pi)^D}\, g^d_{\mu\mu}(\mathbf{k},\omega) \equiv \frac{\pi e^2}{\hbar^{D-1}}\,\omega\, \mathcal{G}^d_{\mu\mu}(\omega),\end{aligned} \tag{5-18}$$

Now we consider a D-dimension material subject to a polarized oscillating field of the light $E_\mu(\omega,t) = E_0\cos\omega t$, where E_0 is the strength of the electric field. The oscillating field induces an oscillating current $j_\mu(\omega,t) = \sigma_{\mu\mu}(\omega)E_0\cos\omega t$ and hence dissipates energy. As a result, the optical absorption power per unit cell at frequency ω is

$$W_a(\omega) = \langle j_\mu(\omega,t)E_\mu(\omega,t)\rangle_t = \frac{1}{2}\sigma_{\mu\mu}(\omega)E_0^2 = \frac{\pi e^2}{2\hbar^{D-1}}\, E_0^2\omega\, \mathcal{G}^d_{\mu\mu}(\omega), \tag{5-19}$$

where $\langle ...\rangle_t$ denotes the time average. As we can see, the optical absorption power is directly given by frequency times the fidelity number spectral function $\mathcal{G}_{\mu\mu}(\omega)$. In other words, the absorption power divided by frequency can be used to extract $\mathcal{G}_{\mu\mu}(\omega)$, and if one further integrates it over frequency then the fidelity number is obtained.

5.2 Quantum metric for Dirac models

In the case of Dirac Hamiltonians, where we can write it in the form

$$H(\mathbf{k}) = \mathbf{d}(\mathbf{k})\cdot\sigma,$$

where $\mathbf{d}(\mathbf{k}) = (d_1(\mathbf{k}), d_2(\mathbf{k}), d_3(\mathbf{k}))$ and $\sigma = (\sigma_x,\sigma_y,\sigma_z)$ is the Pauli vector. The eigenvalues and eigenvectors for this class of Hamiltonians have a special form, to see this first we write in general

$$H(k) = \begin{pmatrix} d_3(\mathbf{k}) & d_1(\mathbf{k}) - id_2(\mathbf{k}) \\ d_1(\mathbf{k}) + id_2(\mathbf{k}) & -d_3(\mathbf{k}) \end{pmatrix}.$$

The eigenvalues are

$$E_{\pm}\left(\mathbf{k}\right)=\pm\left|\mathbf{d}\right|,$$

and the eigenvectors are

$$\begin{aligned}\psi_{+}\left(\mathbf{k}\right)&=\frac{1}{\sqrt{2d\left(d_{3}+d\right)}}\left(d_{3}+d,d_{1}+id_{2}\right),\\ \psi_{-}\left(\mathbf{k}\right)&=\frac{1}{\sqrt{2d\left(d_{3}+d\right)}}\left(id_{2}-d_{1},d_{3}+d\right).\end{aligned}\tag{5-20}$$

Consider the following quantity

$$\mathbf{n}=\frac{\mathbf{d}}{d}=\frac{\left(d_{1},d_{2},d_{3}\right)}{\sqrt{d_{1}^{2}+d_{2}^{2}+d_{3}^{2}}},\tag{5-21}$$

and the partial differentiation of the jth component with respect to $k_{\alpha}=\alpha$ momenta, the first component is

$$\partial_{\alpha}\mathbf{n}_{j}=\partial_{\alpha}\left(\frac{d_{j}}{\sqrt{d_{1}^{2}+d_{2}^{2}+d_{3}^{2}}}\right)=\frac{-d_{j}\left(d_{1}\partial_{\alpha}d_{1}+d_{2}\partial_{\alpha}d_{2}+d_{3}\partial_{\alpha}d_{3}\right)+d^{2}\partial_{\alpha}d_{j}}{d^{3}},\tag{5-22}$$

such that

$$\partial_{\alpha}\mathbf{n}_{j}=\left(\partial_{\alpha}\mathbf{n}_{x},\partial_{\alpha}\mathbf{n}_{y},\partial_{\alpha}\mathbf{n}_{z}\right).$$

Now consider the bilinear form

$$g_{\alpha\beta}\left(\mathbf{k}\right)=\left(\partial_{\alpha}\mathbf{n}_{\alpha}\right)\cdot\left(\partial_{\alpha}\mathbf{n}_{\beta}\right),$$

which we want to relate to the quantum metric in. First let us consider one component which will appear when we expand of such bilinear form

$$\left(\partial_{\alpha}\mathbf{n}_{i}\right)\left(\partial_{\beta}\mathbf{n}_{j}\right)=\frac{\left(-\frac{1}{2}d_{i}\left(d\partial_{\alpha}d\right)+d^{2}\partial_{\alpha}d_{i}\right)\left(-\frac{1}{2}d_{j}\left(d\partial_{\beta}d\right)+d^{2}\partial_{\beta}d_{j}\right)}{d^{6}}\tag{5-23}$$

$$=\frac{d_{i}d_{j}d^{2}\left(\partial_{\alpha}d\right)\left(\partial_{\beta}d\right)-\frac{1}{2}\left(\partial_{\alpha}d\right)d^{3}d_{i}\partial_{\beta}d_{j}-\frac{1}{2}\left(\partial_{\beta}d\right)d^{3}d_{i}\partial_{\alpha}d_{i}+d^{4}\partial_{\alpha}d_{i}\partial_{\beta}d_{j}}{d^{6}}\tag{5-24}$$

where $d\partial_{\alpha}d=d_{1}\partial_{\alpha}d_{1}+d_{2}\partial_{\alpha}d_{2}+d_{3}\partial_{\alpha}d_{3}$. If $i=j$ then

$$\left(\partial_\alpha \mathbf{n}_i\right)\left(\partial_\beta \mathbf{n}_i\right)=\frac{d_i^2 d^2\left(\partial_\alpha d\right)\left(\partial_\beta d\right)-\frac{1}{2} d^3\left(\left(\partial_\alpha d\right) d_i \partial_\beta d_i+\left(\partial_\beta d\right) d_i \partial_\alpha d_i\right)+d^4 \partial_\alpha d_i \partial_\beta d_i}{d^6}.$$

After summing over i we have

$$\begin{aligned} g_{\alpha\beta}\left(\mathbf{k}\right) &= \frac{d^4\left(\partial_\alpha d\right)\left(\partial_\beta d\right)-d^4\left(\left(\partial_\alpha d\right)\left(\partial_\beta d\right)+\left(\partial_\beta d\right)\left(\partial_\alpha d\right)\right)+d^4\left(\partial_\alpha \mathbf{d}\right)\cdot\left(\partial_\beta \mathbf{d}\right)}{d^6}, \\ &= \frac{\left(\partial_\alpha d\right)\left(\partial_\beta d\right)-\left(\partial_\alpha d\right)\left(\partial_\beta d\right)+\left(\partial_\alpha \mathbf{d}\right)\cdot\left(\partial_\beta \mathbf{d}\right)}{d^2}, \\ &= \frac{1}{4}\frac{\left(\partial_\alpha \mathbf{d}\right)\cdot\left(\partial_\beta \mathbf{d}\right)-\left(\partial_\alpha d\right)\left(\partial_\beta d\right)}{d^2}, \end{aligned} \tag{5-25}$$

which is the desired form for the quantum metric and where the term of $\frac{1}{4}$ comes from the dimension of the Dirac model.

5.3 Applications

In the following section we will apply the quantum metric to a few for different dimensions. For the 1D case we will consider the SSH model, which is a model for topological phase transition. For the 2D case we will consider the Lieb lattice. For the 3D case we will consider the Weyl semimetal model,which is a model for topological phase transition. Finally, we will consider the Dirac model in D-dimensions and show that there is a closed form for the fidelity number and the quantum metric spectral function.

5.3.1 SSH Model

The SSH model is a 1D model with topological phase transition [49], the lattice model is given as

$$H\left(k\right)=t\left(M-1+\cos k\right)\sigma_x+t\sin k\sigma_y.$$

In this model, the topological phase transition occur at $M=0$. The low energy approximation is given by expanding in the leading order in k

$$H\left(k\right)=M\sigma_x+v_F k\sigma_y,$$

and the quantum metric is given as

$$g\left(k\right)=\frac{M^2}{4\left(v_F^2k^2+M^2\right)^2}.$$

As per usual we want to calculate the integral

$$G = \frac{1}{4\,(2\pi)} \int_0^\infty dk \frac{M^2}{\left(v_F^2 k^2 + M^2\right)^2},$$

making the change of variables

$$k = \frac{M}{v_F} \tan \xi, \tag{5-26}$$

$$dk = \frac{M}{v_F} \sec^2 \xi d\xi, \tag{5-27}$$

then

$$G = \frac{1}{8\pi v_F M} \int_0^{\pi/2} \frac{d\xi}{\sec^2 \xi} = \frac{1}{8\pi v_F M} \int_0^1 \frac{t^2 dt}{\sqrt{1-t^2}} = \frac{1}{32 v_F M},$$

which is finite but diverges at the phase transition $M = 0$. We define the spectral function as

$$G = \frac{1}{4\,(2\pi)} \int_0^\infty dk \frac{M^2}{\left(k^2 + M^2\right)^2} \delta\left(\omega + \epsilon_- + \epsilon_+\right) \left[f\left(\epsilon_-\right) - f\left(\epsilon_+\right)\right], \tag{5-28}$$

$$= \frac{1}{8\pi} \int_0^\infty dk \frac{M^2}{\left(v_F^2 k^2 + M^2\right)^2} \delta\left(\omega - 2\sqrt{v_F^2 k^2 + M^2}\right) \tanh\left(\frac{v_F \sqrt{v_F^2 k^2 + M^2}}{k_B T}\right), \tag{5-29}$$

making the same change of variables

$$G = \frac{1}{8\pi v_F M} \int_0^{\pi/2} \frac{d\xi}{\sec^2 \xi} \delta\left(\omega - 2\left|M \sec \xi\right|\right) \tanh\left(\frac{v_F \left|M \sec \xi\right|}{2 k_B T}\right), \tag{5-30}$$

$$= \frac{1}{8\pi v_F M} \int_0^1 dt \frac{t^2}{\sqrt{1-t^2}} \delta\left(\omega - \frac{2\left|M\right|}{t}\right) \tanh\left(\frac{v_F \left|M\right|}{t 2 k_B T}\right) \tag{5-31}$$

$$= \frac{M^2}{\pi v_F \omega^3 \sqrt{\omega^2 - 4M^2}} \tanh\left(\frac{v_F \omega}{4 k_B T}\right) \Theta\left(\omega > 2M\right) \tag{5-32}$$

As we can see, for value of ω bigger than the gap $2M$ the spectral function is finite.

5.3.2 Lieb lattice

The Lieb lattice has three sites in their unit-cell, it can be thought to be a square lattice with one site removed. In this sense it is a bipartite lattice with unbalanced number of sites in the partitions, it has therefore a zero

eigenvalues independent of momenta, i.e. a zero-energy flat-band. The tight-binding Hamiltonian describing this system is

$$H(k) = \begin{pmatrix} 0 & X & Y \\ X & 0 & 0 \\ Y & 0 & 0 \end{pmatrix}, \tag{5-33}$$

where $X = 2t\cos\frac{k_x}{2}$and $Y = 2t\cos\frac{k_y}{2}$. The eigenvalues are

$$E_0 = 0, \tag{5-34}$$

$$E_\pm = \pm R, \tag{5-35}$$

where $R = \sqrt{X^2 + Y^2}$. The eigenvectors are

$$|u_0\rangle = \frac{1}{N_0}\left(0, Y, -X\right)^T, \tag{5-36}$$

$$|u_\pm\rangle = \frac{1}{N_\pm}\left(1, \pm\frac{X}{R}, \pm\frac{Y}{R}\right), \tag{5-37}$$

with their respective normalization factors. Using expression (5-11) we write down the auxiliary derivative of the Hamiltonian

$$\partial_{k_x} H = \begin{pmatrix} 0 & \partial X & 0 \\ \partial X & 0 & 0 \\ 0 & 0 & 0 \end{pmatrix}, \tag{5-38}$$

$$\partial_{k_y} H = \begin{pmatrix} 0 & 0 & \partial Y \\ 0 & 0 & 0 \\ \partial Y & 0 & 0 \end{pmatrix}, \tag{5-39}$$

where $\partial X = -t\sin\frac{k_x}{2}$and $\partial Y = -t\sin\frac{k_y}{2}$. The quantum metric components then are

$$g_{xx}(k) = \frac{(\partial X)^2 Y^2}{4R^4} = \frac{\sin^2\frac{k_x}{2}\cos^2\frac{k_y}{2}}{16\cos^4\frac{k_y}{2} + 32\cos^2\frac{k_x}{2}\cos^2\frac{k_y}{2} + 16\cos^4\frac{k_x}{2}}, \tag{5-40}$$

$$g_{yy}(k) = \frac{X^2(\partial Y)^2}{4R^4} = \frac{\cos^2\frac{k_x}{2}\sin^2\frac{k_y}{2}}{16\cos^4\frac{k_y}{2} + 32\cos^2\frac{k_x}{2}\cos^2\frac{k_y}{2} + 16\cos^4\frac{k_x}{2}}, \tag{5-41}$$

$$g_{xy}(k) = g_{yx}(k) = \frac{X\partial X Y\partial Y}{4R^4} = \frac{-\cos\frac{k_x}{2}\sin\frac{k_x}{2}\cos\frac{k_y}{2}\sin\frac{k_y}{2}}{16\cos^4\frac{k_y}{2} + 32\cos^2\frac{k_x}{2}\cos^2\frac{k_y}{2} + 16\cos^4\frac{k_x}{2}}. \tag{5-42}$$

5.3.3 Weyl Semimetal

The 3D Weyl semimetal can put in lattice model such that [50]

$$H(\boldsymbol{k}) = t\sin k_x\sigma_x + t\sin k_y\sigma_y + t\left(2 + M - \cos k_x - \cos k_y - \cos k_z\right)\sigma_z.$$

The low energy approximation is obtained by expanding close to the Weyl nodes $K = (0, 0, \pm k_0)$,where $\cos k_0 = M$. Setting $M = 0$ we get $k_0 = \frac{\pi}{2}$ and expanding in the leading order we get

$$H(\boldsymbol{q} + \boldsymbol{K}) = \boldsymbol{d}\cdot\boldsymbol{\sigma},$$

where $\boldsymbol{d} = v_F\left(k_x, k_y, k_z + M\right)$

As always, the quantum metric is given by 5-25 and for this particular case we have

$$g_{\alpha\beta}(\boldsymbol{k}) = \frac{1}{4\left(k_x^2 + k_y^2 + (k_z + M)^2\right)^2}\begin{pmatrix} k_y^2 + (k_z + M)^2 & -k_xk_y & -k_x(k_z + M) \\ -k_xk_y & k_x^2 + (k_z + M)^2 & -k_y(k_z + M) \\ -k_x(k_z + M) & -k_y(k_z + M) & k_x^2 + k_y^2 \end{pmatrix}.$$

Integrating the $g_{xx}(\boldsymbol{k})$ component over the spherical coordinates

$$G_{xx} = \frac{1}{(2\pi)^3}\int d^3\boldsymbol{k}\, g_{xx}(\boldsymbol{k}) = \frac{1}{4(2\pi)^3}\int_0^{2\pi} d\phi\int_0^{\pi}\sin\theta d\theta\int_0^{\infty} k^2dk\frac{k^2\sin^2\phi\sin^2\theta + (k\cos\theta + M)^2}{\left(k^2\sin^2\theta + (k\cos\theta + M)^2\right)^2}. \tag{5-43}$$

Making the change of variables

$$\xi = \frac{k}{M}\cos\theta, \tag{5-44}$$

$$\xi = -\frac{k}{M}\sin\theta d\theta, \tag{5-45}$$

we have

$$G_{xx} = \frac{\pi M}{4\left(2\pi\right)^3}\int_0^\infty kdk\int_{-\frac{k}{M}}^{\frac{k}{M}} d\xi \frac{k^2 - M^2\xi^2 + 2M^2\left(\xi+1\right)^2}{\left(k^2 - M^2\xi^2 + M^2\left(\xi+1\right)^2\right)^2} \tag{5-46}$$

$$= \frac{1}{32\pi^2}\int_0^\infty dk\frac{k^2}{M^2} + \frac{k\left(k^2-3M^2\right)}{4M^3}\log\left(\frac{k^2-M^2}{k^2+M^2}\right) \tag{5-47}$$

which diverges. Defining the quantum metric spectral function as

$$G_{xx}\left(\omega\right) = \frac{1}{\left(2\pi\right)^3}\int d^3\boldsymbol{k} g_{xx}\left(\boldsymbol{k}\right)\delta\left(\omega - \epsilon_+ + \epsilon_-\right)\left(f\left(\epsilon_-\right) - f\left(\epsilon_+\right)\right), \tag{5-48}$$

$$= \frac{1}{12\pi^2}\int_0^\infty dk\delta\left(\omega - \epsilon_+ + \epsilon_-\right)\left(f\left(\epsilon_-\right) - f\left(\epsilon_+\right)\right). \tag{5-49}$$

Using $\epsilon_\pm = \pm v_F k$then

$$G_{xx}\left(\omega\right) = \frac{1}{12\pi^2}\int_0^\infty dk\delta\left(\omega - 2v_F k\right)\tanh\frac{v_F k}{2k_B T} = \frac{\tanh\frac{v_F\omega}{4k_B T}}{24\pi^2 v_F},$$

and we observe that, with temperature, the quantum metric is linear with frequency.

5.3.4 In D-dimensions

In general, the Hamiltonian describing a topological insulator in d-dimensions is [36, 37]

$$H\left(\boldsymbol{k}\right) = d_0\gamma_0 + \sum_{i=1}^{D-1} d_i\gamma_i, \tag{5-50}$$

where $\gamma_i$are the Dirac gamma matrices in D-dimensions and

$$\boldsymbol{d} = \left(M, vk_1, vk_2, \ldots, vk_{d-1}\right).$$

In this case equation (5-25) takes the form [51]

$$g_{\alpha\beta}\left(\boldsymbol{k}\right) = \frac{N}{8}\frac{\left(\partial_\alpha\boldsymbol{d}\right)\cdot\left(\partial_\beta\boldsymbol{d}\right) - \partial_\alpha d\partial_\beta d}{d^2}, \tag{5-51}$$

where N is the dimension of the γ_i matrices, for $N = 2$, for example, γ_i matrices are simply the Pauli matrices σ_i. We focus only on the diagonal elements because the integration over the non-diagonal ones is zero. With (5-50) and (5-51) we have

$$g_{\alpha\alpha}\left(\boldsymbol{k}\right) = \frac{N}{8}\frac{v^2k^2 - v^2k_\alpha^2 + M^2}{\left(v^2k^2+M^2\right)^2} = \frac{N}{8}\frac{1}{v^2k^2+M^2} - \frac{N}{8}\frac{v^2k_\alpha^2}{\left(v^2k^2+M^2\right)^2}, \tag{5-52}$$

and we wish to integrate this expression in generalized spherical coordinates in D-dimensions as

$$\begin{aligned} G_{\alpha\alpha} &= \int \frac{d^D\boldsymbol{k}}{(2\pi)^D} g_{\alpha\alpha}(\boldsymbol{k}), \\ &= \frac{N\Omega_d}{8(2\pi)^D}\int_0^\infty k^{D-1}dk\frac{v^D}{v^2k^2+M^2} - \frac{N\Lambda_D^\alpha}{8(2\pi)^D}\int_0^\infty k^{D+1}dk\frac{v^{D+2}}{(v^2k^2+M^2)^2}, \end{aligned} \tag{5-53}$$

where we have defined two numerical constants, the first one is

$$\Omega_D = \begin{cases} 1, & \text{for } n=1 \\ \frac{2\pi^{\frac{D}{2}}}{\Gamma\left(\frac{D}{2}\right)} & \text{for } n>1 \end{cases} \tag{5-54}$$

is the surface of a n-ball with radius one. The second one is Λ_n^α, the integration over the n-ball of radius one of the cartesian α-coordinate. Consider first only the $\alpha = x_1$ coordinate, we can calculate its first values

$$\Lambda_1^1 = 1 \tag{5-55}$$

$$\Lambda_2^1 = \int_0^{2\pi}\cos^2\phi d\phi = \pi \tag{5-56}$$

$$\Lambda_3^1 = \int_0^{2\pi} d\phi\int_0^\pi \sin\theta d\theta \sin^2\theta\cos^2\phi = \frac{4\pi}{3} \tag{5-57}$$

$$\Lambda_4^1 = \int_0^{2\pi} d\phi\int_0^\pi \sin^2\theta_1 d\theta_1\int_0^\pi \sin\theta_2 d\theta_2 \sin^2\theta_1\sin^2\theta_2\cos^2\phi = \frac{\pi^2}{2} \tag{5-58}$$

$$\Lambda_5^1 = \int_0^{2\pi} d\phi\int_0^\pi \sin^3\theta_1 d\theta_1\int_0^\pi \sin^2\theta_2 d\theta_2\int_0^\pi \sin\theta_3 d\theta_3 \sin^2\theta_1\sin^2\theta_2\sin^2\theta_3\cos^2\phi = \frac{8\pi^2}{15} \tag{5-59}$$

We notice that for $n>1$ there is a closed formula for the expression above

$$\Lambda_n^1 = \int_0^{2\pi}\cos^2\phi d\phi\int_0^\pi \sin^n\theta_1 d\theta_1\int_0^\pi \sin^{n-1}\theta_2 d\theta_2\int_0^\pi \sin^{n-2}\theta_3 d\theta_3\ldots\int_0^\pi \sin^3\theta_N d\theta_N \tag{5-60}$$

$$= \pi\prod_{i=3}^{n}\frac{\sqrt{\pi}\Gamma\left(\frac{1+i}{2}\right)}{\Gamma\left(1+\frac{i}{2}\right)} = \frac{\pi^{\frac{n}{2}}}{\Gamma\left(1+\frac{n}{2}\right)} = \frac{2\pi^{\frac{n}{2}}}{n\Gamma\left(\frac{n}{2}\right)} \tag{5-61}$$

Using the results above, we can define

$$\Lambda_D^1 = \begin{cases} 1, & \text{for } D=1 \\ \frac{2\pi^{\frac{D}{2}}}{D\Gamma\left(\frac{D}{2}\right)}, & \text{for } D>1 \end{cases}. \tag{5-62}$$

This formula is also true for the second component because $\int_0^{2\pi} d\phi \sin^2(\phi) = \int_0^{2\pi} d\phi \cos^2(\phi) = \pi$. For the last component $\alpha = x_N$, which would be z-component in 3-dimensional space we can proceed similarly

$$\Lambda_1^N = 1 \tag{5-63}$$

$$\Lambda_2^N = \int_0^{2\pi} \cos^2\theta d\theta = \pi \tag{5-64}$$

$$\Lambda_3^N = \int_0^{2\pi} d\phi \int_0^{\pi} \sin\theta d\theta \cos^2\theta = \frac{4\pi}{3} \tag{5-65}$$

$$\Lambda_4^N = \int_0^{2\pi} d\phi \int_0^{\pi} \sin^2\theta_1 d\theta_1 \int_0^{\pi} \sin\theta_2 d\theta_2 \cos^2\theta_1 = \frac{\pi^2}{2} \tag{5-66}$$

$$\Lambda_5^N = \int_0^{2\pi} d\phi \int_0^{\pi} \sin^3\theta_1 d\theta_1 \int_0^{\pi} \sin^2\theta_2 d\theta_2 \int_0^{\pi} \sin\theta_3 d\theta_3 \cos^2\theta_1 = \frac{8\pi^2}{15} \tag{5-67}$$

We see that $\Lambda_n^N = \Lambda_n^1$. We can prove this by noticing that

$$\Lambda_D^N = \int_0^{2\pi} d\phi \int_0^{\pi} \sin^{D-2}\theta_1 \cos^2\theta_1 d\theta_1 \int_0^{\pi} \sin^{D-3}\theta_2 d\theta_2 \ldots \int_0^{\pi} \sin\theta_3 d\theta_3 \tag{5-68}$$

$$= 2\pi \int_0^{\pi} \sin^{D-2}\theta_1 \left(1 - \sin^2\theta_1\right) d\theta_1 \int_0^{\pi} \sin^{D-3}\theta_2 d\theta_2 \ldots \int_0^{\pi} \sin\theta_3 d\theta_3 \tag{5-69}$$

$$= 2\pi \int_0^{\pi} \sin^{D-2}\theta_1 d\theta_1 \int_0^{\pi} \sin^{D-3}\theta_2 d\theta_2 \ldots \int_0^{\pi} \sin\theta_3 d\theta_3 - \tag{5-70}$$

$$2\pi \int_0^{\pi} \sin^{D}\theta_1 d\theta_1 \int_0^{\pi} \sin^{D-3}\theta_2 d\theta_2 \ldots \int_0^{\pi} \sin\theta_3 d\theta_3 \tag{5-71}$$

$$= 2\pi \prod_{i=1}^{D-2} \frac{\sqrt{\pi}\Gamma\left(\frac{1+i}{2}\right)}{\Gamma\left(1+\frac{i}{2}\right)} - 2\pi \frac{\sqrt{\pi}\Gamma\left(\frac{1+D}{2}\right)}{\Gamma\left(1+\frac{n}{2}\right)} \prod_{i=1}^{D-3} \frac{\sqrt{\pi}\Gamma\left(\frac{1+i}{2}\right)}{\Gamma\left(1+\frac{i}{2}\right)} = \frac{\pi^{\frac{D}{2}}}{\Gamma\left(1+\frac{D}{2}\right)} = \Lambda_D^1. \tag{5-72}$$

If we consider $D > 3$ the third component $\alpha = x_3$ would be

$$\Lambda_4^3 = \int_0^{2\pi} d\phi \int_0^{\pi} \sin^2\theta_1 d\theta_1 \int_0^{\pi} \sin\theta_2 d\theta_2 \sin^2\theta_1 \cos^2\theta_2 = \frac{\pi^2}{2} \tag{5-73}$$

$$\Lambda_5^3 = \int_0^{2\pi} d\phi \int_0^{\pi} \sin^3\theta_1 d\theta_1 \int_0^{\pi} \sin^2\theta_2 d\theta_2 \int_0^{\pi} \sin\theta_3 d\theta_3 \sin^2\theta_1 \sin^2\theta_2 \cos^2\theta_3 = \frac{8\pi^2}{15} \tag{5-74}$$

which has the closed form

$$\Lambda_D^3 = \int_0^{2\pi} d\phi \int_0^{\pi} \sin^D \theta_1 d\theta_1 \int_0^{\pi} \sin^{D-1} \theta_2 d\theta_2 \int_0^{\pi} \sin^{D-2} \theta_3 d\theta_3 \ldots \int_0^{\pi} \sin\theta_N \cos^2 \theta_N d\theta_N \tag{5-75}$$

$$= \int_0^{2\pi} d\phi \int_0^{\pi} \sin^D \theta_1 d\theta_1 \int_0^{\pi} \sin^{D-1} \theta_2 d\theta_2 \int_0^{\pi} \sin^{D-2} \theta_3 d\theta_3 \ldots \int_0^{\pi} \sin\theta_N \left(1 - \sin^2 \theta_N\right) d\theta_N \tag{5-76}$$

$$= 4\pi \int_0^{\pi} \sin^D \theta_1 d\theta_1 \int_0^{\pi} \sin^{D-1} \theta_2 d\theta_2 \int_0^{\pi} \sin^{D-2} \theta_3 d\theta_3 \ldots \int_0^{\pi} \sin^4 \theta_{N-1} d\theta_{N-1} - \Lambda_n^1 \tag{5-77}$$

$$= 4\pi \prod_{i=4}^{D} \frac{\sqrt{\pi}\Gamma\left(\frac{1+i}{2}\right)}{\Gamma\left(1+\frac{i}{2}\right)} - \Lambda_D^1 = 2\frac{\pi^{\frac{D}{2}}}{\Gamma\left(1+\frac{D}{2}\right)} - \Lambda_D^1 = \Lambda_D^1 \tag{5-78}$$

and is also equal to the fourth component $\alpha = x_4$. In fact all of the Λ_n^α will be similar to this. Note that Ω_n and Λ_n^α are closely related, in fact we have

$$\Lambda_D^\alpha = \frac{\Omega_D}{D} \tag{5-79}$$

Now we can define the spectral function

$$G_{\alpha\alpha}(\omega) = \int \frac{d^D \boldsymbol{k}}{(2\pi)^D} g_{\alpha\alpha}(\boldsymbol{k}) \delta(\omega - \epsilon_+ + \epsilon_-) [f(\epsilon_-) - f(\epsilon_+)] \tag{5-80}$$

$$= \frac{N\Omega_D}{8(2\pi)^d} \int_0^{\infty} k^{D-1} dk \frac{v^d}{v^2k^2 + M^2} \delta\left(\omega - \frac{2\sqrt{v^2k^2 + M^2}}{\hbar}\right) \tanh\frac{\sqrt{v^2k^2 + M^2}}{2k_BT} \tag{5-81}$$

$$- \frac{N\Lambda_D^\alpha}{8(2\pi)^d} \int_0^{\infty} k^{D+1} dk \frac{v^{D+2}}{\left(v^2k^2 + M^2\right)^2} \delta\left(\omega - \frac{2\sqrt{v^2k^2 + M^2}}{\hbar}\right) \tanh\frac{\sqrt{v^2k^2 + M^2}}{2k_BT}. \tag{5-82}$$

Making the change of variables

$$x = \sqrt{v^2k^2 + M^2} \to k = \sqrt{\frac{x^2 - M^2}{v^2}}, \tag{5-83}$$

$$xdx = v^2 k dk. \tag{5-84}$$

Then

$$G_{\alpha\alpha}(\omega) = \frac{N}{8}\frac{\Omega_D}{(2\pi)^D}\int_{|M|}^{\infty} dx \frac{(x^2-M^2)^{\frac{d-2}{2}}}{x}\delta\left(\omega-\frac{2x}{\hbar}\right)\tanh\frac{x}{2k_BT} \tag{5-85}$$

$$-\frac{N}{8}\frac{\Lambda_D^{\alpha}}{(2\pi)^D}\int_{|M|}^{\infty} dx \frac{(x^2-M^2)^{\frac{D}{2}}}{x^3}\delta\left(\omega-\frac{2x}{\hbar}\right)\tanh\frac{x}{2k_BT} \tag{5-86}$$

$$=\frac{N}{8}\left(\frac{\hbar^2\omega^2\Omega_D\left(\hbar^2\omega^2-4M^2\right)^{\frac{D}{2}-1}-\Lambda_d^{\alpha}\left(\hbar^2\omega^2-4M^2\right)^{\frac{D}{2}}}{4^{D-1}\pi^d\hbar^2\omega^3}\right)\tanh\frac{\hbar\omega}{4k_BT}\Theta\left(\omega>\frac{2M}{\hbar}\right) \tag{5-87}$$

Finally, using (5-79) we have

$$G_{\alpha\alpha}(\omega) = \frac{N}{8}\frac{\Omega_D\left(\hbar^2\omega^2-4M^2\right)^{\frac{d}{2}}}{4^{D-1}\pi^D\hbar^2\omega^3}\left(\frac{\hbar^2\omega^2}{\hbar^2\omega^2-4M^2}-\frac{1}{D}\right)\tanh\frac{\hbar\omega}{4k_BT}\Theta\left(\omega>\frac{2M}{\hbar}\right) \tag{5-88}$$

For example, compute $\alpha = x$ for different values of D

$$G_{xx}(\omega) = \begin{cases} \frac{N}{8}\left(\frac{4M^2}{\pi\hbar^2\omega^3\sqrt{\hbar^2\omega^2-4M^2}}\right)\tanh\frac{\hbar\omega}{4k_BT}\Theta\left(\omega>\frac{2M}{\hbar}\right), & \text{for } D=1 \\ \frac{N}{8}\left(\frac{\hbar^2\omega^2+4M^2}{4\pi\hbar^2\omega^3}\right)\tanh\frac{\hbar\omega}{4k_BT}\Theta\left(\omega>\frac{2M}{\hbar}\right), & \text{for } D=2 \\ \frac{N}{8}\left(\frac{\omega^2 4\pi\left(\hbar^2\omega^2-4M^2\right)^{\frac{1}{2}}-\left(\frac{4\pi}{3}\right)\left(\hbar^2\omega^2-4M^2\right)^{\frac{3}{2}}}{16\pi^3\hbar^2\omega^3}\right)\tanh\frac{\hbar\omega}{4k_BT}\Theta\left(\omega>\frac{2M}{\hbar}\right), & \text{for } D=3 \end{cases} \tag{5-89}$$

The integration of the quantum metric itself, i.e the fidelity number, is

$$G_{\alpha\alpha} = \int\frac{d^D\boldsymbol{k}}{(2\pi)^D}g_{\alpha\alpha}(\boldsymbol{k}) \tag{5-90}$$

$$=\frac{N\Omega_D}{8(2\pi)^D}\int_0^{\infty}dk\frac{k^{D-1}v^D}{v^2k^2+M^2}-\frac{1}{D}\frac{k^{D+1}v^{D+2}}{\left(v^2k^2+M^2\right)^2},$$

making the change of variables

$$x=\sqrt{v^2k^2+M^2}\rightarrow k=\sqrt{\frac{x^2-M^2}{v^2}}, \tag{5-91}$$

$$xdx = v^2kdk. \tag{5-92}$$

then

$$G_{\alpha\alpha} = \frac{N\Omega_D}{8(2\pi)^D}\int_{|M|}^{\infty}dx\frac{(x^2-M^2)^{\frac{D-2}{2}}}{x}-\frac{1}{d}\frac{(x^2-M^2)^{\frac{D}{2}}}{x^3} \tag{5-93}$$

We integrate up to a cutoff Λ and take the leading term in M [51]

$$G_{\alpha\alpha} = \frac{N\Omega_D}{8\left(2\pi\right)^D}\int_{|M|}^{\Lambda} dx \frac{\left(x^2-M^2\right)^{\frac{D-2}{2}}}{x} - \frac{1}{d}\frac{\left(x^2-M^2\right)^{\frac{D}{2}}}{x^3}, \tag{5-94}$$

$$= \frac{N}{8}\times\begin{cases}\frac{1}{8|M|} & \text{for } D=1,\\ \frac{1}{4\pi}\log\frac{\Lambda}{M} & \text{for } D=2,\\ -\frac{1}{8\pi}|M| & \text{for } D=3\end{cases} \tag{5-95}$$

We can also define the Fourier transform of the quantum metric

$$G_{\alpha\alpha} = \int \frac{d^D\boldsymbol{k}}{(2\pi)^D} g_{\alpha\alpha}\left(\boldsymbol{k}\right)e^{i\boldsymbol{k}\cdot\boldsymbol{r}} = \frac{N}{8}\int\frac{d^D\boldsymbol{k}}{(2\pi)^D}\frac{e^{i\boldsymbol{k}\cdot\boldsymbol{r}}}{v^2k^2+M^2} - \frac{v^2k_\alpha^2 e^{i\boldsymbol{k}\cdot\boldsymbol{r}}}{\left(v^2k^2+M^2\right)^2} \tag{5-96}$$

$$= \frac{N}{8\left(2\pi\right)^D}\int d\Omega_D\int_0^\infty dk k^{D-1}\frac{e^{ikr\cos\theta}}{v^2k^2+M^2} - \frac{v^2k_\alpha^2 e^{ikr\cos\theta}}{\left(v^2k^2+M^2\right)^2} \tag{5-97}$$

$$= \frac{N}{8\left(2\pi\right)^D}\int_0^\infty dk k^{D-1}\frac{\Xi_d\left(k,r\right)}{v^2k^2+M^2} - \frac{v^2k^2\Sigma_d^\alpha\left(k,r\right)}{\left(v^2k^2+M^2\right)^2} \tag{5-98}$$

where we have defined

$$\Xi_D\left(k,r\right) = \int d\Omega_D e^{ikr\cos\theta}, \tag{5-99}$$

$$\Sigma_D^\alpha\left(k,r\right) = \int d\Omega_D e^{ikr\cos\theta}\times\left(\alpha\text{-spherical component}\right). \tag{5-100}$$

We can compute the first values of Ξ_D

$$\Xi_1 = e^{ikr} \tag{5-101}$$

$$\Xi_2 = \int_0^{2\pi} e^{ikr\cos\theta}d\theta = 2\pi J_0\left(kr\right) \tag{5-102}$$

$$\Xi_3 = \int_0^{2\pi} d\phi\int_0^\pi \sin\theta d\theta e^{ikr\cos\theta} = 4\pi\frac{\sin kr}{kr} \tag{5-103}$$

It is straight forward to see that

$$\Xi_D\left(k,r\right) = \begin{cases} e^{ikr} & D=1,\\ 2\pi J_0\left(kr\right) & D=2,\\ 4\pi^2\frac{\sin kr}{kr} & D=3,\end{cases}$$

For $\Sigma_D^\alpha\left(k,r\right)$ we have

$$\Sigma_1^1 = e^{ikr} \tag{5-104}$$

$$\Sigma_2^1 = \int_0^{2\pi} e^{ikr\cos\phi}\cos^2\phi d\phi = 2\pi\left(\frac{J_1(kr) - krJ_2(kr)}{kr}\right) \tag{5-105}$$

$$\Sigma_3^1 = \int_0^{2\pi}\cos^2\phi d\phi\int_0^{\pi}\sin\theta d\theta\sin^2\theta e^{ikr\cos\theta} = 4\pi\left(\frac{\sin kr - kr\cos kr}{k^3r^3}\right) \tag{5-106}$$

And we see that

$$\Sigma_D^{\alpha}(k,r) = \begin{cases} e^{ikr} & D=1 \\ 2\pi\left(\frac{J_1(kr)}{kr} - J_2(kr)\right) & D=2 \\ 4\pi\left(\frac{\sin kr - kr\cos kr}{k^3r^3}\right) & D=3 \end{cases}$$

With these two factors worked out we have, for $D=1$

$$G_{\alpha\alpha} = \frac{N}{8(2\pi)}\int_{-\infty}^{\infty} dk\frac{\Xi_1(k,r)}{v^2k^2+M^2} - \frac{v^2k^2\Sigma_1^{\alpha}(k,r)}{(v^2k^2+M^2)^2} \tag{5-107}$$

$$= \frac{N}{8(2\pi)}\int_{-\infty}^{\infty} dk\frac{e^{ikr}}{v^2k^2+M^2} - \frac{v^2k^2e^{ikr}}{(v^2k^2+M^2)^2} \tag{5-108}$$

$$= \frac{N}{8}\frac{1}{4v^2}\frac{e^{-\frac{Mr}{v}}(|M|r+v)}{|M|} \tag{5-109}$$

For $D=2$

$$G_{\alpha\alpha} = \frac{N}{8(2\pi)^2}\int_0^{\infty} dkk\frac{\Xi_2(k,r)}{v^2k^2+M^2} - \frac{v^2k^2\Sigma_2^{\alpha}(k,r)}{(v^2k^2+M^2)^2} \tag{5-110}$$

$$= \frac{N}{8(2\pi)}\int_0^{\infty} dk\frac{kJ_0(kr)}{v^2k^2+M^2} - \frac{v^2k^2J_1(kr) - v^2k^3rJ_2(kr)}{r(v^2k^2+M^2)^2} \tag{5-111}$$

$$= \frac{N}{8}\frac{1}{4\pi v^2}\left[K_0\left(\frac{|M|r}{v}\right) + \frac{|M|r}{v}K_1\left(\frac{|M|r}{v}\right)\right] \tag{5-112}$$

For $D>3$

$$G_{\alpha\alpha} = \frac{N}{8(2\pi)^3}\int_0^{\infty} dkk^2\frac{\Xi_3(k,r)}{v^2k^2+M^2} - \frac{v^2k^2\Sigma_3^{\alpha}(k,r)}{(v^2k^2+M^2)^2} \tag{5-113}$$

$$= \frac{N}{8(2\pi)^3}\int_0^{\infty} dkk^2\frac{4\pi^2\frac{\sin kr}{kr}}{v^2k^2+M^2} - k^4\frac{4\pi\left(\frac{\sin kr - kr\cos kr}{k^3r^3}\right)}{(v^2k^2+M^2)^2} \tag{5-114}$$

$$= \frac{N}{8}\frac{e^{-\frac{|M|r}{v}}(2\pi-1)}{8\pi r} \tag{5-115}$$

For all dimensions we have that the correlation length diverges at the phase transition $M = 0$.

6
Opacity

In the chapter, we apply the quantum metric and fidelity number formalism in the previous chapter to a particularly important material, namely the single-layer graphene. We will elaborate that the well-known 2.3structure constant, actually carries the information of the quantum metric. In addition, because of the correspondence between the quantum metric and topological charge of the Dirac point, the opacity is also directly proportional to the topological charge. To be more precise, the fact that the experimentally observed polarization- and frequency-independence of the opacity is because the opacity is topologically protected. In other words, the fact that the opacity is always 2.3source of any frequency and polarization is actually attributed to the topological charge of the Dirac point. As a result, one can literally see the topological charge of graphene by naked eyes. In addition, the opacity as a function of frequency divided by frequency gives precisely the fidelity number spectral function introduced in the previous chapter.

6.1
Graphene

The tight-binding Hamiltonian for Graphene is

$$H = \sum_{\langle ij\rangle\sigma} t c_{i\sigma}^{\dagger} c_{j\sigma} \tag{6-1}$$

where $\langle ij\rangle$ means the summation over the next-nearest neighbors, $t = 2.8eV$ is the hopping energy, $c_{i\sigma}^{\dagger}$ is the creation operator at site i and spin polarization σ. We wish to investigate the behavior close to the so-called Dirac points, which are high-symmetry points on the Graphene Brillouin zone given by $\boldsymbol{K}^{\eta} = \left(\frac{2\pi}{3a}, \eta\frac{2\pi}{3\sqrt{3}a}\right)$, where $a = 1.42\text{Å}$ is the lattice spacing. We obtain the dispersion for Graphene by making the Fourier transform in to momentum space

$$\begin{aligned} c_{i\sigma}^{\dagger} &= \frac{1}{\sqrt{N}} \sum_{k} c_{k\sigma}^{\dagger} e^{-i\boldsymbol{k}\cdot\boldsymbol{r}_i}, \\ c_{j\sigma} &= \frac{1}{\sqrt{N}} \sum_{k} c_{k\sigma} e^{i\boldsymbol{k}\cdot\boldsymbol{r}_j}. \end{aligned} \tag{6-2}$$

Then we obtain

$$H = \sum_{\langle ij\rangle\sigma} \frac{1}{N} \sum_{kk'} t c^{\dagger}_{k\sigma} c_{k'\sigma} e^{-i(\boldsymbol{k}\cdot\boldsymbol{r}_i - \boldsymbol{k'}\cdot\boldsymbol{r}_j)},$$

where the sum $\sum_{\langle ij\rangle}$ constrains $\boldsymbol{r}_i - \boldsymbol{r}_j = \boldsymbol{\delta}_l$, where $\boldsymbol{\delta}$ are the nearest-neighbors hopping vectors given by

$$\boldsymbol{\delta}_1 = \frac{a}{2}\left(1, \sqrt{3}\right) \;\; \boldsymbol{\delta}_2 = \frac{a}{2}\left(1, -\sqrt{3}\right) \;\; \boldsymbol{\delta}_3 = a\left(-1, 0\right).$$

There we write

$$\begin{aligned} H &= \sum_{il\sigma} \frac{1}{N} \sum_{kk'} t c^{\dagger}_{k\sigma} c_{k'\sigma} e^{-i(\boldsymbol{k}-\boldsymbol{k'})\cdot\boldsymbol{r}_i} e^{-i\boldsymbol{k'}\cdot\boldsymbol{\delta}_l}, \\ &= \sum_{k\sigma} t c^{\dagger}_{k\sigma} c_{k\sigma} \left(\sum_l e^{-i\boldsymbol{k}\cdot\boldsymbol{\delta}_l} \right). \end{aligned}$$

To obtain the low-energy approximation we expand the expression in parenthesis close to the Dirac point, then

$$\begin{aligned} \sum_l e^{-i\boldsymbol{k}\cdot\boldsymbol{\delta}_l} &\approx \sum_l e^{-i\boldsymbol{K}^{\eta}\cdot\boldsymbol{\delta}_l} \left(1 - i\boldsymbol{k}\cdot\boldsymbol{\delta}_l\right), \\ &= -\frac{3}{4}\left(i + \sqrt{3}\right)\left(k_x - \eta i k_y\right). \end{aligned}$$

Noting that $i + \sqrt{3} = 2e^{i\pi/6}$,we can make the gauge transformation $k_x \to k_x$, $k_y \to e^{-i\pi/6} k_y$ to obtain

$$H = \hbar v_F \left(k_x \sigma_x + \eta k_y \sigma_y\right),$$

where we have defined the Fermi velocity $v_F = -\frac{3t}{2}$ and we recover the Planck constant for the sake of consistency. We note that we can highly simplify the eigenproblem by changing $\boldsymbol{k}$ to polar coordinates with $k_x = k\cos\varphi$, $k_y = k\sin\varphi$ and $k = \sqrt{k_x^2 + k_y^2}$. Then

$$\begin{aligned} H &= \hbar v_F k \left(\cos\varphi\sigma_x + \eta \sin\varphi \sigma_y\right), \\ &= \hbar v_F k \begin{pmatrix} 0 & e^{-\eta i\varphi} \\ e^{\eta i\varphi} & 0 \end{pmatrix} \end{aligned}$$

and we see that the eigenvalues are $\varepsilon_{\pm}\left(\boldsymbol{k}\right) = \pm\hbar v_F k$ and the eigenvectors are $|\pm\eta\rangle = \left(1/\sqrt{2}\right)\left(1, \mp e^{\eta i\varphi}\right)$.

6.2 Topological charge

As the eigenstates depend only one parameter φ, we can characterize the topology using the Berry phase or winding the number

$$\begin{aligned}\oint \frac{d\varphi}{2\pi} \langle -\eta | \, i\partial_\varphi \, | -\eta \rangle &= \oint \frac{d\varphi}{2\pi} \frac{1}{2} \left(1, e^{-\eta i\varphi}\right)^T \left(0, -\eta e^{\eta i\varphi}\right) \\ &= -\frac{1}{2}\eta = -\mathcal{C}\eta\end{aligned}$$

6.3 Quantum metric

As we are modelling graphene a Dirac Hamiltonina, We may use the formulation for of the quantum metric defined in the previous section. In the case of the $\varphi\varphi$-component

$$\begin{aligned}g_{\varphi\varphi}\left(\boldsymbol{k}\right) = &\frac{1}{2}\left(0, \mp\eta i e^{-\eta i\varphi}\right)^T \left(1, \pm\eta i e^{\eta i\varphi}\right) \\ &- \frac{1}{4}\left(0, \mp\eta i e^{-\eta i\varphi}\right)^T \left(1, \pm e^{\eta i\varphi}\right) \\ &\times \left(1, \mp e^{-\eta i\varphi}\right)^T \left(0, \pm\eta i e^{\eta i\varphi}\right) \\ &= \frac{1}{4}\eta^2 = \mathcal{C}^2\eta^2.\end{aligned}$$

To formulate the problem in terms of polar coordinates we define

$$\begin{aligned}\partial_x &= \cos\varphi\partial_k - \frac{1}{k}\sin\varphi\partial_\varphi, \\ \partial_y &= \sin\varphi\partial_k + \frac{1}{k}\cos\varphi\partial_\varphi.\end{aligned}$$

As states do not depend on k, we can drop the ∂_k terms: $\partial_x = -\frac{1}{k}\sin\varphi\partial_\varphi$, $\partial_y = \frac{1}{k}\cos\varphi\partial_\varphi$. Then the quantum metric in cartesian coordinates can be formulated as

$$g_{\mu\nu}\left(k\right) = \begin{pmatrix} \sin^2\varphi & -\sin\varphi\cos\varphi \\ -\sin\varphi\cos\varphi & \cos^2\varphi \end{pmatrix} \times \frac{g_{\varphi\varphi}}{k^2}$$

6.4 Opacity

Consider a polarized electromagnetic field interacting with an electron in Graphene. To calculate the opacity we need to calculate the incident flux W_i

and absorbed energy W_a, the absorption in then given as $P = W_a/W_i$. The incident flux W_i can be obtained from the Poynting vector

$$S = \frac{c}{4\pi}\boldsymbol{E} \times \boldsymbol{B}\,(\text{in Gaussian units})\,.$$

For a traveling wave in Gaussian units we have $E = B$, therefore

$$\boldsymbol{S} = \frac{c}{4\pi}E^2\hat{\boldsymbol{x}}.$$

The incident flux is then the magnitude of this quantity, $W_i = \frac{c}{4\pi}E^2$. The absorbed energy is given by $W_a = \eta\hbar\omega$, where η is the number of absorption events per unit of time and is calculated using Fermi's golden rule. We can treat this problem using minimal coupling, where the momenta is changed as $\boldsymbol{p}' = \boldsymbol{p} - q\boldsymbol{A}/c$, where $\boldsymbol{A} = ic\boldsymbol{E}/\omega$. Then, in terms of the reciprocal momentum

$$\hbar\boldsymbol{k}' = \hbar\boldsymbol{k} - \frac{iq\boldsymbol{E}}{\omega}.$$

Considering $\boldsymbol{E} = E_0\hat{\boldsymbol{x}}$, the components of the momentum are changed as $k_x' = k_x - iqE_0/\hbar\omega$, $k_y' = k_y$. Then the Graphene Hamiltonian is modified as

$$\begin{aligned} H' &= \hbar v_F\left[\left(k_x - \frac{iqE_0}{\hbar\omega}\right)\sigma_x + k_y\sigma_y\right] \\ &= \hbar v_F\left(k_x\sigma_x + k_y\sigma_y\right) - \frac{iv_FqE_0}{\omega}\sigma_x \\ &= H + \delta H \end{aligned}$$

The rate of particles excited from states $|n\rangle$ to state $|m\rangle$ is given by Fermi golden rule

$$\begin{aligned} \Gamma_{\boldsymbol{k}} &= \frac{2\pi}{\hbar}\left|\langle n|\,\delta H\,|m\rangle\right|^2\delta\left(\hbar\omega + \varepsilon_n - \varepsilon_m\right) \\ &= \frac{2\pi}{\hbar}\frac{v_F^2q^2E_0^2}{\omega^2}\frac{1}{4}\left|\left(1, e^{-\eta i\varphi}\right)^T\begin{pmatrix}0 & 1\\ 1 & 0\end{pmatrix}\left(1, -e^{\eta i\varphi}\right)\right|^2 \\ &\times\delta\left(\hbar\omega - 2\hbar v_Fk\right) \\ &= \frac{2\pi}{\hbar}\frac{v_F^2q^2E_0^2}{\omega^2}\sin^2\left(\eta\varphi\right)\delta\left(\hbar\omega - 2\hbar v_Fk\right) \end{aligned} \tag{6-3}$$

Another way to do the same calculation is see how the minimal coupling changes the energy of the system, consider the change of momenta on the

Hamiltonian $H = \frac{p^2}{2m}$

$$\begin{aligned} H' &= \frac{\left(\boldsymbol{p} - q\boldsymbol{A}/c\right)^2}{2m} \\ &= \frac{1}{2m}\left[\boldsymbol{p}\cdot\boldsymbol{p} - \frac{2q}{c}\left(\boldsymbol{p}\cdot\boldsymbol{A} + \boldsymbol{A}\cdot\boldsymbol{p}\right) + \frac{q^2}{c^2}\boldsymbol{A}\cdot\boldsymbol{A}\right] \end{aligned}$$

where the last term is the photon-photon term and is usually ignored at this level of calculation. In this case the minimal coupling enter the Hamiltonian as $\delta H = -\frac{q}{mc}\left(\boldsymbol{p}\cdot\boldsymbol{A} + \boldsymbol{A}\cdot\boldsymbol{p}\right)$, using $\boldsymbol{p} = \frac{\hbar}{i}\boldsymbol{\nabla}$ then we can write

$$\begin{aligned} \delta H &= -\frac{q}{mc}\frac{\hbar}{i}\left(\boldsymbol{\nabla}\cdot\boldsymbol{A} + \boldsymbol{A}\cdot\boldsymbol{\nabla}\right) \\ &= -\frac{q\hbar}{m\omega}\left(\boldsymbol{E}\cdot\boldsymbol{\nabla}\right) = -qE_0\frac{\hbar}{m\omega}\partial_x \end{aligned}$$

Defining $\hbar/m\omega$ as the natural length scale of the problem we find that the perturbation of the system due to the dipole is $\delta H = -qE_0\partial_x$. In this case the rate of particles excited is given by

$$\begin{aligned} \Gamma_{\boldsymbol{k}} &= \frac{2\pi}{\hbar}\left|\langle n|\, qE_0\partial_x\,|m\rangle\right|^2 \delta\left(\hbar\omega + \varepsilon_n - \varepsilon_m\right) \\ &= \frac{2\pi}{\hbar}q^2E_0^2\,\langle n|\,\partial_x\,|m\rangle\,\langle m|\,\partial_x\,|n\rangle\,\delta\left(\hbar\omega + \varepsilon_n - \varepsilon_m\right) \end{aligned}$$

Now, using the completeness relation $|n\rangle\langle n| + |m\rangle\langle m| = 1$

$$\begin{aligned} \Gamma_{\boldsymbol{k}} &= \frac{2\pi}{\hbar}q^2E_0^2\left[\langle\partial_x n|\partial_x n\rangle - \langle\partial_x n|n\rangle\langle n|\partial_x n\rangle\right] \\ &\quad\times\delta\left(\hbar\omega + \varepsilon_n - \varepsilon_m\right) \\ &= \frac{2\pi}{\hbar}q^2E_0^2 g_{xx}\delta\left(\hbar\omega + \varepsilon_n - \varepsilon_m\right). \end{aligned}$$

remember that $g_{xx} = \frac{\sin^2\varphi}{k^2}g_{\varphi\varphi}$, then

$$\Gamma_{\boldsymbol{k}} = \frac{2\pi}{\hbar}q^2E_0^2\frac{\sin^2\varphi}{k^2}g_{\varphi\varphi}\delta\left(\hbar\omega - 2\hbar v_F k\right). \tag{6-4}$$

Which provides the same answer as in 6-3 once we use the density of states relation of Graphene. The total number of absorption events per unit of time η is given by the integration of $\Gamma_{\boldsymbol{k}}$ over all the reciprocal space (recall that we

only need a $4\pi^2$ so that the calculation is correct)

$$\begin{aligned}\eta &= \int \frac{d^2\boldsymbol{k}}{(2\pi)^2}\Gamma_{\boldsymbol{k}} \\ &= \frac{1}{2\pi\hbar}q^2E_0^2 g_{\varphi\varphi}\int kdkd\varphi\frac{\sin^2\varphi}{k^2}\delta\left(\hbar\omega - 2\hbar v_F k\right) \\ &= \frac{1}{2\hbar}q^2E_0^2 g_{\varphi\varphi}\int \frac{dk}{k}\delta\left(\hbar\omega - 2\hbar v_F k\right) \\ &= \frac{1}{2\hbar}q^2E_0^2 g_{\varphi\varphi}\int \frac{d\varepsilon}{\varepsilon}\delta\left(\hbar\omega - 2\varepsilon\right) \\ &= \frac{q^2E_0^2 g_{\varphi\varphi}}{\hbar^2\omega}\end{aligned} \tag{6-5}$$

Then the absorbed flux is given by $W_a = q^2E_0^2 g_{\varphi\varphi}/\hbar$ and the absorption then is

$$\begin{aligned}P = \frac{W_a}{W_i} &= \frac{4\pi q^2E_0^2 g_{\varphi\varphi}}{\hbar c E_0^2} = \pi\alpha \times 4g_{\varphi\varphi} \\ &= 2.3\% \times 4g_{\varphi\varphi}\end{aligned}$$

where $\alpha = q^2/\hbar c$ is the fine structure constant [52, 53, 54, 55, 56]. We notice that the opacity in independent of momentum or, in other words, the frequency of the incident light and it is proportional to the topological charge. In principle, this allow us to measure topological charge by measuring the opacity of the material by shining a light onto it and seeing how much light is absorbed. Graphene has lattice vectors $a_1 = \frac{a}{2}\left(3, \sqrt{3}\right)$ and $a_2 = \frac{a}{2}\left(3, -\sqrt{3}\right)$, where a is the lattice spacing. The area of the unit-cell is given by the area of the parallelogram enclosed by a_1 and a_2, which is given by the determinant expression

$$A_{\text{cell}} = \frac{a^2}{4}\begin{vmatrix}3 & \sqrt{3} \\ 3 & -\sqrt{3}\end{vmatrix} = \frac{3\sqrt{3}}{2}a^2.$$

Similarly, for the reciprocal vectors defined as

$$a_i \cdot b_j = 2\pi\delta_{ij}$$

we have $b_1 = \frac{2\pi}{3a}\left(1, \sqrt{3}\right)$ and $b_2 = \frac{2\pi}{3a}\left(1, -\sqrt{3}\right)$. The area enclosed by these two vectors in momentum space is given by the determinant expression

$$A_{\text{BZ}} = \frac{4\pi^2}{9a^2}\begin{vmatrix}1 & \sqrt{3} \\ 1 & -\sqrt{3}\end{vmatrix} = \frac{8\pi^2}{3\sqrt{3}a^2}.$$

Notice that in 6-5 we averaged out the states by dividing over by $(2\pi)^2$, instead we can consider that only states inside the area of the Brillouin zone

are considered and average out

$$\begin{aligned}
\eta &= \int \frac{d^2\boldsymbol{k}}{A_{\mathrm{BZ}}}\Gamma_{\boldsymbol{k}} \\
&= \frac{1}{A_{\mathrm{BZ}}}\frac{2\pi}{\hbar}q^2E_0^2g_{\varphi\varphi}\int kdkd\varphi\frac{\sin^2\varphi}{k^2}\delta\left(\hbar\omega-2\hbar v_Fk\right) \\
&= \frac{1}{A_{\mathrm{BZ}}}\frac{2\pi^2}{\hbar}q^2E_0^2g_{\varphi\varphi}\int \frac{dk}{k}\delta\left(\hbar\omega-2\hbar v_Fk\right) \\
&= \frac{1}{A_{\mathrm{BZ}}}\frac{2\pi^2}{\hbar}q^2E_0^2g_{\varphi\varphi}\int \frac{d\varepsilon}{\varepsilon}\delta\left(\hbar\omega-2\varepsilon\right) \\
&= \frac{1}{A_{\mathrm{BZ}}}\frac{4\pi^2q^2E_0^2g_{\varphi\varphi}}{\hbar^2\omega}
\end{aligned}$$

Then the absorbed flux is $W_a = A_{\mathrm{BZ}}^{-1}4\pi^2q^2E_0^2g_{\varphi\varphi}/\hbar$. Similarly, we can consider that the area of incidence is only the unit-cell area, therefore the incident flux $W_i = A_{\mathrm{cell}}\frac{c}{4\pi}E_0^2$. Then

$$\begin{aligned}
P = \frac{W_a}{W_i} &= \frac{4\pi^2}{A_{\mathrm{BZ}}A_{\mathrm{cell}}}\frac{4\pi q^2E_0^2g_{\varphi\varphi}}{\hbar cE_0^2} \\
&= \pi\alpha\times 4g_{\varphi\varphi}
\end{aligned}$$

because $A_{\mathrm{BZ}}A_{\mathrm{cell}} = 4\pi^2$.

7
Conclusions

This work has provided an exploration of graphene properties and its potential applications, particularly in the field of spintronics. Since its experimental discovery in 2004, graphene has been the subject of extensive research due to its remarkable properties, including its extraordinary strength, thinness, and electrical properties.

The present work builds upon previous studies on Rashba spin-orbit coupling in graphene by proposing an extended tight-binding model for the material that incorporates both Rashba spin-orbit coupling and an external magnetic field. This model has been used to demonstrate that equilibrium current can be developed in graphene and that the currents properties can be controlled by the direction of the applied magnetic field.

Furthermore, this thesis has explored the properties of graphene nanoflakes, where only partial spin polarization can occur, leading to the development of a non-zero spin-torque. A device has been proposed that utilizes graphene atop a substrate, inducing Rashba spin-orbit coupling in the graphene through various proximity effects. This type of device holds promising applications in spintronics, particularly in spin-transfer-torque devices.

Additionally, we investigated the symmetry properties of two-dimensional materials like graphene, including non-symmorphic symmetries and their implications on the system's eigenvalues. The existence of symmetry-protected nodal lines has been demonstrated as a result of these restrictions. A method called "vacancy engineering" has been introduced, which allows for the creation of materials with desired symmetries by removing atoms from the lattice. This method has been shown to be effective in predicting the appearance of nodal lines in the band structure, as well as being robust to perturbations.

By employing vacancy engineering, we also proposed a procedure for the creation of flat-bands in bipartite lattices through the removal of atoms. It has been demonstrated that arbitrary flat-bands can be created, and the number of flat-bands is related to the unbalance of atoms in the lattice partitions. While flat-bands in twisted bilayer graphene are associated with various physical effects, it has been investigated whether the flat-bands in our model can host similar effects, particularly superconductivity.

Bibliography

[1] NOVOSELOV, K. S.; GEIM, A. K.; MOROZOV, S. V.; JIANG, D.; ZHANG, Y.; DUBONOS, S. V.; GRIGORIEVA, I. V. ; FIRSOV, A. A.. **Electric field effect in atomically thin carbon films**. Science, 306(5696):666–669, oct 2004.

[2] MARCHENKO, D.; VARYKHALOV, A.; SCHOLZ, M.; BIHLMAYER, G.; RASHBA, E.; RYBKIN, A.; SHIKIN, A. ; RADER, O.. **Giant rashba splitting in graphene due to hybridization with gold**. 2012.

[3] KOCHAN, D.; IRMER, S. ; FABIAN, J.. **Model spin-orbit coupling hamiltonians for graphene systems**. Physical Review B, 95(16):165415, apr 2017.

[4] MIN, H.; HILL, J. E.; SINITSYN, N. A.; SAHU, B. R.; KLEINMAN, L. ; MACDONALD, A. H.. **Intrinsic and rashba spin-orbit interactions in graphene sheets**. Physical Review B, 74(16):165310, oct 2006.

[5] DE SOUSA, M. S. M.; SIGRIST, M. ; CHEN, W.. **Magnetoelectric torque and edge currents in spin-orbit coupled graphene nanoribbons**. Physical Review Research, 3(3):033021, jul 2021.

[6] RYBKIN, A. G.; RYBKINA, A. A.; OTROKOV, M. M.; VILKOV, O. Y.; KLIMOVSKIKH, I. I.; PETUKHOV, A. E.; FILIANINA, M. V.; VOROSHNIN, V. Y.; RUSINOV, I. P.; ERNST, A.; ARNAU, A.; CHULKOV, E. V. ; SHIKIN, A. M.. **Magneto-spin–orbit graphene: Interplay between exchange and spin–orbit couplings**. Nano Letters, 18(3):1564–1574, jan 2018.

[7] DYRDAŁ, A.; BARNAŚ, J.. **Current-induced spin polarization and spin-orbit torque in graphene**. Physical Review B, 92(16):165404, oct 2015.

[8] LI, H.; MANCHON, A.. **Tunable spin-charge conversion through topological phase transitions in zigzag nanoribbons**. Physical Review B, 93(23):235317, jun 2016.

[9] RODRIGUEZ-VEGA, M.; SCHWIETE, G.; SINOVA, J. ; ROSSI, E.. **Giant edelstein effect in topological-insulator–graphene heterostructures**. Physical Review B, 96(23):235419, dec 2017.

[10] ZOLLNER, K.; PETROVIĆ, M. D.; DOLUI, K.; PLECHÁČ, P.; NIKOLIĆ, B. K. ; FABIAN, J.. **Scattering-induced and highly tunable by gate damping-like spin-orbit torque in graphene doubly proximitized by two-dimensional magnet**. Physical Review Research, 2(4):043057, oct 2020.

[11] RYBKINA, A. A.; RYBKIN, A. G.; KLIMOVSKIKH, I. I.; SKIRDKOV, P. N.; ZVEZDIN, K. A.; ZVEZDIN, A. K. ; SHIKIN, A. M.. **Advanced graphene recording device for spin–orbit torque magnetoresistive random access memory**. Nanotechnology, 31(16):165201, jan 2020.

[12] DE SOUSA, M. S. M.; LIU, F.; MALARD, M.; QU, F. ; CHEN, W.. **Symmetry-enforced nodal lines in the band structures of vacancy-engineered graphene**. Physical Review B, 105(15):155414, apr 2022.

[13] SUTHERLAND, B.. **Localization of electronic wave functions due to local topology**. Physical Review B, 34(8):5208–5211, oct 1986.

[14] LIEB, E. H.. **Two theorems on the hubbard model**. Physical Review Letters, 62(10):1201–1204, mar 1989.

[15] DE SOUSA, M. S. M.; LIU, F.; QU, F. ; CHEN, W.. **Vacancy-engineered flat-band superconductivity in holey graphene**. Physical Review B, 105(1):014511, jan 2022.

[16] CAO, Y.; FATEMI, V.; FANG, S.; WATANABE, K.; TANIGUCHI, T.; KAXIRAS, E. ; JARILLO-HERRERO, P.. **Unconventional superconductivity in magic-angle graphene superlattices**. Nature, 556(7699):43–50, mar 2018.

[17] WALLACE, P. R.. **The band theory of graphite**. Physical Review, 71(9):622–634, may 1947.

[18] NETO, A. H. C.; GUINEA, F.; PERES, N. M. R.; NOVOSELOV, K. S. ; GEIM, A. K.. **The electronic properties of graphene**. Rev. Mod. Phys. 81, 109 (2009), 81(1):109–162, jan 2007.

[19] RASHBA, E. I.. **Spin currents in thermodynamic equilibrium: The challenge of discerning transport currents**. Physical Review B, 68(24):241315, dec 2003.

[20] REYNOSO, A.; USAJ, G.; SÁNCHEZ, M. J. ; BALSEIRO, C. A.. **Theory of edge states in systems with rashba spin-orbit coupling**. Physical Review B, 70(23):235344, dec 2004.

[21] GRIGORYAN, V. L.; ABIAGUE, A. M. ; BADALYAN, S. M.. **Spin edge states: An exact solution and oscillations of the spin current**. Physical Review B, 80(16):165320, oct 2009.

[22] NAKHMEDOV, E.; ALEKPEROV, O.. **Out-of-plane equilibrium spin current in a quasi-two-dimensional electron gas under in-plane magnetic field**. Physical Review B, 85(15):153302, apr 2012.

[23] USAJ, G.; BALSEIRO, C. A.. **Spin accumulation and equilibrium currents at the edge of 2degs with spin-orbit coupling**. Europhysics Letters (EPL), 72(4):631–637, nov 2005.

[24] KLINOVAJA, J.; STANO, P.; YAZDANI, A. ; LOSS, D.. **Topological superconductivity and majorana fermions in RKKY systems**. Physical Review Letters, 111(18):186805, nov 2013.

[25] CHEN, W.. **Absence of equilibrium edge currents in theoretical models of topological insulators**. Physical Review B, 101(19):195120, may 2020.

[26] MA, Z.; SHENG, W.. **A spin-valve device based on dumbbell-shaped graphene nanoislands**. Applied Physics Letters, 99(8):083101, aug 2011.

[27] WEYMANN, I.; BARNAŚ, J. ; KROMPIEWSKI, S.. **Manifestation of the shape and edge effects in spin-resolved transport through graphene quantum dots**. Physical Review B, 85(20):205306, may 2012.

[28] LUO, K.; SHENG, W.. **Many-body effects in the spin-polarized electron transport through graphene nanoislands**. Journal of Applied Physics, 115(5):053705, feb 2014.

[29] SZAŁOWSKI, K.. **Graphene nanoflakes in external electric and magnetic in-plane fields**. Journal of Magnetism and Magnetic Materials, 382:318–327, may 2015.

[30] YOUNG, S. M.; KANE, C. L.. **Dirac semimetals in two dimensions**. Physical Review Letters, 115(12):126803, sep 2015.

[31] WIEDER, B. J.; BRADLYN, B.; WANG, Z.; CANO, J.; KIM, Y.; KIM, H.-S. D.; RAPPE, A. M.; KANE, C. L. ; BERNEVIG, B. A.. **Wallpaper fermions and the nonsymmorphic dirac insulator**. Science, 361(6399):246–251, jul 2018.

[32] ZHANG, J.; CHAN, Y.-H.; CHIU, C.-K.; VERGNIORY, M. G.; SCHOOP, L. M. ; SCHNYDER, A. P.. **Topological band crossings in hexagonal materials**. Physical Review Materials, 2(7):074201, jul 2018.

[33] LIU, F.; QU, F.; ŽUTIĆ, I.; XIE, S.; LIU, D.; FONSECA, A. L. A. ; MALARD, M.. **Robust topological nodal-line semimetals from periodic vacancies in two-dimensional materials**. The Journal of Physical Chemistry Letters, 12(24):5710–5715, jun 2021.

[34] LIU, F.; QU, F.; ŽUTIĆ, I. ; MALARD, M.. **Vacancy-engineered nodal-line semimetals**. Scientific Reports, 12(1), sep 2022.

[35] JACOBSE, P. H.; MCCURDY, R. D.; JIANG, J.; RIZZO, D. J.; VEBER, G.; BUTLER, P.; ZUZAK, R.; LOUIE, S. G.; FISCHER, F. R. ; CROMMIE, M. F.. **Bottom-up assembly of nanoporous graphene with emergent electronic states**. Journal of the American Chemical Society, 142(31):13507–13514, jul 2020.

[36] SCHNYDER, A. P.; RYU, S.; FURUSAKI, A. ; LUDWIG, A. W. W.. **Classification of topological insulators and superconductors in three spatial dimensions**. Physical Review B, 78(19):195125, nov 2008.

[37] RYU, S.; SCHNYDER, A. P.; FURUSAKI, A. ; LUDWIG, A. W. W.. **Topological insulators and superconductors: tenfold way and dimensional hierarchy**. New Journal of Physics, 12(6):065010, jun 2010.

[38] KITAEV, A.; LEBEDEV, V. ; FEIGEL'MAN, M.. **Periodic table for topological insulators and superconductors**. In: AIP CONFERENCE PROCEEDINGS. AIP, 2009.

[39] CHIU, C.-K.; TEO, J. C.; SCHNYDER, A. P. ; RYU, S.. **Classification of topological quantum matter with symmetries**. Reviews of Modern Physics, 88(3):035005, aug 2016.

[40] SAITO, R.; JORIO, A.; FILHO, A. G. S.; DRESSELHAUS, G.; DRESSELHAUS, M. S. ; PIMENTA, M. A.. **Probing phonon dispersion relations of graphite by double resonance raman scattering**. Physical Review Letters, 88(2):027401, dec 2001.

[41] MAULTZSCH, J.; REICH, S.; THOMSEN, C.; REQUARDT, H. ; ORDEJÓN, P.. **Phonon dispersion in graphite**. Physical Review Letters, 92(7):075501, feb 2004.

[42] MOHR, M.; MAULTZSCH, J.; DOBARDŽIĆ, E.; REICH, S.; MILOŠEVIĆ, I.; DAMNJANOVIĆ, M.; BOSAK, A.; KRISCH, M. ; THOMSEN, C.. **Phonon dispersion of graphite by inelastic x-ray scattering**. Physical Review B, 76(3):035439, jul 2007.

[43] KOPNIN, N. B.; HEIKKILÄ, T. T. ; VOLOVIK, G. E.. **High-temperature surface superconductivity in topological flat-band systems**. Physical Review B, 83(22):220503, jun 2011.

[44] PROVOST, J. P.; VALLEE, G.. **Riemannian structure on manifolds of quantum states**. Communications in Mathematical Physics, 76(3):289–301, sep 1980.

[45] GIERZ, I.; PETERSEN, J. C.; MITRANO, M.; CACHO, C.; TURCU, I. C. E.; SPRINGATE, E.; STÖHR, A.; KÖHLER, A.; STARKE, U. ; CAVALLERI, A.. **Snapshots of non-equilibrium dirac carrier distributions in graphene**. Nature Materials, 12(12):1119–1124, oct 2013.

[46] DE SOUSA, M. S. M.; CRUZ, A. L. ; CHEN, W.. **Mapping quantum geometry and quantum phase transitions to real space by a fidelity marker**. Physical Review B, 107(20):205133, may 2023.

[47] STILLMAN, G.; ROBBINS, V. ; TABATABAIE, N.. **III-v compound semiconductor devices: Optical detectors**. IEEE Transactions on Electron Devices, 31(11):1643–1655, nov 1984.

[48] VON GERSDORFF, G.; CHEN, W.. **Measurement of topological order based on metric-curvature correspondence**. Physical Review B, 104(19):195133, nov 2021.

[49] SU, W. P.; SCHRIEFFER, J. R. ; HEEGER, A. J.. **Solitons in polyacetylene**. Physical Review Letters, 42(25):1698–1701, jun 1979.

[50] CHIU, C.-K.; SCHNYDER, A. P.. **Classification of reflection-symmetry-protected topological semimetals and nodal superconductors**. Physical Review B, 90(20):205136, nov 2014.

[51] MATSUURA, S.; RYU, S.. **Momentum space metric, nonlocal operator, and topological insulators**. Physical Review B, 82(24):245113, dec 2010.

[52] NAIR, R. R.; BLAKE, P.; GRIGORENKO, A. N.; NOVOSELOV, K. S.; BOOTH, T. J.; STAUBER, T.; PERES, N. M. R. ; GEIM, A. K.. **Fine**

structure constant defines visual transparency of graphene. Science, 320(5881):1308–1308, jun 2008.

[53] STAUBER, T.; PERES, N. M. R. ; GEIM, A. K.. **Optical conductivity of graphene in the visible region of the spectrum**. Physical Review B, 78(8):085432, aug 2008.

[54] BRUNA, M.; BORINI, S.. **Optical constants of graphene layers in the visible range**. Applied Physics Letters, 94(3):031901, jan 2009.

[55] WEBER, J. W.; CALADO, V. E. ; VAN DE SANDEN, M. C. M.. **Optical constants of graphene measured by spectroscopic ellipsometry**. Applied Physics Letters, 97(9):091904, aug 2010.

[56] NAIR, R. R.; REN, W.; JALIL, R.; RIAZ, I.; KRAVETS, V. G.; BRITNELL, L.; BLAKE, P.; SCHEDIN, F.; MAYOROV, A. S.; YUAN, S.; KATSNELSON, M. I.; CHENG, H.-M.; STRUPINSKI, W.; BULUSHEVA, L. G.; OKOTRUB, A. V.; GRIGORIEVA, I. V.; GRIGORENKO, A. N.; NOVOSELOV, K. S. ; GEIM, A. K.. **Fluorographene: A two-dimensional counterpart of teflon**. Small, 6(24):2877–2884, nov 2010.

A
Graph Theory Approach to Tight-binding models

A.1
Introduction

The idea of this report is to give a translation between spectral properties of graphs from Graph Theory and the theory of tight-binding models. The tight-binding model describes systems where the electrons are localized on atomic sites and may hop to its neighboring sites. The amplitude associated which such hop is usually denoted as t. The Hamiltonian is

$$H = \sum_{i\sigma} t c^{\dagger}_{\sigma,i} c_{\sigma,i}. \tag{A-1}$$

One such approximation is where the electrons may only hop to their first neighboring sites, in this case the subscript i of the summation above is replaced by $\langle i, j\rangle$, meaning the summation only occur for the first neighbors. This approximation is related to a problem of graph theory where each site is connected only to its neighboring sites.

Ignoring spin, we may interpret the matrix element $\langle i| H |j\rangle$ as an edge going from vertex i to j in a undirected graph. In real space, the correspondence is evident. If we normalize the hopping parameter $t = 1$, then $\langle i| H |j\rangle$ corresponds to a element of the adjacency matrix.

A.2
Preliminaries

Let G be a graph representing the physical connections between sites. The adjacency matrix $A(G)$ of a graph G with n vertices is an $n \times n$ symmetric matrix with elements a_{ij} such that

$$a_{ij} = \begin{cases} 1, & \text{if vertices } i \text{ and } j \text{ are adjacent} \\ 0, & \text{otherwise} \end{cases} . \tag{A-2}$$

Definição A.1 *A graph is said simple if all vertices are distict and labelled and if there are no loops.*

Definição A.2 *A graph is said singular is its adjacency matrix $A(G)$ is singular, i.e at least one of its eigenvalues is zero.*

Definição A.3 *The multiplicity of the zero eigenvalue of A is called nullity and denoted $\eta(G)$, it is also the dimension of the nullspace of A.*

The rank of a graph is defined as $rank(G) = n(G) - \eta(G)$, where $n(G)$ is the order of G. The zero eigenvalue also defines a non-trivial eigenvector called kernel from which entries induce two sub-graphs of G called core and periphery.

Definição A.4 *The kernel eigenvector v_0 is an eigenvector in the nullspace of A.*

Definição A.5 *The non-zero components of the kernel eigenvector v_0 induces a subgraph of vertices in G called core χ. Another subgraph is induced from the complement $\mathcal{V}(G) - \mathcal{V}(\chi)$, this is called periphery $\mathcal{P}$.*

The eigenvalues correspond to a tight-binding Hamiltonian with zero energy at the Γ-point. The core corresponds to where wave-function is localized at this energy and the periphery is where the wave-function vanishes. This interpretation is aligned with another method relating spectral properties of graphs and properties of chemical systems called Hückel Theory.

The nullity of a graph may change its nullity when adding or removing vertices from it. In particular the nullity increase by one if we remove one vertex from the periphery as a consequence of the Interlacing Theorem.

Graphs come in different shapes and forms depending on application. In our case we are interested in bipartite graphs which are realized in square lattices, honeycomb lattices and much others. These have special importance due to its relation to so-called particle-hole symmetry. For bipartite graphs the rank is bounded by the matching number $\mu(G)$, the length of maximum independent edge set, i.e the set of edges such that they share no vertices. For the bipartite graph the the bound is $rank(G) \leq 2\mu(G)$, where for trees the equality holds.

A.3
Bipartite graphs

A graph G is said bipartite if the vertex set $\mathcal{V}(G)$ can partitioned into two sets U and V such that no two vertices from the same set are adjacent. Each bipartite graph has an unique bipartition. Let $u \in U$ be a element in U and $v \in V$ a element in V, then it follows from the definition of G that in the basis $\{u^1 \dots u^p v^i \dots v^q\}$ the adjacency matrix $A(G)$ has the form

$$A = \begin{pmatrix} 0 & B \\ B^\dagger & 0 \end{pmatrix}, \tag{A-3}$$

where B is a p times q matrix. The bipartition of a graph may be found from inspection but a more systematic way is to find the co-cliques of the graph. The co-clique is a property of a graph similar to the matching number mentioned above.

Definição A.6 *Co-clique is a subset of the vertices of a graph such that no two vertices are adjacent.*

In particular for bipartite graph, where the bipartition is unique, the biggest co-clique corresponds to biggest partition of G. The other partition may be derived from the complement $\mathcal{V}(V) = \mathcal{V}(G) - \mathcal{V}(U)$.

For practical purposes, we would like to start with a balanced bipartite graph where $|U| = |V|$. Upon vacancy engineering this graph will become unbalanced.

Throughout this work it is assumed that the dimension of the domain is the same as the number of columns of the matrix such that Rank-nullity theorem holds in the following form

Teorema A.7 *Let M be a matrix with m rows and n columns then*

$$rank(M) + \eta(M) = n. \tag{A-4}$$

Proposição A.8 *Let B be a matrix, then $rank(B) = rank(B^\dagger) = rank(BB^\dagger) = rank(B^\dagger B)$.*

Prova. Let $B_{p\times q}$ have nullity $\eta(B) = k$ and let ψ_k its correspondent eigenvectors. Then

$$\psi_k^* B^\dagger B \psi_k = 0. \tag{A-5}$$

Let $C = B^\dagger B$, then C has the same nullity as B. The rank-nullity theorem states that

$$rank(C) = q - k = rank(B). \tag{A-6}$$

It follows from the definition of C that $rank(C) \leq rank(B^\dagger)$. The same argument follows conversely, $C^\dagger = BB^\dagger$ has the same nullity as $B^\dagger$ and rank-nullity states that

$$rank(C^\dagger) = p - k = rank(B^\dagger), \tag{A-7}$$

and $rank(C^\dagger) \leq rank(B)$. Using Eq. A-6 and Eq. A-7 together with the two inequalities we conclude $rank(B) = rank(B^\dagger)$ and $rank(C) = rank(C^\dagger)$. ■

Proposição A.9 *Let A a matrix of the form A-3, it follows that $rank(A) = 2\,rank(B)$.*

Prova. Let $C_1 = \begin{pmatrix} 0 & B \end{pmatrix}$ and $C_2 = \begin{pmatrix} B^\dagger & 0 \end{pmatrix}$ such that A has the form

$$A = \begin{pmatrix} C_1 \\ C_2 \end{pmatrix}. \tag{A-8}$$

Then $rank(A) = rank(C_1) + rank(C_2) = rank(B) + rank(B^\dagger)$. The proof is complete because $rank(B) = rank(B^\dagger)$. ■

Proposição A.10 *Let A a matrix of the form A-3, if B is not square then A is singular.*

Prova. Let $A_{n\times n}$ and $B_{p\times q}$ matrices such that $p + q = n$. The rank-nullity theorem states that $rank(B) + \eta(B) = q$. Let B have nullity $\eta(B) = k$ and $rank(B) = q - k$. From the property that G is bipartite in A.9 $rank(A) = 2(q-k)$. Rank-nullity theorem for A states that $\eta(A) = p-q+2k$. If $p-q > 0$ then $\eta(A) > 0$ and A is singular in general. ■

Corolário A.11 *When B is square we have the identity $\eta(A) = 2k$. Then A will be singular only if B is also singular.*

Remark 1 *If A of the form A-3 is singular and if B is not singular then either $BB^\dagger$ or $B^\dagger B$ is singular. Which one is singular depends on the ordering of the partitions.*

Prova. From Proposition A.8 we have $rank(BB^\dagger) = rank(B^\dagger B)$. Moreover, let $B_{p\times q}$ and take the rank-nullity theorem

$$rank(BB^\dagger) + \eta(BB^\dagger) = p, \tag{A-9}$$

$$rank(B^\dagger B) + \eta(B^\dagger B) = q, \tag{A-10}$$

then

$$\eta(BB^\dagger) - \eta(B^\dagger B) = p - q. \tag{A-11}$$

Take $\eta(B^\dagger B) = 0$, then we need $\eta(BB^\dagger) = p - q$ and from Proposition A.8 $\eta(B^\dagger) = p - q$ and $rank(B) = q$. This is done by ordering the partitions such that $|U| > |V|$. If we take $\eta(B^\dagger B) = 0$, then we need $\eta(B^\dagger B) = q - p = \eta(B)$ and $rank(B) = p$. This is done by ordering the partitions such that $|V| > |U|$. ■

Remark 2 *From Remark A.3 and Proposition A.8 we conclude that the zero eigenvalue is localized at the biggest partition.*

Take the square of A

$$A^2 = \begin{pmatrix} BB^\dagger & 0 \\ 0 & B^\dagger B \end{pmatrix} \tag{A-12}$$

which is now positive definite.

Remark 3 *A and A^2 share the zero eigenvalue and its correspondent eigenvector. From the block-diagonal form of matrix A-12 we conclude that this eigenvector is orthogonal across partitions.*

B
Projecting states in the Eigenproblem

We start the argument by setting up the eigenproblem that we want to investigate. As motivating example of what we want to prove we consider a generic 3×3 matrix

$$A = \begin{pmatrix} a & b & c \\ d & e & f \\ g & h & i \end{pmatrix}. \tag{B-1}$$

We want to show that the characteristic polynomial

$$\det\left(A - \mathbb{I}\lambda\right) = \begin{vmatrix} a-\lambda & b & c \\ d & e-\lambda & f \\ g & h & i-\lambda \end{vmatrix} = 0 \tag{B-2}$$

of this matrix reduces to

$$(a-\lambda) \times \begin{vmatrix} e-\lambda & f \\ h & i-\lambda \end{vmatrix} = 0, \tag{B-3}$$

as $a \to \infty$. To prove this we need to rely on the three properties of the determinants:

1. Adding a linear combination of rows to another row leave the determinant invariant.

2. Swapping two rows contributes to a minus sign on the original determinant.

3. Multiplying a row by a scalar k contributes to a factor of k to the original determinant.

With properties we can perform the row reduction of the characteristic polynomial equation

$$\begin{vmatrix} a-\lambda & b & c \\ 0 & (e-\lambda)-\frac{bd}{(a-\lambda)} & f-\frac{cd}{(a-\lambda)} \\ 0 & h-\frac{bh}{(a-\lambda)} & (i-\lambda)-\frac{cg}{(a-\lambda)} \end{vmatrix} = 0. \tag{B-4}$$

It's clear that the determinant is given by

$$(a-\lambda)\times\begin{vmatrix} (e-\lambda)-\frac{bd}{(a-\lambda)} & f-\frac{cd}{(a-\lambda)} \\ h-\frac{bh}{(a-\lambda)} & (i-\lambda)-\frac{cg}{(a-\lambda)}, \end{vmatrix} \tag{B-5}$$

and in the limit $a \to \infty$ we recover the desired result (B-3). Simple inspection and we see that we will have "spurious" eigenvalues at $\lambda = a$ and the remaning eigenvalues are given by $\lambda = \frac{1}{2} \pm \left(\sqrt{e^2 - 2ei + 4fh + i^2} + e + i\right)$, i.e. the eigenvalues corresponding matrix after removing the row and column of the matrix element a. A similar analysis can be carried out for the eigenvectors. As an example consider a 3×3 symmetric matrix

$$A = \begin{pmatrix} U & b & c \\ b & 0 & d \\ c & d & 0 \end{pmatrix}. \tag{B-6}$$

As $U \to \infty$ the eigenvalues would be $\lambda \in \{-d, d, U\}$. For the λ_i eigenvalue the $|\xi_i\rangle$ eigenvector is obtained by solving the system of linear equations

$$\begin{pmatrix} U-\lambda_i & b & c \\ b & -\lambda_i & d \\ c & d & -\lambda_i \end{pmatrix}\begin{pmatrix} \xi_i^1 \\ \xi_i^2 \\ \xi_i^3 \end{pmatrix} = \begin{pmatrix} 0 \\ 0 \\ 0 \end{pmatrix}, \tag{B-7}$$

which can be written in the augmented matrix form

$$\left[\begin{array}{ccc|c} U-\lambda_i & b & c & 0 \\ b & -\lambda_i & d & 0 \\ c & d & -\lambda_i & 0 \end{array}\right] \tag{B-8}$$

After performing the row reduction as in the previous section we get

$$\left[\begin{array}{ccc|c} U-\lambda_i & b & c & 0 \\ 0 & -\lambda_i-\frac{b^2}{(a-\lambda)} & d-\frac{bd}{(a-\lambda)} & 0 \\ 0 & d-\frac{bc}{(a-\lambda)} & -\lambda_i-\frac{c^2}{(a-\lambda)} & 0 \end{array}\right]. \tag{B-9}$$

Taking the limit $U \to \infty$ and without loss of generality we can set $\xi_i^3 = 1$ and it will follow that $\xi_i^2 = \frac{\lambda_i}{d}$ and $\xi_i^3 = \frac{cd-b}{d(U-\lambda_i)}$. Thus we can write the eigenvectors as

$$|\xi_i\rangle = \frac{1}{\mathcal{N}_i}\left(1, \frac{\lambda}{d}, \frac{cd-b}{d(U-\lambda_i)}\right)^T, \tag{B-10}$$

where $\mathcal{N}_i$ is the normalization of the eigenvector. We note that the effect of U is to decouple the the eigenspace in two subspaces, one containing the set of "usable" eigenvectors and another which will contain a set of "disposable" eigenvectors that are projected onto to the space vector containing only the zero vector. To notice the occurence of this projection on the eigenvectors we see that as $U \to \infty$ all the vectors in the "disposable" eigenspace are projected onto the zero vector. The normalization factor is given by

$$\mathcal{N}_i = \sqrt{1 + \left|\frac{\lambda_i}{d}\right|^2 + \left|\frac{b-cd}{d(U-\lambda_i)}\right|^2}. \tag{B-11}$$

If $\lambda \neq U$, in the limit $U \to \infty$ it reduces to the usual value

$$\mathcal{N}_i = \sqrt{1 + \left|\frac{\lambda_i}{d}\right|^2}. \tag{B-12}$$

Care must be taken in the case $\lambda_3 = U$. The first two components of the eigenvector go to zero in the limit, the only non-trivial term is

$$\frac{\frac{cd-b}{d(U-\lambda_3)}}{\mathcal{N}_3} = \frac{cd-b}{d}\frac{1}{\sqrt{1 + \left|\frac{\lambda_3}{d}\right|^2 + \left|\frac{b-cd}{d(U-\lambda_3)}\right|^2}(U-\lambda_3)}. \tag{B-13}$$

In the limit $U \to \infty$ the third term dominates the square root and the terms just cancel out to give the answer

$$|\xi_3\rangle = (0,0,1)^T. \tag{B-14}$$

Therefore we have the realization that this second eigenspace consist of only two vectors: $|0\rangle_Q$ and $|1\rangle_Q$, where Q signals that these states live in the second eigenspace. We explicitly separate the eigenvector in two eigenspaces

$$|\xi_i\rangle = |\xi_i\rangle_P \otimes |\xi_i\rangle_Q, \tag{B-15}$$

where $|\xi_i\rangle_P$ are the eigenvectors after removing the row and column of the matrix A and $|\xi_i\rangle_Q = \left\{|0\rangle_Q, |1\rangle_Q\right\}$. Denoting $|p\rangle$ an element of the P-subspace and $|q\rangle$ an element of the Q-subspace. A vector spanned by the set of eigenvectors would have the form

$$|\varphi\rangle = \sum_{i=1}^{|P|} p_i |p_i\rangle + \sum_{j=1}^{|Q|} q_j |q_j\rangle \tag{B-16}$$

where $p_i = \langle p_i|\varphi\rangle$ and $q_j = \langle q_j|\varphi\rangle$, $|P|$ is the number of elements in the P-subspace and $|Q| = 2$ from the argument of the previous discusssion. The identity of this eigenspace can be written as

$$\sum_{i=1}^{|P|} |p_i\rangle \langle p_i| + \sum_{j=1}^{|Q|} |q_j\rangle \langle q_j| = \mathbb{I}. \tag{B-17}$$

As discussed before, the elements of Q consist of "spurious" eigenvectors that we want to discard at some point. To this end, we can define projection onto the P and Q subspaces.

$$\mathcal{P}_P = \sum_{i=1}^{|P|} |p_i\rangle \langle p_i| \tag{B-18}$$

$$\mathcal{P}_Q = \sum_{j=1}^{|Q|} |q_j\rangle \langle q_j| \tag{B-19}$$

Using (B-18) we can write the "clean" inner product between two vectors as

$$\langle\psi|\varphi\rangle = \langle\psi| \mathcal{P}_P |\varphi\rangle = \sum_{i=1}^{|P|} \langle\psi|p_i\rangle \langle p_i|\varphi\rangle . \tag{B-20}$$

Similarly, "expectation values" of an operator $\mathcal{O}$ can be taken as

$$\langle\psi| \mathcal{O} |\varphi\rangle = \langle\psi| \mathcal{P}_P \mathcal{O} \mathcal{P}_P |\varphi\rangle = \sum_{i=1}^{|P|} \sum_{j=1}^{|P|} \langle\psi|p_i\rangle \langle p_i| \mathcal{O} |p_j\rangle \langle p_j|\varphi\rangle . \tag{B-21}$$

In light of (B-15), we can simplify the notation by arranging the elements of the eigenvectors in such way that the p-elements comes first and q-elements comes after. This way, the projector onto the P-subspace would be

$$\sum_{i=1}^{|P|} |\xi_i\rangle \langle \xi_i| \tag{B-22}$$

where ξ is an element of the whole eigenspace. If we do this we can avoid the $|1\rangle_Q$ element completely and it will not interfere in the calculations. This observation is rather obvious as we already stated that the structure obtained in (B-15) was an effect of taking the limit. Then

$$\langle\psi|\varphi\rangle = \sum_{i=1}^{|P|} \langle\psi|\xi_i\rangle \langle\xi_i|\varphi\rangle \,, \tag{B-23}$$

and

$$\langle\psi| \mathcal{O} |\varphi\rangle = \sum_{i=1}^{|P|} \sum_{j=1}^{|P|} \langle\psi|\xi_i\rangle \langle\xi_i| \mathcal{O} |\xi_j\rangle \langle\xi_j|\varphi\rangle \,. \tag{B-24}$$

If U is big but not necessarily infinite, the separation between P and Q-subspaces is not very sharp and we would have elements mixing these two subspaces. To investigate this we consider the projection onto this mixing elements

$$\mathcal{P}_{\text{mix}} = \sum_{i=1}^{|P|} \sum_{j=1}^{|Q|} |p_i\rangle \langle q_j| + |q_j\rangle \langle p_i| \,. \tag{B-25}$$

In some sense, we can relate this projection as a measure of the error in taking the limit. For instance, the measure of error of the inner product is

$$|\langle\psi|\varphi\rangle_{\text{Error}}|^2 = \langle\psi| \mathcal{P}_{\text{mix}} |\varphi\rangle \langle\varphi| \mathcal{P}_{\text{mix}} |\psi\rangle = \tag{B-26}$$

$$= \sum_{i}^{|P|} \sum_{j}^{|Q|} \langle\psi|p_i\rangle \langle q_j|\varphi\rangle \langle\varphi|p_i\rangle \langle q_j|\psi\rangle + \langle\psi|p_i\rangle \langle q_j|\varphi\rangle \langle\varphi|q_j\rangle \langle p_i|\psi\rangle \tag{B-27}$$

$$+ \langle\psi|q_j\rangle \langle p_i|\varphi\rangle \langle\varphi|p_i\rangle \langle q_j|\psi\rangle + \langle\psi|q_j\rangle \langle p_i|\varphi\rangle \langle\varphi|q_j\rangle \langle p_i|\psi\rangle \tag{B-28}$$

$$= \langle\psi| \mathcal{P}_P |\psi\rangle \langle\varphi| \mathcal{P}_Q |\varphi\rangle + \langle\psi| \mathcal{P}_Q |\psi\rangle \langle\varphi| \mathcal{P}_P |\varphi\rangle \tag{B-29}$$

$$+ \sum_{i}^{|P|} \sum_{j}^{|Q|} \langle\psi|p_i\rangle \langle q_j|\varphi\rangle \langle\varphi|p_i\rangle \langle q_j|\psi\rangle + \langle\psi|q_j\rangle \langle p_i|\varphi\rangle \langle\varphi|q_j\rangle \langle p_i|\psi\rangle \tag{B-30}$$

If we ignore the crossing terms for now and focus on the first two terms, we see that the error in the inner product is given by the product of projections

$$|\langle\psi|\varphi\rangle_{\text{Error}}|^2 = \langle\psi| \mathcal{P}_P |\psi\rangle \langle\varphi| \mathcal{P}_Q |\varphi\rangle + \langle\psi| \mathcal{P}_Q |\psi\rangle \langle\varphi| \mathcal{P}_P |\varphi\rangle + (\text{crossing terms}). \tag{B-31}$$

We can write this expression in a slightly different way

$$|\langle\psi|\varphi\rangle_{\text{Error}}|^2 = \langle\psi|\,\mathcal{P}_P + \mathcal{P}_Q\,|\psi\rangle\,\langle\varphi|\,\mathcal{P}_P + \mathcal{P}_Q\,|\varphi\rangle \tag{B-32}$$

$$- \langle\psi|\,\mathcal{P}_P\,|\psi\rangle\,\langle\varphi|\,\mathcal{P}_P\,|\varphi\rangle - \langle\psi|\,\mathcal{P}_Q\,|\psi\rangle\,\langle\varphi|\,\mathcal{P}_Q\,|\varphi\rangle \tag{B-33}$$

From the definition (B-17) $\mathcal{P}_P + \mathcal{P}_Q = \mathbb{I}$ and from the normalization condition $\langle\psi|\psi\rangle = \langle\varphi|\varphi\rangle = 1$, therefore

$$|\langle\psi|\varphi\rangle_{\text{Error}}|^2 = 1 - \langle\psi|\,\mathcal{P}_P\,|\psi\rangle\,\langle\varphi|\,\mathcal{P}_P\,|\varphi\rangle - \langle\psi|\,\mathcal{P}_Q\,|\psi\rangle\,\langle\varphi|\,\mathcal{P}_Q\,|\varphi\rangle\,, \tag{B-34}$$

and if they are the same state $\psi = \varphi$, then

$$|\langle\psi|\psi\rangle_{\text{Error}}|^2 = 1 - |\langle\psi|\,\mathcal{P}_P\,|\psi\rangle|^2 - |\langle\psi|\,\mathcal{P}_Q\,|\psi\rangle|^2\,. \tag{B-35}$$

To check this result we can consider the two extreme cases. If $|\psi\rangle \in P$ then $|\langle\psi|\,\mathcal{P}_P\,|\psi\rangle|^2 = 1$ and $|\langle\psi|\,\mathcal{P}_Q\,|\psi\rangle|^2 = 0$, therefore the error is zero $|\langle\psi|\psi\rangle_{\text{Error}}|^2 = 0$. If $|\psi\rangle \in Q$ then $|\langle\psi|\,\mathcal{P}_P\,|\psi\rangle|^2 = 0$ and $|\langle\psi|\,\mathcal{P}_Q\,|\psi\rangle|^2 = 1$ and again $|\langle\psi|\psi\rangle_{\text{Error}}|^2 = 0$. These results suggest that the terms that were ignored in (B-31) are at least an order of magnitude smaller and can be neglected for this analysis. In the case where U is large but not infinite we would have $|\langle\psi|\,\mathcal{P}_P\,|\psi\rangle|^2 \approx 1 - \frac{A}{U^2}$ and $|\langle\psi|\,\mathcal{P}_Q\,|\psi\rangle|^2 \approx \frac{B}{U^2}$, where A and B are constants. Therefore

$$|\langle\psi|\psi\rangle_{\text{Error}}|^2 \approx \frac{A-B}{U^2}. \tag{B-36}$$

Assuming $A - B = k$ then the choice of $U = 25k$ would make the error in the inner product of about 0.16%. We can estimate the value of k from the norm of the matrix after removing the row and column, i.e. $||\mathcal{P}_P A \mathcal{P}_P||$, the norm itself can be estimated for example by calculating the maximum of the absolute value of the sum of rows or columns. A similar argument can be made to show that $|\langle\psi|\,\mathcal{O}\,|\varphi\rangle_{\text{Error}}|^2 \propto \frac{1}{U^2}$.

We can generalize this result by taking the limit of more elements in the diagonal going to infinity, say $U_1 \to \infty, U_2 \to \infty \ldots U_N \to \infty$. In this case we would have $N + 1$ eigenspaces where N is the number of elements in the diagonal going to infinity that contains only two elements. Of course $N + 1 \leq n$ where n is the dimension of the matrix considered. We would

explicitly separate the eigenstates as such

$$|\xi_i\rangle = |\xi_i\rangle_P \otimes |\xi_i\rangle_{Q_1} \otimes |\xi_i\rangle_{Q_2} \ldots \otimes |\xi_i\rangle_{Q_N} , \tag{B-37}$$

and $|\xi_i\rangle_{Q_j} = \left\{ |0\rangle_{Q_j} , |1\rangle_{Q_j} \right\}$. Consider a vector spanned by the eigenvectors would have the form

$$|\varphi\rangle = \sum_{i=1}^{|P|} p_i |p_i\rangle + \sum_{j=1}^{|Q_1|} q_j^{(1)} \left|q_j^{(1)}\right\rangle + \sum_{j=1}^{|Q_2|} q_j^{(2)} \left|q_j^{(2)}\right\rangle + \ldots + \sum_{j=1}^{|Q_N|} q_j^{(N)} \left|q_j^{(N)}\right\rangle . \tag{B-38}$$

All the previous discussion apply to each subspace separately. But if we take the limit for all U's simultanously we can colapse these vector spaces into a single vector space of dimension N and with only two states, $|0, 0, \ldots, 0\rangle_Q$ and $|1, 1, \ldots, 1\rangle_Q$. Therefore the argument is identical to the previous section. In this case a vector would be spanned again as

$$|\varphi\rangle = \sum_{i=1}^{|P|} p_i |p_i\rangle + \sum_{j=1}^{|Q|} q_j |q_j\rangle . \tag{B-39}$$

We can summarize the result in the following. For the practical purpose of calculating the eigenvalues and eigenvectors of the matrix A then the limit $U \to \infty$ is equivalent to removing the row and column of the matrix.

$$\begin{pmatrix} U & a_{12} & a_{13} & a_{14} \\ a_{21} & a_{22} & a_{23} & a_{24} \\ a_{31} & a_{32} & U & a_{34} \\ a_{41} & a_{42} & a_{43} & a_{44} \end{pmatrix} \to \begin{pmatrix} a_{22} & a_{24} \\ a_{42} & a_{44} \end{pmatrix} \tag{B-40}$$

The price paid to is to have an additional eigenvalue at $\lambda = \infty$ and its corresponding eigenvector $|1\rangle_Q$. For practical calculations, avoiding this $|1\rangle_Q$ eigenvector, we can sort the eigenvalues in increasing order is such way that this eigenvector is the very last ones and we need to use only the $|P|$ first elements. In the case where U is not infinite but big, we can assert that at least that the reduced matrix will converge to the desired one with $\frac{1}{U}$ and the result of inner products and taking expectation values will converge to the answer with $\frac{1}{U^2}$.